



**HEAD TRACKING FOR 3D AUDIO
USING A GPS-AIDED MEMS IMU**

THESIS

Jacque M. Joffrion, Captain, USAF

AFIT/GE/ENG/05-09

**DEPARTMENT OF THE AIR FORCE
AIR UNIVERSITY**

AIR FORCE INSTITUTE OF TECHNOLOGY

Wright-Patterson Air Force Base, Ohio

APPROVED FOR PUBLIC RELEASE; DISTRIBUTION UNLIMITED

The views expressed in this thesis are those of the author and do not reflect the official policy or position of the United States Air Force, Department of Defense, or the United States Government.

AFIT/GE/ENG/05-09

HEAD TRACKING FOR 3D AUDIO USING A GPS-AIDED
MEMS IMU

THESIS

Presented to the Faculty of the
Department of Electrical and Computer Engineering
Graduate School of Engineering and Management
of the Air Force Institute of Technology
Air University
In Partial Fulfillment of the
Requirements for the Degree of
Master of Science

Jacque M. Joffrion, BSEE
Captain, USAF

March 2005

Approved for public release; distribution unlimited.

HEAD TRACKING FOR 3D AUDIO USING A GPS-AIDED MEMS IMU

Jacque M. Joffrion, BSEE
Captain, USAF

Approved:

/signed/

Dr John F. Raquet (Chairman)

date

/signed/

Dr Peter S. Maybeck (Member)

date

/signed/

Dr Meir Pachter (Member)

date

/signed/

Dr Mikel M. Miller (Member)

date

/signed/

Major Russell G. Adelgren (Member)

date

Acknowledgements

I would like to thank my committee for their excellent instruction on the fundamentals of inertial navigation, Kalman filtering, and INS/GPS integration required to conduct this research. I would especially like to thank my advisor, Dr. Raquet, for his encouragement and guidance during this research. Even across three time zones, Dr. Raquet was readily available to answer questions and provide expert advice.

A special thanks goes to my wife and daughter for their sacrifices during my time at AFIT and TPS. Without their love, support, and understanding, this thesis would not have been possible. Finally, I would like to express my gratitude to God for blessing me with this tremendous opportunity.

Jacque M. Joffrion

Table of Contents

	Page
Acknowledgements	iii
List of Figures	viii
List of Tables	xii
Abstract	xv
I. Introduction	1-1
1.1 Background	1-1
1.2 Problem Definition	1-3
1.3 Related Research	1-4
1.3.1 Head Trackers	1-4
1.3.2 Low Cost IMU/GPS Integration	1-6
1.4 Assumptions	1-7
1.5 Methodology	1-8
1.6 Thesis Overview	1-8
II. Background	2-1
2.1 Overview	2-1
2.2 Inertial Navigation	2-1
2.2.1 Basic Principles	2-1
2.2.2 Attitude Representation	2-2
2.3 Global Positioning System	2-4
2.4 Kalman Filters	2-6
2.4.1 Stochastic Difference Equation	2-6

	Page
2.4.2 State Transition Matrix	2-7
2.4.3 Measurement Model	2-8
2.4.4 Incorporating Measurements into the Estimates	2-8
2.4.5 Propagating State Estimates and Error Covari- ance	2-9
2.4.6 Covariance Analysis	2-9
2.5 INS/GPS Integration	2-10
2.5.1 State Space Formulation	2-10
2.5.2 Feedforward and Feedback Implementations .	2-11
2.5.3 INS/GPS Integration Levels	2-12
2.6 Hardware/Test Equipment	2-14
2.6.1 Inertial Measurement Unit	2-14
2.6.2 GPS Receiver	2-14
2.6.3 Pentium 4 Laptop	2-15
2.6.4 Truth Data	2-15
2.6.5 Test Aircraft	2-16
2.7 Summary	2-17
III. Methodology and Algorithm Development	3-1
3.1 Overview	3-1
3.2 Inertial Navigation System	3-2
3.2.1 INS Alignment	3-2
3.2.2 Modeling the Earth	3-4
3.2.3 Propagation of the Direction Cosine Matrix .	3-6
3.2.4 DCM Orthogonalization	3-7
3.2.5 Determining Position and Velocity in the Navi- gation Frame	3-8
3.3 Kalman Filter	3-10

	Page
3.3.1 Dynamics Model.	3-11
3.3.2 Process Noise	3-14
3.3.3 Measurement Model	3-16
3.3.4 Measurement Noise	3-19
3.3.5 Initial Conditions	3-21
3.3.6 Kalman Filter Cycle.	3-21
3.3.7 Feedback Corrections	3-22
3.4 Real-Time Software	3-23
3.5 Chapter Summary	3-24
IV. Test Results and Analysis	4-1
4.1 Overview	4-1
4.2 Flight Test Background Information	4-1
4.2.1 System Configuration	4-1
4.2.2 Data Collection	4-2
4.2.3 Overall Test Methodology	4-4
4.2.4 Data Sets	4-5
4.3 Flight Test Results	4-5
4.3.1 Straight-and-Level Unaccelerated Flight	4-15
4.3.2 Steady Heading Side Slip	4-18
4.3.3 Ground Alignment Through Climbout	4-19
4.3.4 Deficiencies in Real-Time Data Capture of Sensor Outputs	4-23
4.4 Benefits of Head Tracker Seen in 3D Audio Analysis	4-25
4.5 Further Analyses	4-30
4.5.1 GPS Outage	4-30
4.5.2 GPS Course Measurement	4-39
4.5.3 Simplified Dynamics Model	4-43
4.6 Chapter Summary	4-46

	Page
V. Conclusions and Recommendations	5-1
5.1 Overview	5-1
5.2 Conclusions	5-1
5.3 Recommendations	5-4
Appendix A. C-12C Tail Number 73-1215 Equipment Coordinates .	A-1
Bibliography	BIB-1
Vita	VITA-1

List of Figures

Figure		Page
2.1.	Error State Feedforward Implementation	2-11
2.2.	Error State Feedback Implementation	2-12
2.3.	Tightly-Coupled INS/GPS Integration [18]	2-13
2.4.	Loosely-Coupled INS/GPS Integration [18]	2-13
2.5.	XSens MT9 Inertial Measurement Unit	2-14
2.6.	Garmin GPS 35 Receiver	2-15
2.7.	GPS Aided Inertial Navigation Reference (GAINR) Equipment	2-16
2.8.	C-12C Huron	2-17
3.1.	INS/GPS Integration Flowchart	3-1
3.2.	Local-Level INS Mechanization Scheme [34]	3-9
3.3.	Raw Stationary Data from Y Accelerometer	3-15
3.4.	Raw Stationary Data from X Gyro	3-15
3.5.	Position Error and filter-predicted $\pm 1 \sigma$	3-17
3.6.	Velocity Error and filter-predicted $\pm 1 \sigma$	3-18
3.7.	Attitude Error and filter-predicted $\pm 1 \sigma$	3-18
3.8.	Down Velocity Measurement Error and $\pm 1 \sigma$	3-20
4.1.	System Diagram	4-2
4.2.	Hardware Mounted in C-12C	4-3
4.3.	Top of Data Acquisition System Rack	4-3
4.4.	Data Set 2 Ground Track	4-7
4.5.	Data Set 2 Horizontal TSPI Position Trajectory	4-8
4.6.	Data Set 2 TSPI Position	4-8
4.7.	Data Set 2 TSPI Velocity	4-9

Figure		Page
4.8.	Data Set 2 TSPI Attitude	4-9
4.9.	Data Set 2 Filter Estimated Accelerometer Bias	4-10
4.10.	Data Set 2 Filter Estimated Gyro Drift	4-11
4.11.	Data Set 2 Position Residuals	4-12
4.12.	Data Set 2 Velocity Residuals	4-12
4.13.	Data Set 2 Position Error and Filter Predicted $\pm 1 \sigma$	4-13
4.14.	Data Set 2 Velocity Error and Filter Predicted $\pm 1 \sigma$	4-13
4.15.	Data Set 2 Tilt Error and Filter Predicted $\pm 1 \sigma$	4-14
4.16.	Data Set 2 TSPI and Filter Estimated Attitude	4-15
4.17.	TSPI and Filter Estimated Attitude during SLUF - Data Set 2	4-16
4.18.	Filter Angular Accuracy in Straight-and-Level Unaccelerated Flight - Data Set 2	4-16
4.19.	TSPI and Filter Estimated Heading - Data Set 5 (Straight-and- Level Unaccelerated Flight Occurred Between 1 and 5 Minutes and Between 9 and 13 Minutes)	4-18
4.20.	TSPI and Filter Estimated Attitude - Steady Heading Side Slip (From 78 Seconds to 88 Seconds)	4-19
4.21.	Ground Ops through Takeoff Ground Track - Data Set 1	4-20
4.22.	TSPI Heading and Filter Estimated Heading During Takeoff Roll - Data set 1	4-20
4.23.	Attitude Error - Comparison Between Magnetometer-Based and GAINR-Based Alignments - Data Set 1	4-22
4.24.	Accelerometer Bias States - Comparison Between Magnetometer- Based and GAINR-Based Alignments - Data Set 1	4-22
4.25.	Gyro Drift States - Comparison Between Magnetometer-Based and GAINR-Based Alignments - Data Set 1	4-23
4.26.	Effect of Data Gap on Attitude Error - Data Set 5 (2.2 Second Data Gap Shown By Vertical Lines)	4-24
4.27.	MT9 IMU Mounted on Headset	4-26

Figure		Page
4.28.	GAINR-Coupled Localization Elevation Response Performance	4-27
4.29.	Head Tracker-Coupled Localization Elevation Response Performance	4-27
4.30.	GAINR-Coupled Localization Azimuth Response Performance	4-29
4.31.	Head Tracker-Coupled Localization Azimuth Response Performance	4-29
4.32.	Real-Time Processing and Post-Processing - Position Error .	4-31
4.33.	Difference Between Real-Time Processing and Post-Processing - Position Error	4-31
4.34.	Real-Time Processing and Post-Processing - Velocity Error .	4-32
4.35.	Difference Between Real-Time Processing and Post-Processing - Velocity Error	4-32
4.36.	Real-Time Processing and Post-Processing - Attitude Error .	4-33
4.37.	Difference Between Real-Time Processing and Post-Processing - Attitude Error	4-33
4.38.	Attitude Error with 60 Second GPS Outage During SLUF . .	4-35
4.39.	Tilt Error and Filter Predicted $\pm 1 \sigma$ with 60 Second GPS Outage During SLUF	4-35
4.40.	Attitude Error with 60 Second GPS Outage During 2G Turn	4-36
4.41.	Tilt Error and Filter Predicted $\pm 1 \sigma$ with 60 Second GPS Outage During 2G Turn	4-36
4.42.	Position Error and Filter Predicted $\pm 1 \sigma$ with 60 Second GPS Outage During SLUF	4-37
4.43.	Velocity Error and Filter Predicted $\pm 1 \sigma$ with 60 Second GPS Outage During SLUF	4-37
4.44.	Position Error and Filter Predicted $\pm 1 \sigma$ with 60 Second GPS Outage During 2G Turn	4-38
4.45.	Velocity Error and Filter Predicted $\pm 1 \sigma$ with 60 Second GPS Outage During 2G Turn	4-38
4.46.	TSPI Course and TSPI Heading	4-39

Figure		Page
4.47.	Difference between TSPI Heading and TSPI Course	4-41
4.48.	Difference between TSPI Course and GPS Course	4-42
4.49.	Attitude Error with and without GPS Heading Measurement	4-42
4.50.	Tilt Error and Filter Predicted $\pm 1 \sigma$ with and without GPS Heading Measurement	4-43
4.51.	Difference Between Full and Simplified Dynamics Model - Po- sition Error	4-47
4.52.	Difference Between Full and Simplified Dynamics Model - Ve- locity Error	4-47
4.53.	Difference Between Full and Simplified Dynamics Model - Atti- tude Error	4-48

List of Tables

Table		Page
2.1.	Estimated TSPI Accuracy (1σ)	2-16
3.1.	WGS 84 Fundamental Parameters [31]	3-4
3.2.	Kalman Filter State Definitions	3-10
3.3.	Dynamics Noise Standard Deviations	3-17
3.4.	Measurement Noise Standard Deviations	3-20
3.5.	Filter Initial Standard Deviations	3-21
4.1.	C-12C Aircraft Maneuver Set for Inertial Head Tracker Evaluation	4-5
4.2.	Data Set Summary	4-6
4.3.	Alignment Comparison Attitude Results	4-21

List of Acronyms and Abbreviations

1PPS	One-Pulse-Per-Second
3D	Three-Dimensional
AFB	Air Force Base
AFFTC	Air Force Flight Test Center
AFRL/HE	Air Force Research Laboratory Human Effectiveness Directorate
AHRS	Attitude and Heading Reference System
AOB	Angle of Bank
C/A	Coarse Acquisition
DAS	Data Acquisition System
DCM	Direction Cosine Matrix
EGI	Embedded GPS/INS
GAINR	GPS Aided Inertial Reference
GPS	Global Positioning System
HUD	Heads Up Display
IMC	Instrument Meteorological Conditions
IMU	Inertial Measurement Unit
INS	Inertial Navigation System
KIAS	Knots Indicated Airspeed
kts	knots
Level Accel	Level acceleration
Level Decel	Level deceleration
MEMS	Microelectromechanical System
MSL	Mean Sea Level
NMEA	National Marine Electronics Association
Ops	Operations
P(Y)	Precise (Encrypted)
PA	Pressure Altitude
PCMCIA	Personal Computer Memory Card International Association
RS-232	Recommended Standard-232

RWR	Radar Warning Receiver
SHSS	Steady Heading Side Slip
SLUF	Straight-and-Level Unaccelerated Flight
TCAS	Traffic alert and Collision Avoidance System
TOL	Tolerance
TSPI	Time, Space, Position Information
VMC	Visual Meteorological Conditions
WGS 84	World Geodetic System 1984

Abstract

Audio systems have been developed which use stereo headphones to project sound in three dimensions. When using these 3D audio systems, audio cues sound like they are originating from a particular direction. There is a desire to apply 3D audio to general aviation applications, such as projecting control tower transmissions in the direction of the tower or providing an audio orientation cue for VFR pilots who find themselves in emergency zero-visibility conditions. 3D audio systems, however, require real-time knowledge of the pilot's head orientation in order to be effective. This research describes the development and testing of a low-cost head tracking system for 3D audio rendering applied in general aviation. The system uses a low-cost MEMS IMU combined with a low-cost, single frequency GPS receiver. Real-time data from both of these systems was sent to a laptop computer where a real-time Kalman filter was implemented in MATLAB to solve for position velocity, and attitude. The attitude information was then sent to a 3D audio system for sound direction rendering. The system was flight tested on board a Raytheon C-12C aircraft. The accuracy of the system was measured by comparing its output to truth data from a high-accuracy post-processed navigation-grade INS/DGPS solution. Results showed that roll and pitch error were accurate to within 1-2 degrees, but that heading error was dependent upon the flight trajectory. During straight-and-level flight, the heading error would drift up to 10-15 degrees because of heading unobservability. However, even with heading error, the ability of a pilot to determine the correct direction of a 3D audio cue was significantly improved when using the developed head tracking system over using the navigation-grade INS/GPS system fixed to the aircraft.

HEAD TRACKING FOR 3D AUDIO USING A GPS-AIDED MEMS IMU

I. Introduction

1.1 Background

The benefits of integrating an Inertial Navigation System (INS) and the Global Positioning System (GPS) are well known in the area of navigation. Typically, an INS can maintain accurate estimates of position, velocity, and attitude over the short term while GPS provides accurate position and velocity information over the long term. Navigation is not the only area that has reaped the benefits of this powerful synergy. Head tracking is yet another application of INS/GPS integration and is the focus of this thesis research. Many applications require precise orientation information of a person's head. Virtual reality simulators, helmet-mounted displays, and three-dimensional (3D) audio generators are just a few systems that require head orientation information.

The head tracker developed in this research was designed to be implemented with a 3D audio system. 3D audio uses various techniques based on an understanding of how humans recognize the directionality of sound to reproduce these effects using headphones [7]. Potential applications for this technology exist in both military and general aviation.

In the world of high performance military aviation, task management is critical. For example, in a low altitude environment, a pilot continually has to divide his or her resources among terrain clearance tasks (i.e., avoiding the ground), mission critical tasks (e.g., placing bombs on target), and non-critical tasks (i.e., items that

can be accomplished in a flexible window) [1]. Displaying sensor information to the operator in the most efficient manner can reduce task saturation and increase mission effectiveness. This is why the Heads Up Display (HUD) was developed. A HUD allows pilots to cross check information like aircraft altitude and airspeed without “burying” their eyes inside the cockpit during critical tasks such as air intercepts, weapons employment, or landing. 3D audio can be used in much the same way. If an aircraft is being tracked by a surface-to-air missile battery, the pilot will be alerted by an auditory cue from the Radar Warning Receiver (RWR). He will then have to look inside the cockpit at the RWR display to determine azimuth information of the threat. If the auditory cue were directional, the pilot could perform the appropriate threat reaction in less time and therefore increase survivability [33].

3D audio can be a great asset in general aviation as well. Two situations that commonly lead to fatal accidents in general aviation are spatial disorientation and midair collisions. The use of 3D audio may be able to lower the number of fatalities in both of these areas. Spatial disorientation is usually not a problem under day visual meteorological conditions (VMC); however, a pilot can easily become disoriented when flying in instrument meteorological conditions (IMC) or at night. This is especially true if a pilot without instrument training inadvertently flies into weather. Spatial disorientation could possibly be prevented by providing spatial auditory cues to the pilot when the aircraft has been flown into an unusual attitude. If 3D audio is combined with information provided by a Traffic alert and Collision Avoidance System (TCAS), auditory spatial cues can be generated to alert pilots of approaching aircraft and provide a reference for evasive action. This has promise of reducing the number of fatalities due to midair collisions.

The potential for 3D audio to improve safety in general aviation has been recognized by Congress. The FY2003 Appropriation Conference directed funding for research in 3D audio display technology for general aviation [4], and the research is being managed by the Air Force Research Laboratory Human Effectiveness Di-

rectorate (AFRL/HE). In turn, AFRL/HE is the primary sponsor for this thesis research on INS-based head tracking technology.

In order for 3D audio to provide useful relative information, the orientation of the user's head with respect to a common reference frame must be available. This can be accomplished by mounting an Inertial Measurement Unit (IMU) to a headset. Using a low cost Micro-Electro-Mechanical System (MEMS) IMU for this application, as opposed to other types of IMUs, makes sense for a couple of reasons. First of all, the IMU must be lightweight or it would be uncomfortable to wear and could potentially cause neck injury. Secondly, the developed system should be affordable to the general aviator. Currently, MEMS IMUs represent the most affordable class of IMUs.

The drawback, of course, is that the accuracy of an INS using a MEMS IMU will degrade much faster over time than an INS using a higher quality IMU. The errors in a MEMS-based INS will quickly grow without bounds with no feedback corrections. This problem is alleviated in this research by estimating the errors in the INS through the use of a Kalman filter and GPS measurements. Feedback corrections are then made to the INS at a 1-Hz rate.

1.2 Problem Definition

The primary objective of this research is to develop an affordable head tracker that will provide real-time attitude of the user's head with respect to the local-level reference frame, independent of aircraft attitude under typical general aviation flight and ground conditions. To meet AFRL/HE specifications, the head tracker should provide orientation accuracy of ± 3 degrees, and data latency should be minimized as much as possible [13]. The head tracker will consist of an integrated MEMS-based INS/GPS system.

1.3 Related Research

1.3.1 Head Trackers. Most head tracker research has been accomplished in the area of augmented reality, in which 3D virtual objects are integrated into a 3D real environment in real time [2]. Rolland [26] summarizes the current techniques for head tracking. These techniques, described below, fall into six categories: time of flight, spatial scan, mechanical linkages, phase-difference sensing, direct field sensing, and inertial sensing.

Time of flight techniques include using ultrasonic or pulsed infrared laser diode measurements. *Spatial scan* covers all optical and beam-tracking techniques. *Mechanical linkage* uses an assembly of mechanical parts between a fixed reference and the user. Orientation is computed from various linkage angles. *Phase-difference sensing* measures the relative phase of an incoming signal and compares it to a signal of the same frequency located on a fixed reference. *Direct field sensing* includes tracking techniques using either magnetic or gravitational fields. *Inertial sensing* uses inertial measurements from accelerometers and gyroscopes. All of these techniques except direct field sensing and inertial sensing require the use of measurements to a fixed reference [26]. This is not a problem for systems designed for virtual or augmented reality, but obviously becomes a problem for the general aviation application. Once again, the goal is to provide orientation of the user's head with respect to the local-level reference frame. Using a fixed reference inside the cockpit would only provide orientation of the user's head with respect to the aircraft. It is true that if the aircraft attitude information with respect to the local-level reference frame was available, then head position relative to the local-level reference frame could be derived using a fixed reference inside the cockpit. Most general aviation aircraft do not have digital attitude information readily available for such use. It is desirable to keep the proposed system low cost and stand alone so these methods are not practical. Sensors that measure the earth's magnetic field can potentially be used, but the earth's magnetic field is not homogeneous. Furthermore, any disturbances

in the ambient magnetic field, which are quite likely inside a cockpit, will also cause angular errors in the orientation estimates. This leaves inertial sensing to accomplish the task.

Foxlin [10] examined the use of use of inertial sensors for head tracking. His system was based on three orthogonal solid-state rate gyros, a two-axis fluid inclinometer and a two-axis fluxgate compass. Orientation was determined by integrating angular rates from the gyros starting from a known initial orientation. Drift compensation was accomplished by using the inclinometer and compass as a “noisy and sloshy but drift-free” measurement of orientation. Estimates of orientation were then generated using a Kalman filter and both sources of orientation. Foxlin implemented an adaptive algorithm by increasing the estimate of inclinometer measurement noise during periods of slosh. On the other hand, the estimate of measurement noise was decreased at a specified length of time since the last nonzero gyro reading or last change in the inclinometer reading. In this way, the Kalman filter took advantage of the inclinometer and compass measurements when they were the most accurate (with no head motion). This technique would not be advantageous in an aviation environment, because several phases of flight, including takeoff and coordinated turns, are exposed to sustained constant linear acceleration.

Optical cameras were used to aid inertial tracking in research done by Chai, et al [5]. They developed a system that used head-mounted cameras and computer vision techniques to locate and track naturally occurring features in a scene. It could estimate angular orientation, angular rates, as well as translational position, velocity, and acceleration of the camera with respect to an arbitrary reference frame. The system used two extended Kalman filters. One was used to estimate the position of up to five points in the scene, and the other was used to estimate the dynamics of the user’s head. Measurements were taken from three types of sensors: gyroscopes, accelerometers, and cameras. However, synthetic inertial sensor data was used because their system did not allow for simultaneous recording of video imagery and inertial

sensor data. Using this technique as well as other inertial-optical tracking techniques would become more complicated in the aviation environment. Points being tracked by the camera could be inside or outside the cockpit. An algorithm to distinguish between the two types of points would have to be developed.

1.3.2 Low Cost IMU/GPS Integration. With low cost IMU technology expanding, several authors have written on the topic of low cost INS/GPS integration. Van Graas, et al [15, 29, 32] have explored many aspects of using low-cost INS/GPS integration in the aviation environment. They have developed a performance evaluation of low cost inertial systems to include a frequency analysis to characterize gyro bandwidth. Using GPS carrier-phase measurements, they were able to achieve between 0.1-1 degrees of attitude accuracy. Much of their work investigated GPS code/carrier tracking loop aiding as well as INS coasting during GPS outages [15]. Although GPS tracking loop aiding is not directly applicable to this thesis research, they also concede that attitude determination is the least demanding application for a strapdown IMU from an accuracy perspective [15]. Van Grass, et al have also achieved high accuracy results using a segmented processing technique [32]. Stand-alone GPS processing was performed using adjusted double differences, and data from the low-cost IMU was combined with the GPS carrier-phase data using only velocity and attitude states. Position was estimated using code measurements and a different Kalman filter.

Ellum, et al [9] have proposed a method for obtaining attitude without using gyros at all. They remove GPS-derived accelerations from the specific forces measured by MEMS-based accelerometers to determine a gravity vector in the body frame. Pitch and roll can be calculated from the gravity vector, and they use the GPS measured trajectory to determine azimuth. This technique, although intriguing, is not suited for this application. Azimuth is determined by the GPS-measured trajectory which would not correspond to the direction a user is facing. Furthermore,

the GPS-measured trajectory would not necessarily correspond to aircraft heading depending on wind conditions.

Yang, et al [36] performed testing on a two-antenna GPS/INS system. Using relative carrier-phase differential GPS, attitude could be determined in two axes with a known moment arm between the two antennas. This attitude information could be used to estimate the errors of a low-cost IMU. One benefit of this technique was that heading information was always available. Normally, heading error is unobservable unless the vehicle is accelerating. Because baselines of at least one meter are needed for accurate GPS attitude determination, it would not be feasible to implement this system as a head tracker even if the canopy configuration provided a clear view of the sky above the user's head.

1.4 Assumptions

Several assumptions were made in this research. Head orientation in an aviation environment is the primary focus. Head tracking performance in other environments is not considered. Although position and velocity estimates are evaluated, system performance is based on attitude accuracy. It is assumed that GPS-level positioning is adequate for the 3D audio head tracking application. No simulation of the system is accomplished, and all results are based on more accurate reference truth data. Tuning of the Kalman filter was also accomplished using reference truth data. All software development was accomplished in MATLAB®, and all processing was accomplished on a Pentium 4 laptop. Although GPS-out operation is noted, the system is designed based on constant GPS availability during operation. The focus of this thesis is the INS/GPS integration that is the foundation of the head tracker and does not address the design and implementation of 3D audio hardware or software.

1.5 Methodology

The first phase of this research was to learn the fundamentals needed to implement a strapdown INS/GPS integration algorithm. The algorithm was tested using prerecorded IMU and GPS data. The INS/GPS algorithm was then modified to operate in real time to include the addition of an alignment routine. Once the basic functionality was demonstrated, the system was tested in a dynamic flight environment aboard a U.S. Air Force C-12C aircraft under several flight conditions. Results are presented and recommendations are made.

1.6 Thesis Overview

Chapter 2 presents background descriptions of the subsystems to include relevant information on inertial navigation, Kalman filtering, INS/GPS integration, and the test hardware. In Chapter 3, the INS mechanization is detailed along with the design of the Kalman filter. In addition, the real-time software is briefly described. Results of the flight test are presented in Chapter 4. Finally, Chapter 5 presents conclusions, a summary of results, and recommendations for future research.

II. Background

2.1 Overview

This chapter gives some general background information on the different components that make up the head tracker system. The first section will introduce inertial navigation. The second section will provide some details on GPS. The next section will cover the general Kalman filter equations used for integrating the inertial and GPS information. Details on INS/GPS integration are described, and finally, the last section will introduce hardware and test equipment.

2.2 Inertial Navigation

2.2.1 Basic Principles. Inertial navigation at its basic level is dead reckoning – estimating your position by using course, speed, time, and a previously known position. The term dead reckoning has its origins from sailors centuries ago. These pioneers kept detailed logs in order to create maps and pass along information. The entries in these logs often included the source of their navigation, and one common entry was deduced reckoning which was sometimes abbreviated as d’ed reckoning. Over time the apostrophe was lost (ded reckoning), and finally others corrected what they perceived to be a misspelling. The result was the phrase dead reckoning [28].

A modern INS keeps track of position and orientation in the same manner as early sailors but with much greater accuracy and efficiency. An INS measures accelerations and angular rates relative to inertial space using accelerometers and gyroscopes. The output of accelerometers contain both gravitational and inertial forces. The sensor cannot distinguish between specific forces due to gravitational attraction and specific forces due to acceleration [3, 8]. Because of this, knowledge of the earth’s gravitational field must be known in order to obtain the desired inertial acceleration used to navigate.

Raw specific forces and angular rates are measured in the body frame relative to inertial space. However, users often want to know orientation and position relative to their surroundings. To accomplish this, the specific force vector can be transformed into another coordinate system or reference frame. Frequently, the local-level reference frame is used. This reference frame, sometimes referred to as the geographic frame or the navigation frame, has its origin at the system's location and axes aligned with north, east, and down. The down direction is defined to be normal to a reference ellipsoid, and north is the projection of the earth's angular velocity vector into the local horizontal plane (i.e., the plane perpendicular to the down direction) [3]. East completes the orthogonal set. Navigation in this frame can take place in the following manner. Angular rates from the gyroscopes provide information about sensor orientation with respect to the reference frame, and the acceleration vector resolved in the navigation frame is then integrated once to obtain velocity and twice to obtain position.

2.2.2 Attitude Representation. In a strapdown system, the triad of accelerometers and gyroscopes contained in the IMU are fixed to the body of interest. A method to transform vectors in the body frame to vectors in the desired reference frame is needed. Several methods are available to include Euler angles, the Direction Cosine Matrix (DCM), the rotation vector, and quaternions [22]. In this research, Euler angles and the DCM are used due to their ease of use and adequacy for this application (e.g., pitch angles at or near $\pm 90^\circ$ are not expected).

Euler angles are often used to represent the attitude of a vehicle with respect to the local-level reference frame. This is convenient because the set of Euler angles ψ , θ , and ϕ directly correspond to the heading, pitch, and roll of the body with respect to the reference frame. Formally, Euler angles determine a coordinate frame transformation as a result of three successive rotations about different axes in which the order of the rotations is important [22]. Typically, rotations are ordered z -axis (pointing down from the fuselage), y -axis (pointing out the right wing), and x -axis

(pointing out the nose of the aircraft). A different order would result in a different transformation.

The Direction Cosine Matrix is a 3 x 3 matrix with columns that represent unit vectors in the body axes projected along the reference axis [31]. A vector in one reference frame can be transformed to a vector in another reference frame by pre-multiplying the original vector by the appropriate DCM. For example, the transformation of the vector \mathbf{x} from the a -frame to the b -frame can be represented by

$$\mathbf{x}^b = \mathbf{C}_a^b \mathbf{x}^a \quad (2.1)$$

where \mathbf{C}_a^b is the DCM from a to b .

A DCM can be related to Euler angles. For example, to form the body-frame-to-navigation-frame DCM, \mathbf{C}_b^n is constructed from the product of three individual DCMs representing Euler rotations about the x , y , and z axes [22].

$$\mathbf{C}_b^1 = \begin{bmatrix} 1 & 0 & 0 \\ 0 & \cos \phi & -\sin \phi \\ 0 & \sin \phi & \cos \phi \end{bmatrix} \quad (2.2)$$

$$\mathbf{C}_1^2 = \begin{bmatrix} \cos \theta & 0 & \sin \theta \\ 0 & 1 & 0 \\ -\sin \theta & 0 & \cos \theta \end{bmatrix} \quad (2.3)$$

$$\mathbf{C}_2^n = \begin{bmatrix} \cos \psi & -\sin \psi & 0 \\ \sin \psi & \cos \psi & 0 \\ 0 & 0 & 1 \end{bmatrix} \quad (2.4)$$

where \mathbf{C}_b^1 is the rotation about the x axis through angle ϕ , \mathbf{C}_1^2 is the rotation about the y axis through angle θ , and \mathbf{C}_2^n is the rotation about the z axis through angle ψ .

The complete DCM is then

$$\mathbf{C}_b^n = \mathbf{C}_2^n \mathbf{C}_1^2 \mathbf{C}_b^1 \quad (2.5)$$

Completing the matrix multiplication gives

$$\mathbf{C}_b^n = \begin{bmatrix} \cos \psi \cos \theta & \cos \psi \sin \theta \sin \phi - \sin \psi \cos \phi & \cos \psi \sin \theta \cos \phi + \sin \psi \sin \phi \\ \sin \psi \cos \theta & \sin \psi \sin \theta \sin \phi + \cos \psi \cos \phi & \sin \psi \sin \theta \cos \phi - \cos \psi \sin \phi \\ -\sin \theta & \cos \theta \sin \phi & \cos \theta \cos \phi \end{bmatrix}$$

Euler angles can be computed using three elements of the DCM.

$$\theta = -\arcsin[C_{3,1}] \quad (2.6)$$

$$\phi = \arcsin \left[\frac{C_{3,2}}{\cos \theta} \right] \quad (2.7)$$

$$\psi = \arcsin \left[\frac{C_{2,1}}{\cos \theta} \right] \quad (2.8)$$

It should be noted that \mathbf{C}_n^b would entail Euler angles applied in the opposite order, and $\mathbf{C}_n^b = [\mathbf{C}_b^n]^T$ (a very useful property of the DCM).

2.3 Global Positioning System

The Global Positioning System is a satellite-based navigation system that provides position and velocity to an unlimited number of users with GPS receivers. The system is made up of a space segment, control segment, and user segment [19]. The space segment contains a baseline constellation of 24 satellites, although often the constellation will have more than 24 operational satellites, and the system can support up to 30 [19]. The control segment manages the constellation, monitors system performance, and updates the orbital ephemeris data for each satellite. The user segment consists of all GPS receivers.

Receivers determine position through a trilateration process by taking measurements of distance from available satellites. Each distance is determined using a

time-of-arrival technique [24]. By knowing when a signal was transmitted, the speed of signal travel, and the time that the signal was received, distance can be determined. In order for this method to be useable, an accurate time reference must be available at the transmitter and at the receiver. The satellites have atomic clocks to maintain accurate time, and receivers derive accurate time by taking measurements from at least 4 satellites. The 4 measurements are needed to solve for 4 unknowns: an x, y, z position and δt , the receiver clock error [24]. Since the initial range measurement from a satellite contains the clock error, it is called a pseudorange. Besides clock error, each pseudorange generally contains less significant error from a variety of sources which are detailed in [19].

For this distance to be useful, the receiver must be able to calculate the position of the satellite that made the transmission. The receiver calculates satellite position using the orbital ephemeris data sent in a 50 bps navigation message contained in the transmitted signal [19]. Knowing the dynamics of the satellite also allows for receiver velocity determination. Velocity can be calculated by measuring the Doppler shift of the signal carrier frequency [31].

The code contained in the signal that allows for time stamping is generated using pseudo-random noise or a binary sequence that appears to be random. GPS uses two classes of code, Course-Acquisition (C/A) code and Precise (P) code. The P-code, only available to select users through an encryption process, is generated at a rate 10 times that of the C/A-code and provides more precise pseudorange measurements [24]. The INS/GPS integration of this research uses a C/A-code based solution since the GPS receiver being used is a civilian receiver. The reference data used for analysis, however, comes from a P-code based solution using a military keyed receiver.

2.4 Kalman Filters

The Kalman filter is an optimal linear estimator based on linear stochastic system models driven by white Gaussian noise and implemented in a recursive data processing algorithm [16]. It has the capability to incorporate information of known statistical precision properties to provide the best estimates of the variables of interest. The Kalman filter contains a dynamics model of the system of interest as well as a model of measurement errors. It uses statistical information regarding the uncertainty in the dynamics model, measurement errors, and initial conditions to accomplish its task. The filter enters a propagate-update cycle using the internal model equations and new measurements as they become available. This cycle can be described as the propagation of a conditional probability density for quantities of interest, conditioned on data available from measurements. The Kalman filter operates on three basic assumptions: the systems dynamics are described by a linear model, all noise processes are white (i.e., not correlated in time), and all noise processes are jointly Gaussian. The following Kalman filter background section is based on the Kalman filter development presented by Maybeck in [16].

2.4.1 Stochastic Difference Equation. The physical system model that the Kalman filter uses takes the form of a linear state equation driven by white Gaussian noise. Consider the linear stochastic differential equation:

$$d\mathbf{x}(t) = \mathbf{F}(t)\mathbf{x}(t)dt + \mathbf{G}(t)d\boldsymbol{\beta}(t) \quad (2.9)$$

where

$\mathbf{x}(t)$ = the n-dimensional system state vector

$\mathbf{F}(t)$ = the n-by-n state dynamics matrix

$\mathbf{G}(t)$ = the n-by-s noise input matrix

$\boldsymbol{\beta}(\cdot, \cdot)$ = the s-dimensional Brownian motion vector of diffusion $\mathbf{Q}(t)$

The discrete-time equivalent stochastic difference equation [16] is

$$\mathbf{x}(t_{i+1}) = \boldsymbol{\Phi}(t_{i+1}, t_i)\mathbf{x}(t_i) + \mathbf{w}_d(t_i) \quad (2.10)$$

where

$\mathbf{x}(t_i)$ = the n-dimensional system state vector

$\boldsymbol{\Phi}(t_{i+1}, t_i)$ = the n-by-n state transition matrix

The discrete-time white Gaussian dynamics driving noise, \mathbf{w}_d , is given as

$$\mathbf{w}_d(t_i) = \int_{t_i}^{t_{i+1}} \boldsymbol{\Phi}(t_{i+1}, \tau)\mathbf{G}(\tau)\mathbf{d}\boldsymbol{\beta}(\tau) \quad (2.11)$$

with statistics

$$E\{\mathbf{w}_d(t_i)\} = \mathbf{0} \quad (2.12)$$

$$E\{\mathbf{w}_d(t_i)\mathbf{w}_d^T(t_i)\} = \mathbf{Q}_d(t_i) = \int_{t_i}^{t_{i+1}} \boldsymbol{\Phi}(t_{i+1}, \tau)\mathbf{G}(\tau)\mathbf{Q}(\tau)\mathbf{G}^T(\tau)\boldsymbol{\Phi}^T(t_{i+1}, \tau)d\tau \quad (2.13)$$

$$E\{\mathbf{w}_d(t_i)\mathbf{w}_d^T(t_j)\} = \mathbf{0}, t_i \neq t_j \quad (2.14)$$

2.4.2 State Transition Matrix. The state transition matrix $\boldsymbol{\Phi}$ used in the stochastic difference equation “transitions” the states from time t_i to time t_{i+1} . The

state dynamics matrix Φ is related to F , in that it satisfies the parent differential equation and initial condition

$$\frac{d}{dt} [\Phi(t, t_o)] = F(t)\Phi(t, t_o) \quad (2.15)$$

$$\Phi(t_o, t_o) = I \quad (2.16)$$

If F is time invariant, then Φ can be expressed as a matrix exponential:

$$\Phi(t_{i+1}, t_i) = \Phi(t_{i+1} - t_i) = e^{F(\Delta t)} \quad (2.17)$$

2.4.3 Measurement Model. Each available measurement can be expressed as a linear combination of the state variables and additive measurement noise:

$$z(t_i) = H(t_i)x(t_i) + v(t_i) \quad (2.18)$$

where

$z(t_i)$ = the m-dimensional measurement vector

$H(t_i)$ = the m-by-n measurement model matrix

$v(t_i)$ = the m-dimensional vector of additive measurement noise

The noise $v(\cdot, \cdot)$ is modeled as a discrete-time white Gaussian noise with

$$E\{v(t_i)\} = 0 \quad (2.19)$$

$$E\{v(t_i)v^T(t_j)\} = \begin{cases} R(t_i) & \text{for } t_i = t_j \\ 0 & \text{for } t_i \neq t_j \end{cases} \quad (2.20)$$

2.4.4 Incorporating Measurements into the Estimates. When a measurement comes available at time t_i , we would like to incorporate the measurement and update the states and associated error covariance from t_i^- to t_i^+ . This is accomplished using the following equations:

$$\mathbf{K}(t_i) = \mathbf{P}(t_i^-) \mathbf{H}^T(t_i) [\mathbf{H}(t_i) \mathbf{P}(t_i^-) \mathbf{H}^T(t_i) + \mathbf{R}(t_i)]^{-1} \quad (2.21)$$

$$\hat{\mathbf{x}}(t_i^+) = \hat{\mathbf{x}}(t_i^-) + \mathbf{K}(t_i) [\mathbf{z}(t_i) - \mathbf{H}(t_i) \hat{\mathbf{x}}(t_i^-)] \quad (2.22)$$

$$\mathbf{P}(t_i^+) = \mathbf{P}(t_i^-) - \mathbf{K}(t_i) \mathbf{H}(t_i) \mathbf{P}(t_i^-) \quad (2.23)$$

2.4.5 Propagating State Estimates and Error Covariance. Propagation takes place between two measurements. In general, we want to propagate the state estimates and associated error covariance from a time just after one measurement to a time just prior to the next measurement. This can be depicted as a time propagation from t_i^+ to t_{i+1}^- . The equations that accomplish this propagation are

$$\hat{\mathbf{x}}(t_{i+1}^-) = \Phi(t_{i+1}, t_i) \hat{\mathbf{x}}(t_i^+) \quad (2.24)$$

and

$$\mathbf{P}(t_{i+1}^-) = \Phi(t_{i+1}, t_i) \mathbf{P}(t_i^+) \Phi^T(t_{i+1}, t_i) + \mathbf{Q}_d(t_i) \quad (2.25)$$

where $\mathbf{P}(t_{i+1}^-)$ is the conditional covariance of $\mathbf{x}(t_{i+1})$ before the measurement $\mathbf{z}(t_{i+1})$ is incorporated.

2.4.6 Covariance Analysis. A covariance analysis uses analytical comparison of error committed by the filter to help determine performance. It compares the “true” filter’s accuracy with the filter’s own predicted accuracy. If the predicted accuracy matches the actual accuracy, the filter is well “tuned”. To determine the actual accuracy of the filter, a truth model (often of considerably higher state dimensionality than the filter design model) or more accurate reference data must be used. To achieve the best possible Kalman filter performance, the designer can iterate on the values of \mathbf{P}_o , \mathbf{Q} , and \mathbf{R} assumed by the filter until the filter errors are minimized and the actual errors committed by the filter match its own prediction as seen in the

standard deviations (one-sigma values) taken from the time history of the covariance matrix \mathbf{P} . By accomplishing this error matching, the actual filter state estimates will be more accurate, thereby improving overall system performance [17].

2.5 INS/GPS Integration

As mentioned in Chapter 1, an INS solution will degrade over time. This is due to sensor errors, misalignment errors, and computational errors, but is mostly due to imperfections in any physical gyro. If an INS is going to be useful for the long term, a method is needed that will allow measurements from one or more independent navigational sources to be used. These independent sensors with long-term error stability can complement the short-term error stability of an INS [25]. For example, if altitude is available from a barometric altimeter, and its error characteristics are stable in the long term, then it can be used to aid the unstable free inertial solution. The Kalman filter described in the previous section is the preferred tool to accomplish this type of integration.

2.5.1 State Space Formulation. In a *total state space formulation*, the Kalman filter estimates parameters of interest such as position, velocity, and attitude. In this formulation, the Kalman filter is contained inside the INS mechanization and therefore must operate at a high sample rate to capture all dynamics of the body of interest. In addition, the system is described by nonlinear dynamics not well suited for a Kalman filter. As a consequence, this formulation is generally restricted to alignments, calibrations, and slower dynamic applications such as submarine inertial systems [16]. As an alternative, the *error state formulation* estimates the errors committed by the INS. Measurements are formed from the difference in INS outputs and corresponding outputs from other navigational aids. In contrast to the total state filter, the dynamics are well modeled as linear processes with low frequency content. For example, the INS error in position, velocity, and attitude changes much

slower than changes in the actual total variables. The INS/GPS integration in this research utilizes the error state formulation.

2.5.2 Feedforward and Feedback Implementations. The two mechanization schemes to apply Kalman filter estimates are feedforward and feedback. In the feedforward implementation, depicted in Figure 2.1, the Kalman filter estimates are used to correct the final position, velocity, and attitude solution. The INS is left autonomous, and its errors are allowed to accumulate. There are advantages and disadvantages to using the feedforward implementation. Advantages include INS protection from bad measurements, as well as the ability for the INS and Kalman filter to run independently [18]. The primary disadvantage is that, as the INS errors are allowed to grow without bounds, the Kalman filter assumption of a linear dynamics model for those errors maybe violated [18]. Therefore the Kalman filter will only be accurate when INS errors are small.

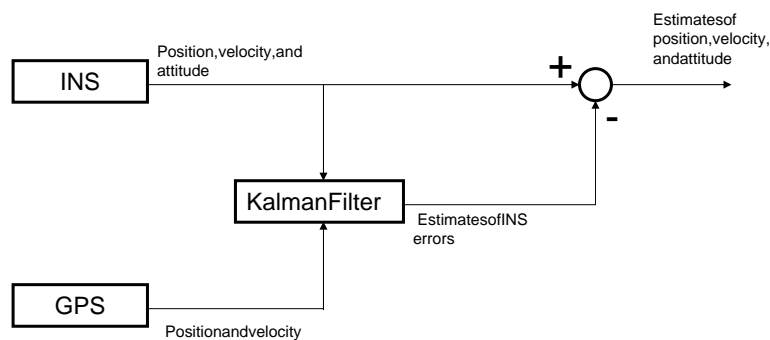


Figure 2.1 Error State Feedforward Implementation

In the feedback implementation, depicted in Figure 2.2, the Kalman filter estimates are used to correct the INS, and the errors are not allowed to grow unbounded. The feedback implementation has advantages and disadvantages as well [18]. The primary advantage is that INS errors are kept small with feedback from the Kalman filter, and the linear model assumption is upheld. On the other hand, any bad measurements incorporated by the Kalman filter will affect the INS also unless the filter can reject any potentially bad measurements before they are incorporated (e.g.,

through residual monitoring). Furthermore, stability problems could arise due to the feedback configuration. This research uses a combination of feedforward and feedback implementations.

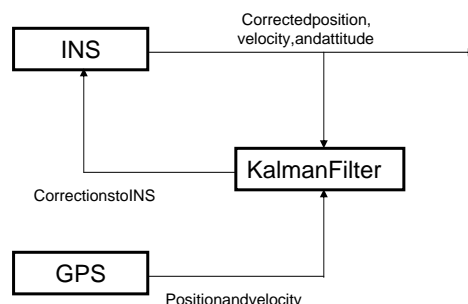


Figure 2.2 Error State Feedback Implementation

2.5.3 INS/GPS Integration Levels. There are several methods to accomplish INS/GPS integration. Two common methods are tightly-coupled integration and loosely-coupled integration. In a tightly-coupled integration, GPS measurements come in the form of pseudoranges and pseudorange rates. Since these measurements are not preprocessed, the noises associated with them more closely follow the white noise Kalman filter assumption. As a result, the estimates from the Kalman filter are more accurate. Another advantage is that INS aiding can take place with a measurement from as few as one satellite, decreasing system sensitivity to satellite dropouts [18]. One of the drawbacks of this configuration, compared to the loosely-coupled configuration, is added complexity to the Kalman filter measurement model. The filter must now be able to calculate each satellite position in order to predict range and range rates to form the measurement. Another disadvantage is that many GPS receivers do not allow access to these “raw” measurements. A tightly-coupled INS/GPS integration is depicted in Figure 2.3.

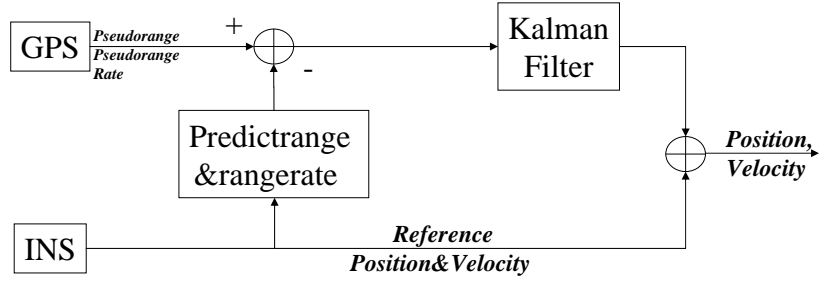


Figure 2.3 Tightly-Coupled INS/GPS Integration [18]

In a loosely-coupled configuration, depicted in Figure 2.4, the GPS measurements come in the form of GPS receiver-computed position and/or velocity. The advantage of this integration method is that it can be accomplished with any GPS receiver that provides a digital output of its solution. The benefits of GPS can be obtained without extensive modifications to an existing navigation system. Also, there are potentially two independent navigation solutions, which is advantageous if one system fails. The largest disadvantage to this configuration is that the measurements being passed to the navigation Kalman filter are being generated by a filter in the GPS receiver, a filter-feeding-filter situation. As a result, the measurement noise is not white, and the estimates from the Kalman filter are not optimum and are degraded in accuracy [18]. An additional disadvantage to the loosely-coupled integration is the need for at least 4 satellites to provide a measurement. A loosely-coupled configuration is used in this research to mitigate risk in this first implementation of this real-time algorithm.

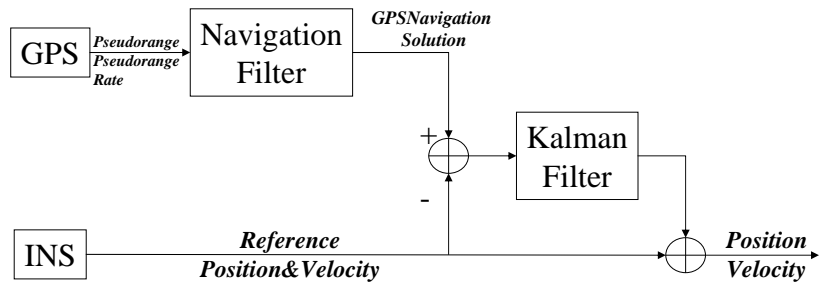


Figure 2.4 Loosely-Coupled INS/GPS Integration [18]

2.6 Hardware/Test Equipment

2.6.1 Inertial Measurement Unit. The Xsens MT9-B outputs raw binary sensor data from a triad of accelerometers, gyros, and magnetometers via an RS-232 serial connection. The IMU can sense angular velocity up to ± 450 degrees/second and accelerations up to ± 50 meters/second². The device is lightweight at only 35 grams and relatively small with dimensions 39 x 54 x 28 mm (W x L x H) [35] as seen in Figure 2.5. The sample frequency can be set between 10 Hz and 512 Hz. A sample rate of 100 Hz was selected for this research. Factory calibration data is provided for orthogonalization, scaling and offset corrections. Gyro drift rates were not published.



Figure 2.5 Xsens MT9 Inertial Measurement Unit

2.6.2 GPS Receiver. The Garmin GPS 35, depicted in Figure 2.6, is a 12 channel C/A-code GPS receiver with embedded antenna [11]. Data is transmitted via an RS-232 serial connection using sentences defined by NMEA 0183 ASCII interface protocol as well as various Garmin proprietary sentences. The receiver also provides a One-Pulse-Per-Second (1PPS) output. The rising edge of the pulse is synchronized to the start of each GPS second. This pulse is used in the time synchronization of the IMU and GPS data.



Figure 2.6 Garmin GPS 35 Receiver

2.6.3 Pentium 4 Laptop. Real-time processing was accomplished on a Dell Pentium 4 laptop running Microsoft Windows 2000. Two additional serial ports were added with the use of a dual serial PCMCIA interface card.

2.6.4 Truth Data . The Time, Space, and Position Information (TSPI) truth data was provided by a multi-sensor optimal smoother estimation algorithm that post-processed differential GPS data and INS data (independent of the IMU and GPS receiver just described) to produce an optimal Kalman filter/smoothing trajectory estimate [6]. Equipment onboard the aircraft, as shown in Figure 2.7, consisted of a GPS Aided Inertial Navigation Reference (GAINR) system. The heart of the GAINR system is the Honeywell H-764G-TSPI Embedded GPS/Inertial Navigation System that can be keyed to accept GPS P code measurements. Data from the GAINR system is recorded on PCMCIA media. The optimal smoother algorithm accepts reference receiver differential corrections collected by a static Ashtech Z-12 or Ashtech ZY-12 GPS receiver [6]. The smoother algorithm was developed for the Air Force Flight Test Center (AFFTC) by the TSPI department of Computer Sciences Corporation, Edwards AFB. Estimated 1σ accuracies for the truth data are depicted in Table 2.1.

Table 2.1 Estimated TSPI Accuracy (1σ)

Parameter	Value	Units
Position	0.8	ft
Velocity	0.01	ft/sec
Acceleration	0.01	ft/sec ²
Attitude	0.05	deg



Figure 2.7 GPS Aided Inertial Navigation Reference (GAINR) Equipment

2.6.5 Test Aircraft. Testing was conducted in a C-12C Huron. The C-12C is a Raytheon King Air twin-engine transport aircraft. The aircraft is powered by two Pratt and Whitney PT6A-42 turboprops providing 850 shp per engine. Max speed is 339 knots, service ceiling is 25,000 feet, and operating weight is approximately 8,000 lbs. The aircraft requires a basic crew of two to operate [12] but held a crew of 4 during testing. Figure 2.8 is an in-flight photograph of the C-12C.



Figure 2.8 C-12C Huron

2.7 Summary

This chapter has provided a basic overview of inertial navigation and GPS. The essential equations for discrete-time Kalman filtering were presented. Key mechanization schemes of INS/GPS integration were discussed. Finally, hardware and test equipment were introduced.

III. Methodology and Algorithm Development

3.1 Overview

This chapter will detail the design and application of the algorithm used for the real time integrated INS/GPS system. It will begin with the development of the INS mechanization and follow with the Kalman Filter and GPS measurement scheme. Next the feedback methodology is described, and finally the real-time software is discussed. Figure 3.1 depicts the INS/GPS integration algorithm.

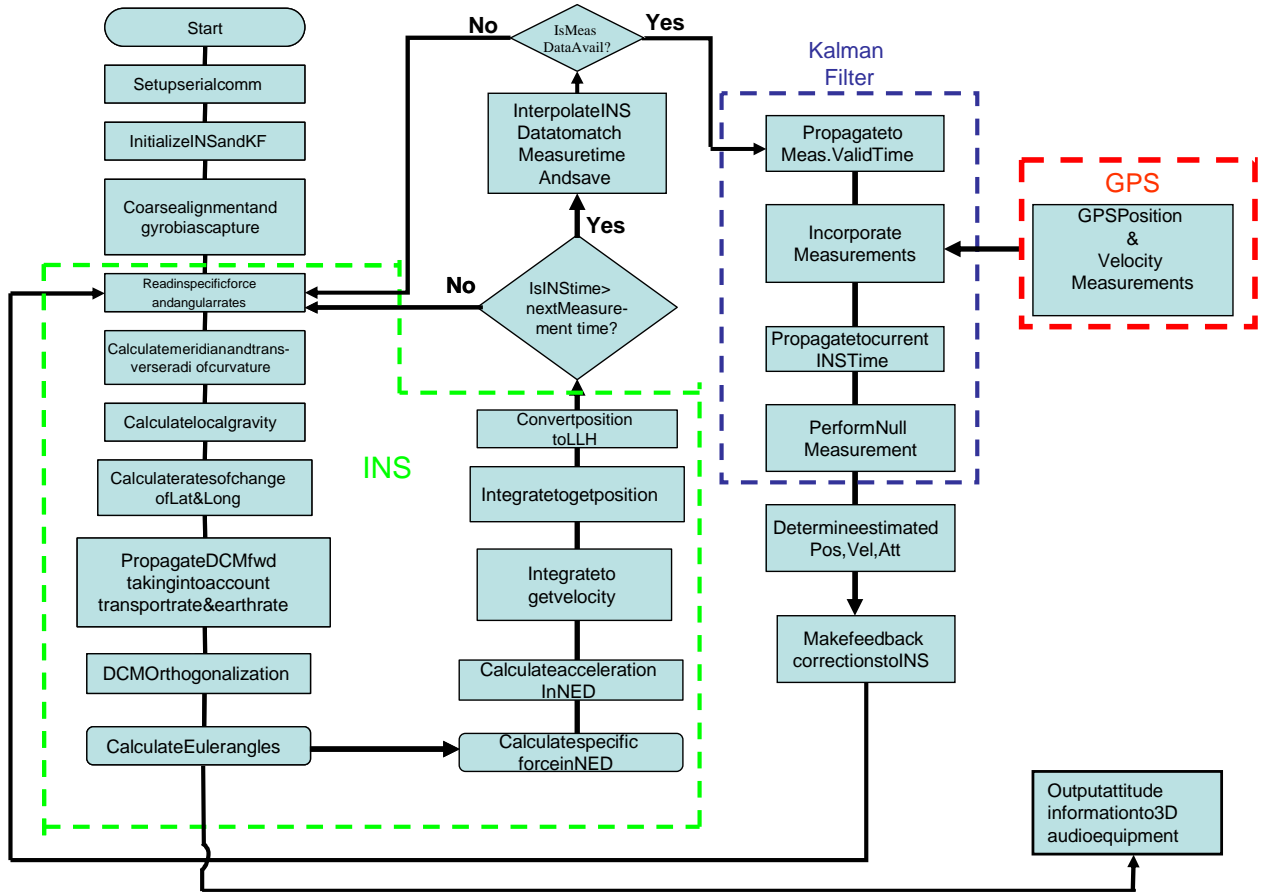


Figure 3.1 INS/GPS Integration Flowchart

3.2 Inertial Navigation System

Based on the requirements of the head tracker and the equipment being used, a local-level strapdown INS mechanization is used. The MEMS IMU requires the strapdown algorithm, and the system should provide attitude information of the user's head with respect to the local-level reference frame. The INS mechanization that is used in this real time algorithm is based largely on the strapdown INS fundamentals presented by Titterton and Weston [31].

3.2.1 INS Alignment. The INS has two modes for alignment. One mode is used for stationary alignment and the second is used for in-motion alignment. Both modes use the GPS position solution for its initial position and the local gravity vector for levelling. Straight-and-level unaccelerated flight is maintained for in-motion alignments in order to allow the levelling process to work. The algorithm averaged 300 samples of IMU data (sampled at 100Hz) to form the initial body-frame-to-navigation-frame DCM \mathbf{C}_b^n as described in Equations (2.2) through (2.5) in Section 2.2.2.

Since alignments take place when the IMU is in a nonaccelerating environment relative to the local-level reference frame, the only specific force measured by the accelerometers is the local gravity vector. The components of gravity measured in the body frame of the IMU are used to determine ϕ and θ (levelling).

The angle ϕ is the rotation about the x axis required to zero out the measured y component of gravity \mathbf{g}^b in the body frame. Using a 4 quadrant arctan function,

$$\phi = \arctan \left[\frac{\mathbf{g}_z^b}{\mathbf{g}_y^b} \right] \quad (3.1)$$

The angle θ is the rotation about the y axis required to zero out the measured x component of gravity \mathbf{g}^1 in the first intermediate frame. Using a 4 quadrant arctan

function,

$$\theta = \arctan \left[\frac{\mathbf{g}_z^1}{\mathbf{g}_x^1} \right] \quad (3.2)$$

where $\mathbf{g}^1 = \mathbf{C}_b^1 \mathbf{g}^b$.

Traditionally, ψ is initialized as the rotation about the z axis required to zero out the y component of earth rate (gyrocompassing). However, the gyros on the MT9 are not sensitive enough to measure Earth rotation. Initial heading is therefore determined using other methods. For static alignments, the magnetometers on the MT9 are used. The horizontal component of the earth's magnetic field vector, \mathbf{m} , points toward the magnetic north pole. The first two rotations are used to resolve the horizontal component, and then ψ' is the angle of rotation about the z axis required to align the x axis with magnetic north. Magnetic variation is then applied to determine ψ , rotation to true north. Local magnetic variation is provided by the GPS receiver based on its current position solution. Using a 4 quadrant arctan function,

$$\psi' = \arctan \left[\frac{\mathbf{m}_x^2}{\mathbf{m}_y^2} \right] \quad (3.3)$$

where \mathbf{m}^2 is the earth's magnetic field in the second intermediate frame $\mathbf{m}^2 = \mathbf{C}_1^2 \mathbf{C}_b^1 \mathbf{m}^b$.

Magnetometers are only used to provide initial heading during static alignments. Although heading derived from the magnetometers can be accurate in a benign environment, aircraft strobe lights, moving magnetic-based headsets, and other avionics make magnetometer-derived heading problematic. During in-motion alignments, GPS course information is used to provide the initial heading. This is not optimal since course and heading may differ depending on the winds aloft, but GPS course is the best azimuth information available to align INS heading. Therefore, the user looks straight ahead (i.e., align the x axis of the IMU as closely as

possible to the course of the aircraft) and keeps his head still during the in-motion alignment.

The in-motion alignment also uses GPS-provided north, east, and down velocities to initialize the INS as opposed to zero velocity values used in the static alignment. It should also be noted that 300 samples of the x , y , and z gyros are taken during the each alignment process to establish an initial gyro drift, and it is imperative that the user holds his head as still as possible in the alignment process.

3.2.2 Modeling the Earth.

3.2.2.1 Reference Ellipsoid. The World Geodetic System 1984 (WGS 84) is used as the reference ellipsoid to approximate the actual surface of the earth. This ellipsoid was chosen for three reasons. First, the TSPI data is presented using the WGS 84 datum. Secondly, the Garmin GPS-35 used to aid the INS readily provided WGS 84 measurements, and finally, WGS 84 has become the “*de facto* world standard” [19]. Table 3.1 lists the WGS 84 parameters that are used in the INS mechanization.

Table 3.1 WGS 84 Fundamental Parameters [31]

Parameter	Value
Semi-major axis (a)	6378137.0 m
Major Eccentricity of the Ellipsoid (e)	0.0818191908426
Earth's Rate (Ω)	$7.292115 \times 10^{-5} \frac{rad}{sec}$
Speed of Light in a Vacuum (c)	299792458 $\frac{m}{s}$

3.2.2.2 Local Gravity. Since accelerometers really measure specific force to include gravity, it is important to model and remove the local gravity vector prior to the determination of velocity or position. Otherwise, the IMU would always appear to be accelerating in the up direction. A gravity model is presented in [34]

that takes into account centrifugal potential due to the rotation of the earth and is based on an infinite power series of spherical harmonics. A truncated form of the series is shown below.

$$g = a_1(1 + a_2 \sin^2 L + a_3 \sin^4 L) + (a_4 + a_5 \sin^2 L)h + a_6 h^2 \quad (3.4)$$

where g is the magnitude of the gravity vector orthogonal to the ellipsoid at latitude L and height above the ellipsoid h . The coefficients a_1 to a_6 depend on the parameters of the ellipsoid. For details on the model see [27] and [34]. The motivation for using this model was its accuracy (quoted at $10^{-6}m/s^2$) and its efficiency for numerical computations in a real-time algorithm.

3.2.2.3 Rotating Reference Frame. Because the local-level reference frame is used, both earth rate and transport rate were computed before propagation of \mathbf{C}_b^n . Earth rate in the navigation frame is determined using the following relationship.

$$\boldsymbol{\omega}_{ie}^n = [\Omega \cos L \quad 0 \quad -\Omega \sin L]^T \quad (3.5)$$

At 0 degrees of latitude, all of the earth's angular velocity is in the north direction, and at 90 degrees latitude all of the earth's angular velocity is in the up direction. Any latitude between 0 degrees and 90 degrees will have the appropriate component of angular velocity in the up and north directions.

Transport rate accounts for the rotation of the local-level reference frame as the IMU traverses the ellipsoid (i.e., the navigation frame must be kept locally level [31]). If a tangential velocity and radius are known, then a component of the turn rate can be determined. In order to compute transport rate with respect to the reference ellipsoid, the meridian radius of curvature (R_N) and the transverse radius of curvature (R_E) need to be determined. R_N is the radius of the best fitting circle

to a meridian section of the reference ellipsoid, and R_E is the radius of the best fitting circle to a vertical east-west section of the reference ellipsoid [23]. They are both related to latitude, eccentricity of the ellipsoid, and the semi-major axis of the ellipsoid:

$$R_N = \frac{R(1 - e^2)}{(1 - e^2 \sin^2 L)^{\frac{3}{2}}} \quad (3.6)$$

$$R_E = \frac{R}{\sqrt{1 - e^2 \sin^2 L}} \quad (3.7)$$

As seen in [31], transport rate in the local-level navigation frame can be expressed as

$$\boldsymbol{\omega}_{en}^n = \left[\begin{array}{ccc} \frac{V_E}{R_E + h} & \frac{-V_N}{R_N + h} & \frac{-V_E \tan L}{R_N + h} \end{array} \right]^T \quad (3.8)$$

3.2.3 Propagation of the Direction Cosine Matrix. In order to propagate the body-frame-to-navigation-frame DCM, the body angular rate, $\boldsymbol{\omega}_{nb}^b$, is formed from the gyroscope rates, $\boldsymbol{\omega}_{ib}^b$, and the computed earth rate and transport rate.

$$\boldsymbol{\omega}_{nb}^b = \boldsymbol{\omega}_{ib}^b - \mathbf{C}_n^b (\boldsymbol{\omega}_{ie}^n + \boldsymbol{\omega}_{en}^n) \quad (3.9)$$

A first order DCM propagation takes the form

$$\mathbf{C}_b^n(t + \delta t) = \mathbf{C}_b^n(t) \mathbf{A}(t) \quad (3.10)$$

where $\mathbf{A}(t)$ is a DCM which transforms the body frame at time t to the body frame at time $t + \delta t$.

$$\mathbf{A}(t) = [\mathbf{I} + \delta \boldsymbol{\Psi}] \quad (3.11)$$

\mathbf{I} is a 3 x 3 identity matrix and

$$\delta\mathbf{\Psi} = \begin{bmatrix} 0 & -\omega_z\delta t & \omega_y\delta t \\ \omega_z\delta t & 0 & -\omega_x\delta t \\ -\omega_y\delta t & \omega_x\delta t & 0 \end{bmatrix} \quad (3.12)$$

where $\boldsymbol{\omega}_{nb}^b = [\omega_x \ \omega_y \ \omega_z]^T$. The DCM propagation is valid if $\delta\mathbf{\Psi}$ contains small angles [31]. This is a good assumption in this application since $\delta t = 0.01$ seconds and typical head rotations are estimated to be less than 180 degrees/second. Higher order DCM propagation techniques are available [21, 31]. Nevertheless, this first implementation of the real-time algorithm uses the method described above to ensure computations can be accomplished within the 100-Hz cycle.

3.2.4 DCM Orthogonalization. As the DCM is propagated in time, small errors will be induced from numerical computation. In order to improve the accuracy of the DCM computation, the DCM is reorthogonalized on a periodic basis (once a second). The orthogonality characteristic of the DCM is used to check and maintain the “quality” of the matrix. Each row of the DCM needs to be mutually orthogonal to the other two. To accomplish the orthogonalization, any projection of one row will be removed from the other two. An orthogonalization technique from [31] is used in this INS mechanization and follows below.

$$\Delta_{ij} = \mathbf{C}_i \mathbf{C}_j^T \quad (3.13)$$

$$\hat{\mathbf{C}}_i = \mathbf{C}_i - \frac{1}{2}\Delta_{ij}\mathbf{C}_j \quad (3.14)$$

$$\hat{\mathbf{C}}_j = \mathbf{C}_j - \frac{1}{2}\Delta_{ij}\mathbf{C}_i \quad (3.15)$$

where \mathbf{C}_i and \mathbf{C}_j are the i th and j th rows of the DCM, and Δ_{ij} is the orthogonality error between the two rows. The $\hat{}$ notation is used to denote the corrected quantity. After the DCM undergoes orthogonalization, it is also normalized to maintain its desired ortho-normal properties.

3.2.5 Determining Position and Velocity in the Navigation Frame. With the body-frame-to-navigation-frame DCM in hand, accelerations experienced in the navigation frame are calculated. As developed in [23], acceleration experienced in the navigation reference frame can be expressed as

$$\dot{\mathbf{v}}^n = \mathbf{C}_b^n \mathbf{f}^b - (2\boldsymbol{\omega}_{ie}^n + \boldsymbol{\omega}_{en}^n) \times \mathbf{v}^n + \mathbf{g}^n \quad (3.16)$$

where $\mathbf{C}_b^n \mathbf{f}^b$ is the specific force measured in the navigation frame, $2\boldsymbol{\omega}_{ie}^n \times \mathbf{v}^n$ is the Coriolis term characterizing the acceleration due to velocity over the rotating earth, $\boldsymbol{\omega}_{en}^n \times \mathbf{v}^n$ is the centripetal acceleration due to motion over the earth, and finally \mathbf{g}^n is the local gravity vector. Figure 3.2 illustrates this local-level INS mechanization.

Using simple trapezoidal integration, velocity and position are determined using the new INS time (t_{k+1}) and the previous INS time (t_k):

$$\mathbf{v}_{k+1}^n = \mathbf{v}_k^n + \frac{[\mathbf{a}_k^n + \mathbf{a}_{k+1}^n]}{2} \Delta t \quad (3.17)$$

$$\mathbf{r}_{k+1}^n = \mathbf{r}_k^n + \frac{[\mathbf{v}_k^n + \mathbf{v}_{k+1}^n]}{2} \Delta t \quad (3.18)$$

where \mathbf{a}^n , \mathbf{v}^n , and \mathbf{r}^n are navigation frame acceleration, velocity, and position, respectively.

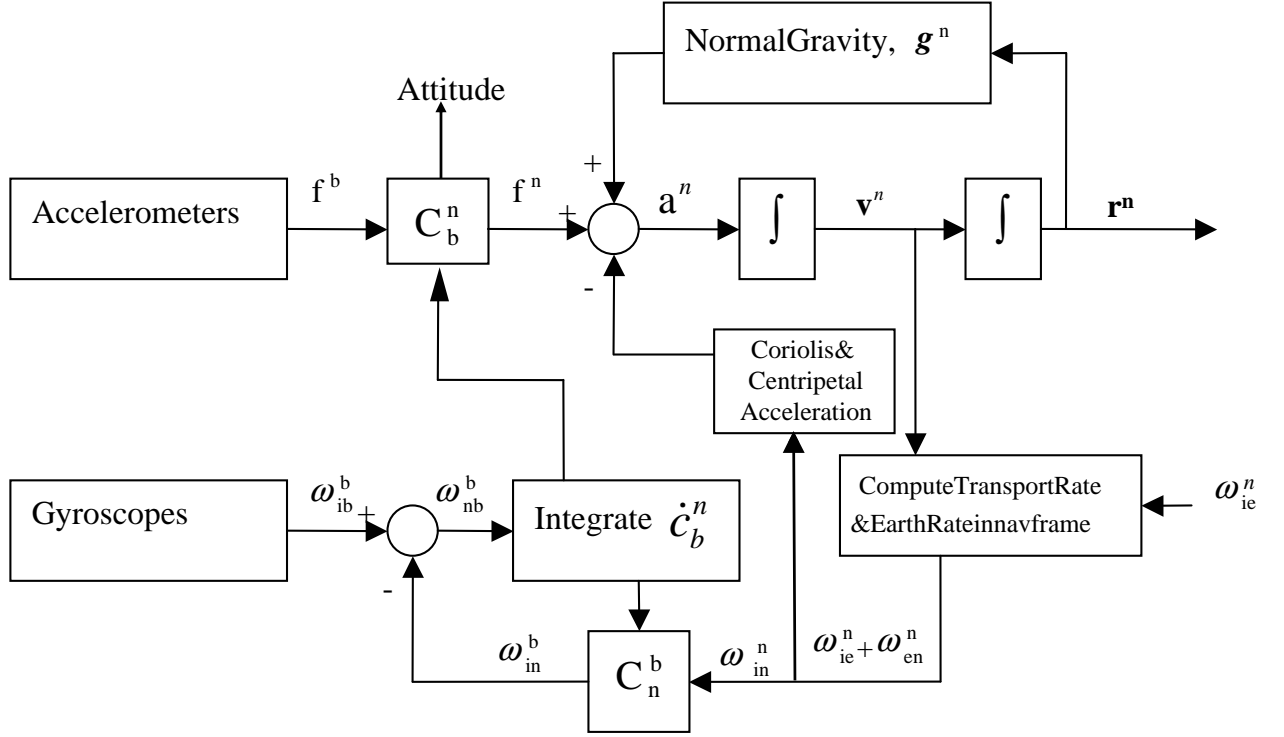


Figure 3.2 Local-Level INS Mechanization Scheme [34]

To get position in WGS 84 latitude (L) and longitude (λ), the meridian radius of curvature (R_N) and the transverse radius of curvature (R_E) are applied:

$$\delta L = \frac{\delta r_N}{R_N + h} \quad (3.19)$$

$$\delta \lambda = \frac{\delta r_E}{(R_E + h) \cos L} \quad (3.20)$$

where δr_N and δr_E are changes in north and east position. Finally roll, pitch, and yaw can be extracted from \mathbf{C}_b^n using Equations (2.6) through (2.8).

3.3 Kalman Filter

The filter design used in this research is based on an error-state implementation of a Kalman filter as described in Section 2.5.1. The state vector has 15 states, which are defined in Table 3.2.

Table 3.2 Kalman Filter State Definitions

x_1	δlat	latitude error (rad)
x_2	δlon	longitude error (rad)
x_3	δalt	height error (m)
x_4	δv_N	north velocity error (m/sec)
x_5	δv_E	east velocity error (m/sec)
x_6	δv_D	down velocity error (m/sec)
x_7	$\delta \alpha$	north tilt error (rad)
x_8	$\delta \beta$	east tilt error (rad)
x_9	$\delta \gamma$	down tilt error (rad)
x_{10}	δf_{x_s}	x accelerometer bias (m/sec^2)
x_{11}	δf_{y_s}	y accelerometer bias (m/sec^2)
x_{12}	δf_{z_s}	z accelerometer bias (m/sec^2)
x_{13}	$\delta \omega_{x_s}$	gyro drift (rad/sec)
x_{14}	$\delta \omega_{y_s}$	gyro drift (rad/sec)
x_{15}	$\delta \omega_{z_s}$	gyro drift (rad/sec)

A Kalman filter is used to improve head tracker performance by estimating the errors in the strapdown INS, and then correcting the INS solution using these estimated errors. The estimates are based on a model of how the INS errors will propagate in time, as well as measurement updates from GPS position and velocity. The implementation of this Kalman filter is based on parameters that define the structure of the models: $\mathbf{F}(\mathbf{t})$ or $\Phi(t_{i+1}, t_i)$, $\mathbf{G}(t)$, and $\mathbf{H}(t_i)$, as well as parameters

that characterized the uncertainties: $\hat{\mathbf{x}}_o$, \mathbf{P}_o , $\mathbf{Q}(t)$, and $\mathbf{R}(t_i)$ [16]. The next section will describe the design and motivation for choosing each of these parameters as they apply to the head tracker Kalman filter.

3.3.1 Dynamics Model. The so-called Pinson error model [31] for a strap-down INS mechanized in the local-level reference frame is used to model the interactions between the first nine states. Some of the terms in the Pinson error model are insignificant for a low quality IMU like the Xsens MT9 used in this research. In spite of this, the full Pinson error model was used in the real-time algorithm, and a performance analysis using a simplified model is accomplished using a post-processing version of the algorithm. Both accelerometer bias and gyro drift are modeled as random walks. Combining the Pinson error model from [31] with the models for the last six states produces the complete dynamics model.

The 15 x 15 dynamics matrix, \mathbf{F} , can be divided into 3 x 3 partitions.

$$\mathbf{F} = \begin{bmatrix} \mathbf{PP} & \mathbf{PV} & \mathbf{0} & \mathbf{0} & \mathbf{0} \\ \mathbf{VP} & \mathbf{VV} & \mathbf{VA} & \mathbf{VB} & \mathbf{0} \\ \mathbf{AP} & \mathbf{AV} & \mathbf{AA} & \mathbf{0} & \mathbf{AD} \\ \mathbf{0} & \mathbf{0} & \mathbf{0} & \mathbf{0} & \mathbf{0} \\ \mathbf{0} & \mathbf{0} & \mathbf{0} & \mathbf{0} & \mathbf{0} \end{bmatrix} \quad (3.21)$$

Each 3 x 3 partition is expanded to describe the dynamics of the differential equation:

Change in Position Error due to Position Error

$$\mathbf{PP} = \begin{bmatrix} 0 & 0 & \frac{-v_N}{R^2} \\ \frac{v_E \tan L}{R \cos L} & 0 & \frac{-v_E}{R^2 \cos L} \\ 0 & 0 & 0 \end{bmatrix}$$

Change in Position Error due to Velocity Error

$$\mathbf{PV} = \begin{bmatrix} \frac{1}{R} & 0 & 0 \\ 0 & \frac{1}{R \cos L} & 0 \\ 0 & 0 & -1 \end{bmatrix}$$

Change in Velocity Error due to Position Error

$$\mathbf{VP} = \begin{bmatrix} -v_E \left(2\Omega \cos L + \frac{v_E}{R \cos^2 L} \right) & 0 & \frac{1}{R^2} (v_E^2 \tan L - v_N v_D) \\ 2\Omega (v_N \cos L - v_D \sin L) + \frac{v_N v_E}{R \cos^2 L} & 0 & -\frac{v_E}{R^2} (v_N \tan L + v_D) \\ 2\Omega v_E \sin L & 0 & \frac{1}{R^2} (v_N^2 + v_E^2) \end{bmatrix}$$

Change in Velocity Error due to Velocity Error

$$\mathbf{VV} = \begin{bmatrix} \frac{v_D}{R} & -2 \left(\Omega \sin L + \frac{v_E}{R} \tan L \right) & \frac{v_N}{R} \\ 2\Omega \sin L + \frac{v_E}{R} \tan L & \frac{1}{R} (v_N \tan L + v_D) & 2\Omega \cos L + \frac{v_E}{R} \\ \frac{-2v_N}{R} & -2 \left(\Omega \cos L - \frac{v_E}{R} \right) & 0 \end{bmatrix}$$

Change in Velocity Error due to Attitude Error

$$\mathbf{VA} = \begin{bmatrix} 0 & -f_D & f_E \\ f_D & 0 & -f_N \\ -f_E & f_N & 0 \end{bmatrix}$$

Change in Velocity Error due to Accelerometer Bias

$$\mathbf{VB} = \mathbf{C}_b^n$$

Change in Attitude Error due to Position Error

$$\mathbf{AP} = \begin{bmatrix} -\Omega \sin L & 0 & \frac{-v_E^2}{R^2} \\ 0 & 0 & \frac{v_N}{R^2} \\ -\Omega \cos L - \frac{v_E}{R \cos^2 L} & 0 & \frac{v_E \tan L}{R^2} \end{bmatrix}$$

Change in Attitude Error due to Velocity Error

$$\mathbf{AV} = \begin{bmatrix} 0 & \frac{1}{R} & 0 \\ -\frac{1}{R} & 0 & 0 \\ 0 & \frac{-\tan L}{R} & 0 \end{bmatrix}$$

Change in Attitude Error due to Attitude Error

$$\mathbf{AA} = \begin{bmatrix} 0 & -\Omega \sin L - \frac{v_E}{R} \tan L & \frac{v_N}{R} \\ \Omega \sin L + \frac{v_E}{R} \tan L & 0 & \Omega \cos L + \frac{v_E}{R} \\ -\frac{v_N}{R} & -\Omega \cos L - \frac{v_E}{R} & 0 \end{bmatrix}$$

Change in Attitude Error due to Gyro Drift

$$\mathbf{AD} = -\mathbf{C}_b^n$$

R is the radius of the earth semi-major axis, Ω is the earth's rotation rate, L is INS latitude, \mathbf{v} is INS velocity in the navigation frame, and \mathbf{f} is specific force resolved in the navigation frame. Terms with the earth's radius in the denominator are small, and R can be used in place of $R_N + h$ and $R_E + h$.

As mentioned before, a random walk is used to estimate accelerometer bias and gyro drift. The bias and the drift appear to vary slowly over time, and the random walk captures this behavior [16]. Stationary IMU data was collected over a 10 minute time period (see Figures 3.3 and 3.4). Notice how the accelerometer bias

trend in Figure 3.3 gradually increases. The x axis gyro drift in Figure 3.4 is fairly constant over the 10 minute period averaging just above -0.04 rad/sec. Output from the other accelerometers and gyros are similar.

The random walk can be modeled as an integrator driven by white Gaussian noise [16].

$$\dot{\mathbf{x}}(t) = 0 + \mathbf{w}(t) \quad (3.22)$$

Since the system is implemented on a digital computer, the state transition matrix, $\Phi(t_{i+1}, t_i)$, is formed as described in Equation (2.17). Admittedly, \mathbf{F} is not truly time invariant between propagation steps. The current INS values are used for position and velocity; it is assumed that these values will not change drastically between propagation steps. On the other hand, specific force measurements and the body to navigation frame DCM are more likely to change between steps. To use more representative quantities than the most recent values from the INS, the discrete values of \mathbf{f}^n , and \mathbf{C}_b^n are collected between propagation steps. The mean values over the propagation period are calculated and used for the propagation step. In this way, the *average* specific force and *average* DCM sensed during the time period of interest are used in the creation of the state transition matrix. We can further compensate for an imperfect system model through the addition of process noise to the dynamics model.

3.3.2 Process Noise. The diagonal matrix \mathbf{Q} carries the strength of the process noise for each state on the diagonal. The noise input matrix \mathbf{G} is a 15 x 15 diagonal matrix and allows for noise input into each state directly.

$$\mathbf{Q} = \begin{bmatrix} Q_1 & & \\ & \ddots & \\ & & Q_{15} \end{bmatrix} \quad (3.23)$$

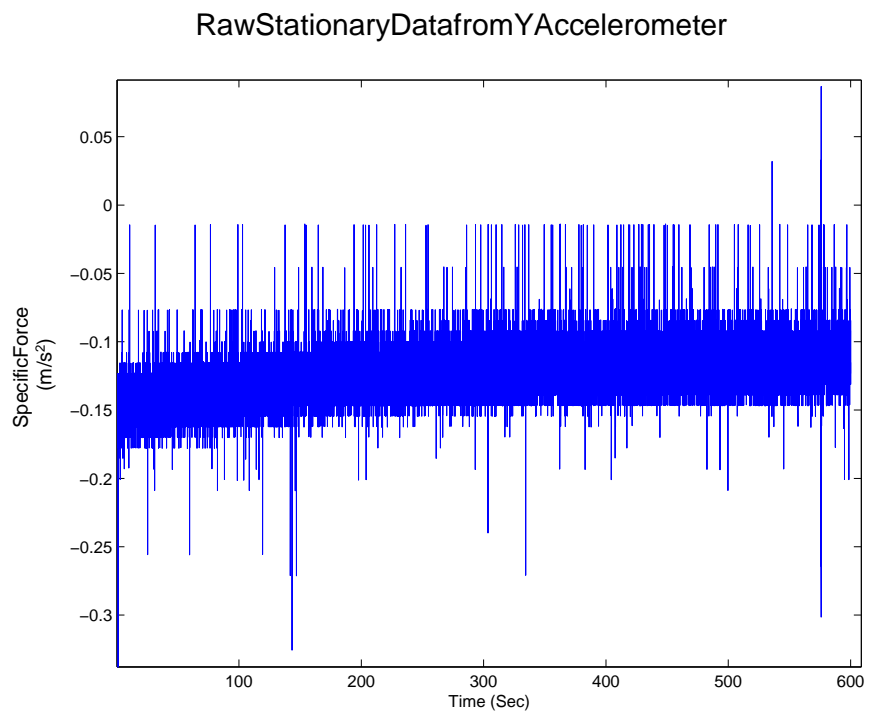


Figure 3.3 Raw Stationary Data from Y Accelerometer

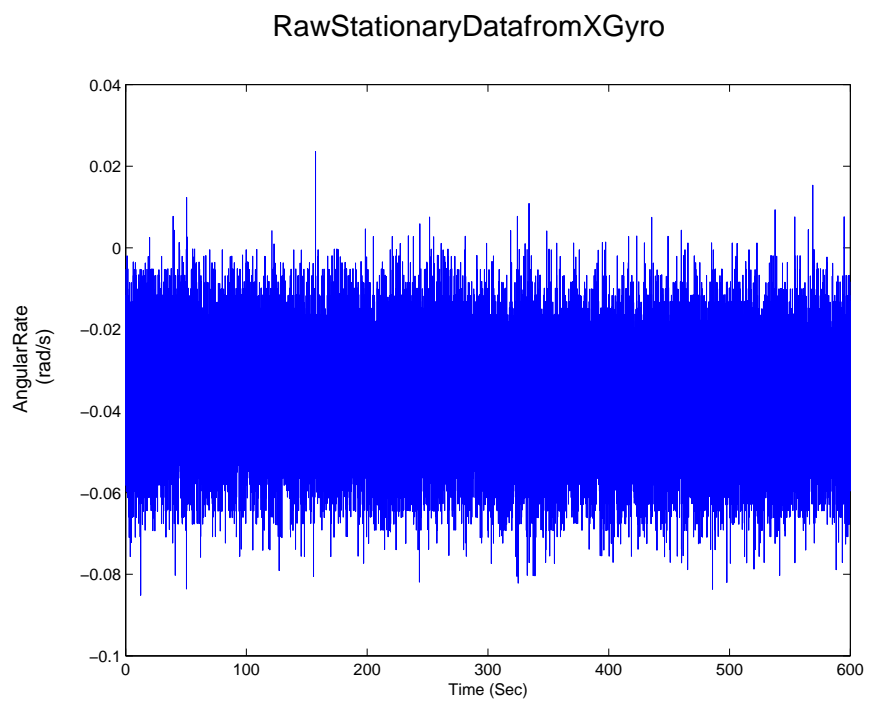


Figure 3.4 Raw Stationary Data from X Gyro

The values for each entry are shown in Table 3.3. They were determined from previous work [20] with the MT-9 IMU and were validated through covariance analysis. This was accomplished by exposing the system to various types of accelerations and angular rates on a dedicated flight in the test aircraft. Raw specific forces and angular rates were recorded from the IMU while position, velocity, and attitude information were recorded using the GAINR system. The IMU data was post-processed, and the TSPI data was used to conduct the covariance analysis as described in Section 2.4.6. Figures 3.5, 3.6, and 3.7, depict actual error vs. filter-predicted $\pm 1 \sigma$ for position, velocity, and attitude, respectively, and show that the actual error and the filter-predicted error match relatively well (i.e., actual error falls within $\pm 1 \sigma$ bounds roughly 68% of the time), indicating good filter performance. With validated dynamics noise strengths in hand, testing of the real-time algorithm could be accomplished.

3.3.3 Measurement Model. In addition to position, the Garmin GPS 35 provides north, east, and down velocity. Both position and velocity are incorporated using the standard discrete time measurement model of the form

$$\mathbf{z} = \mathbf{H}\mathbf{x} + \mathbf{v} \quad (3.24)$$

where \mathbf{z} is the measurement vector, \mathbf{x} is the state vector, \mathbf{H} is a measurement matrix relating the state variables and the measurement variables, and \mathbf{v} is the measurement noise vector. Using latitude as an example,

$$lat_{GPS} = lat_{True} + v$$

$$lat_{INS} = lat_{True} - \delta lat$$

Table 3.3 Dynamics Noise Standard Deviations

	Filter State	Value	Units
Q_1	δlat	$(9.873 \times 10^{-17})^2$	$(rad)^2/s$
Q_2	δlon	$(9.873 \times 10^{-17})^2$	$(rad)^2/s$
Q_3	δalt	$(6)^2$	$(m)^2/s$
Q_4	δv_N	$(1 \times 10^{-6})^2$	$(m/s)^2/s$
Q_5	δv_E	$(1 \times 10^{-6})^2$	$(m/s)^2/s$
Q_6	δv_D	$(1 \times 10^{-6})^2$	$(m/s)^2/s$
Q_7	$\delta \phi$	$(3.491 \times 10^{-11})^2$	$(rad/s)^2/s$
Q_8	$\delta \theta$	$(3.491 \times 10^{-11})^2$	$(rad/s)^2/s$
Q_9	$\delta \psi$	$(3.491 \times 10^{-11})^2$	$(rad/s)^2/s$
Q_{10}	δf_{x_s}	$(8 \times 10^{-4})^2$	$(m/s^2)^2/s$
Q_{11}	δf_{y_s}	$(8 \times 10^{-4})^2$	$(m/s^2)^2/s$
Q_{12}	δf_{z_s}	$(8 \times 10^{-4})^2$	$(m/s^2)^2/s$
Q_{13}	$\delta \omega_{x_s}$	$(1.745 \times 10^{-4})^2$	$(rad/s)^2/s$
Q_{14}	$\delta \omega_{y_s}$	$(1.745 \times 10^{-4})^2$	$(rad/s)^2/s$
Q_{15}	$\delta \omega_{z_s}$	$(1.745 \times 10^{-4})^2$	$(rad/s)^2/s$

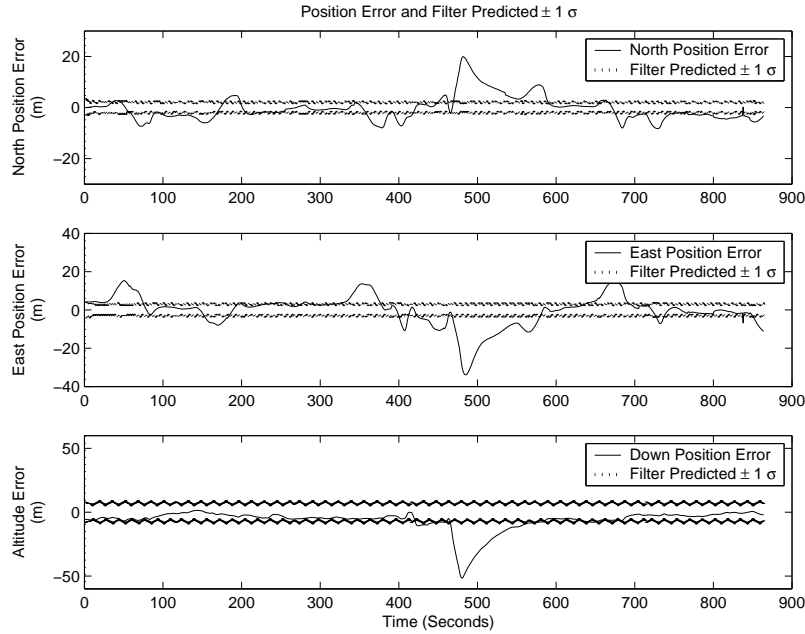


Figure 3.5 Position Error and filter-predicted $\pm 1 \sigma$

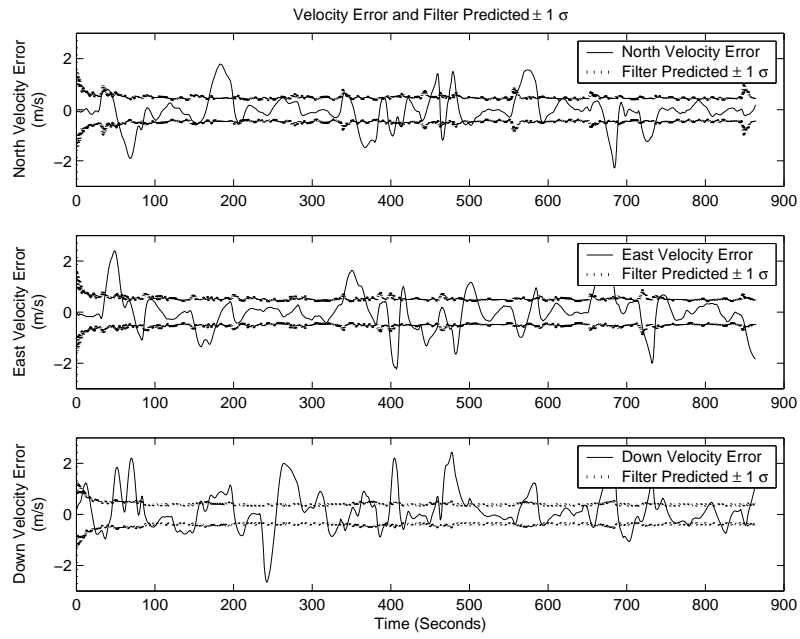


Figure 3.6 Velocity Error and filter-predicted $\pm 1 \sigma$

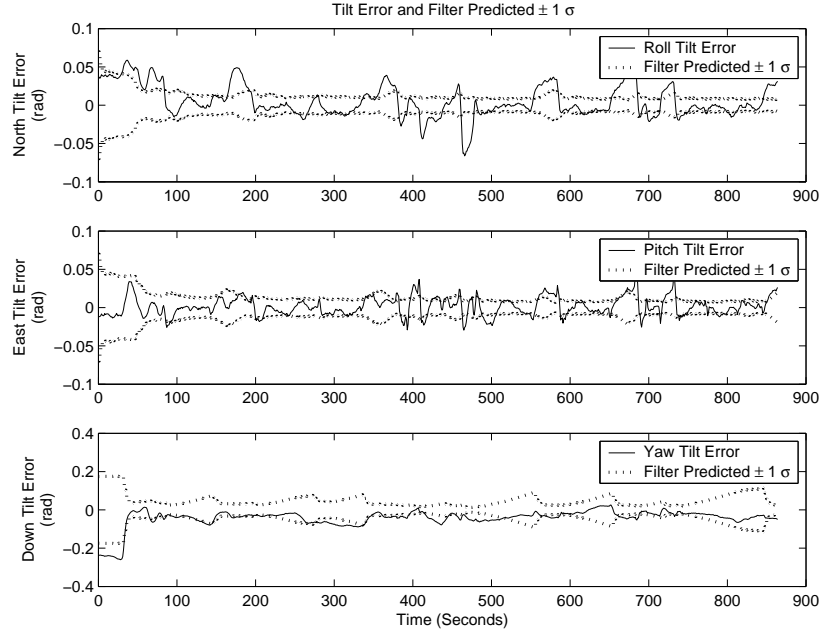


Figure 3.7 Attitude Error and filter-predicted $\pm 1 \sigma$

Subtracting the two yields

$$lat_{GPS} - lat_{INS} = \delta lat + v$$

The measurement is then

$$z_{lat} = lat_{GPS} - lat_{INS} = \delta lat + v \quad (3.25)$$

A similar process is accomplished for the other two position measurements (longitude and altitude) and the three velocity measurements. The final 6×1 measurement vector \mathbf{z} is then

$$\mathbf{z} = \begin{bmatrix} z_{lat} \\ z_{lon} \\ z_{alt} \\ z_{v_n} \\ z_{v_e} \\ z_{v_d} \end{bmatrix} \quad (3.26)$$

and the 6×15 measurement matrix \mathbf{H} is simply

$$\mathbf{H} = \begin{bmatrix} 1 & 0 & 0 & 0 & 0 & 0 & 0 & 0 \\ 0 & 1 & 0 & 0 & 0 & 0 & 0 & 0 \\ 0 & 0 & 1 & 0 & 0 & 0 & 0 & \dots \\ 0 & 0 & 0 & 1 & 0 & 0 & 0 & 0 \\ 0 & 0 & 0 & 0 & 1 & 0 & 0 & 0 \\ 0 & 0 & 0 & 0 & 0 & 1 & 0 & 0 \end{bmatrix}$$

3.3.4 Measurement Noise. The covariance \mathbf{R} of the measurement noise was determined by differencing the measurement data from the Garmin GPS 35 and the more accurate TSPI truth data. Standard deviations were taken from each sample and used to compute the \mathbf{R} matrix. An example of this can be seen in Figure 3.8,

which shows downward velocity measurement error from the Garmin GPS 35 data and $\pm 1 \sigma$ bars as computed by this procedure. Table 3.4 shows the measurement noise standard deviations used in the covariance analysis previously mentioned as well as the real time algorithm.

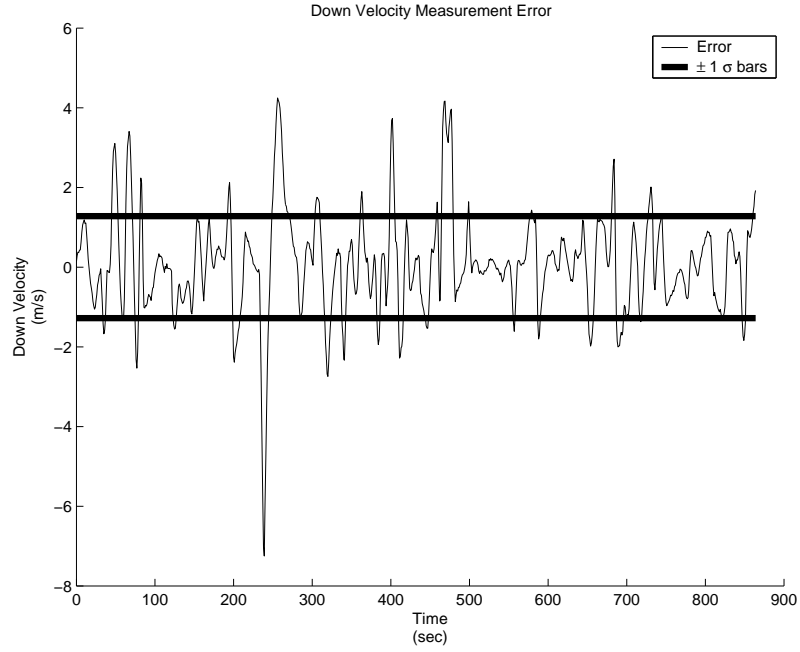


Figure 3.8 Down Velocity Measurement Error and $\pm 1 \sigma$

Table 3.4 Measurement Noise Standard Deviations

Measurement	σ	Units
Latitude	6.087×10^{-7}	<i>rad</i>
Longitude	9.996×10^{-7}	<i>rad</i>
Altitude	7.971	<i>m</i>
v_N	1.256	<i>m/sec</i>
v_E	1.288	<i>m/sec</i>
v_D	1.280	<i>m/sec</i>

3.3.5 Initial Conditions. All errors states are assumed to be zero-mean after initial alignment of the INS and $\hat{\mathbf{x}}_o = \mathbf{0}_{15 \times 1}$. Initial covariance \mathbf{P}_o is different for the stationary alignment and the in-motion alignment. For the stationary alignment, velocity is well known (i.e., zero) and is assigned a very low initial error covariance. Position is based on a conservative estimate of the measurement noise since the initial position is taken from a GPS solution. For the in-motion alignment, velocity is obviously less well known, but position is assigned a higher covariance as well. This is to accommodate the real-time algorithm. During the alignment process, the initial position is set, and several IMU records are processed to synchronize INS time to GPS time. During this period, a moving vehicle may have travelled several meters, and therefore the initial covariance on position is much higher. Table 3.5 summarizes the standard deviations values used for each alignment type.

Table 3.5 Filter Initial Standard Deviations

State	Stationary Alignment Value	In-Motion Alignment Value	Units
δlat	1.571×10^{-6}	7.853×10^{-4}	<i>rad</i>
δlon	1.571×10^{-6}	7.853×10^{-4}	<i>rad</i>
δalt	10	100	<i>m</i>
δv_N	1×10^{-10}	10	<i>m/sec</i>
δv_E	1×10^{-10}	10	<i>m/sec</i>
δv_D	1×10^{-10}	10	<i>m/sec</i>
$\delta \phi$	6.981×10^{-3}	6.981×10^{-2}	<i>rad</i>
$\delta \theta$	6.981×10^{-3}	6.981×10^{-2}	<i>rad</i>
$\delta \psi$	6.981×10^{-2}	0.175	<i>rad</i>
δf_{x_s}	0.5	0.5	<i>m/sec²</i>
δf_{y_s}	0.5	0.5	<i>m/sec²</i>
δf_{z_s}	0.5	0.5	<i>m/sec²</i>
$\delta \omega_{x_s}$	1.745×10^{-3}	1.745×10^{-3}	<i>rad/sec</i>
$\delta \omega_{y_s}$	1.745×10^{-3}	1.745×10^{-3}	<i>rad/sec</i>
$\delta \omega_{z_s}$	1.745×10^{-3}	1.745×10^{-3}	<i>rad/sec</i>

3.3.6 Kalman Filter Cycle. The GPS measurements are valid at the beginning of each GPS week second. Because of latencies in the GPS 35 receiver, however, the actual measurement data is not available until approximately 400 milliseconds

after the data is valid. Two Kalman filter propagation cycles per measurement update period are used to accommodate the delay. At the time the measurement is valid, INS position and velocity are stored. When the GPS measurement is available, a measurement update is accomplished using the stored INS position and velocity. The error states are then propagated to the current INS time (typically 400 ms after the GPS measurement time), and a null measurement is then accomplished (i.e., set $\hat{\mathbf{x}}(t_i^+) = \hat{\mathbf{x}}(t_i^-)$ and $\mathbf{P}(t_i^+) = \mathbf{P}(t_i^-)$). Estimates of the errors in the INS are then available for feedback corrections. After feedback corrections are made, the error states are propagated forward to the next GPS week second to facilitate the next measurement update.

3.3.7 Feedback Corrections. Estimates of the true position, velocity, and attitude as well as accelerometer bias and gyro drift are formed using the output of the INS navigation algorithm and the estimates of the errors in these quantities from the Kalman Filter. In order to minimize drift in the INS, the estimates of the true position, velocity, and attitude are used to “reset” the INS every time there is a measurement available.

Estimates of position and velocity can be formed by adding the INS quantity with the respective error state. For example, the estimate of velocity in the east direction \hat{v}_E is formed in the following manner.

$$\hat{v}_E = INS_{v_E} + \hat{\delta v}_E \quad (3.27)$$

Attitude estimates are formed using the skew symmetric matrix Ψ [31].

$$\Psi = \begin{bmatrix} 0 & -\delta\psi & \delta\theta \\ \delta\psi & 0 & -\delta\phi \\ -\delta\theta & \delta\phi & 0 \end{bmatrix} \quad (3.28)$$

$$\hat{\mathbf{C}}_b^n = [\mathbf{I} - \mathbf{\Psi}]\mathbf{C}_b^n \quad (3.29)$$

The performance of the system was observed to be better without resetting the accelerometer bias and gyro drift. Occasionally these states would become unstable in the feedback configuration. To keep the system stable, the algorithm utilizes a combination of feedforward and feedback implementations. x_{1-9} are feedback terms while x_{10-15} are feedforward terms.

3.4 Real-Time Software

MATLAB®'s serial port interface makes it possible to use MATLAB® in a real-time environment for this application. Serial port objects are established for the IMU, GPS receiver, and 3D audio hardware. Communications with each piece of equipment varies, depending on the communications protocol for each device, and event callback functions are the primary method to accomplish specific tasks. For example, each NMEA ASCII sentence from the GPS receiver terminates with a carriage return followed by a linefeed. To take advantage of this, each time this specific terminator is detected on the serial bus, a callback function is executed. This function reads all current data on the serial bus and checks for specific NMEA sentence headers. It then parses the desired data into a MATLAB® structure.

The One-Pulse-Per-Second (1PPS) output from the GPS receiver is integrated using the PinStatusFcn in MATLAB®. This callback function is typically used to detect the presence of connected devices or control the flow of data. A user-specified function will execute whenever there is a change in status of one of the RS-232 control pins. The pulse output from the GPS receiver is tied to the Carrier Detect (CA) pin, and the rising edge of the pulse is captured using logic in the PinStatusFcn. The start of GPS week second is determined when the CA pin transitions from low to high. The 1PPS accuracy of the Garmin GPS-35 is specified to be ± 1 microsecond [11].

The IMU outputs data in a continuous binary format with no terminators, so a subroutine checks for the number of bytes available on the serial bus. Each data packet sent from the IMU consists of 24 bytes. If 24 or more bytes are available on the serial bus, the subroutine searches for the message header, checks for data validity, and stores the data in a temporary software buffer until it can be read into the INS mechanization algorithm. In addition, this subroutine time tags the IMU data arrival time with GPS week seconds, using a combination of the NMEA data, the 1PPS, and the IMU sample counter. The sample counter is included in the IMU data packet and is incremented every sample period. It is a 16-bit counter and rolls over upon reaching 2^{16} sample period counts.

3.5 Chapter Summary

This chapter has described the navigation computations used to form an INS solution of position, velocity, and attitude. In addition, it detailed the design and motivation of the system Kalman filter, to include methods of correcting the INS. Lastly, the real-time software was briefly discussed.

IV. Test Results and Analysis

4.1 Overview

This chapter presents flight test results and analysis of the head tracker system developed in this research. First, background information is provided, to include overall system configuration, data collection, test methodology, and data set descriptions. The flight test results section contains performance results and analysis of the real-time system during a single flight under various conditions. Next, improvements to 3D audio localization through the addition of the head tracker system is examined. Finally, raw data collected during the flight is post-processed to provide further analysis of the head tracker algorithm. This final section includes the effects of GPS outages, the incorporation of GPS course information, and the use of a simplified dynamics model.

4.2 Flight Test Background Information

4.2.1 System Configuration. Operation of the real time system was first verified in a laboratory setting. The MT9 IMU, Garmin GPS 35, processing laptop, and 3D audio equipment were set up to ensure proper connectivity and functionality. A diagram of the overall system is depicted in Figure 4.1. After laboratory testing, the system was placed inside an automobile for a dynamic evaluation. A truth source was not available for this dynamic ground test, and a formal analysis could not be accomplished. Qualitatively, the head tracker worked well inside the moving automobile, and the system was prepared for flight test.

The test aircraft, C-12C tail number 73-1215, was modified to allow testing of the system under various flight conditions. The GAINR system was added to the existing Data Acquisition System (DAS) rack [30] onboard the aircraft. The head tracker laptop, 3D audio laptop, pan-and-tilt unit, and MT9 IMU were mounted to

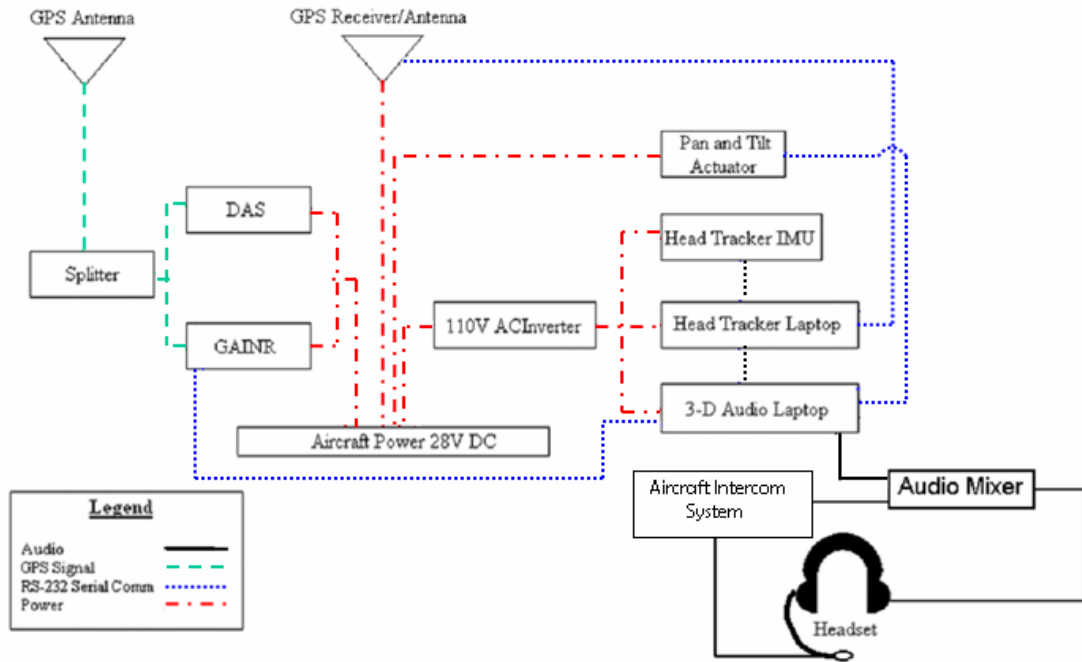


Figure 4.1 System Diagram

a plate on top of the DAS rack, as seen in Figures 4.2 and 4.3. The pan-and-tilt was intended to simulate head movement in a measurable way (e.g., rotate the MT9 a known number of degrees). Unfortunately, the actuator proved to be incompatible with aircraft power, so it could not be used in this evaluation. Precise location of all equipment was determined through the use of Faro laser surveying equipment. This information was passed to the TPSI office so that moment-arm corrections could be applied to the truth data. A moment-arm correction was not applied for the head tracker, since the Garmin GPS 35 antenna was within 1 meter of the IMU (well within the GPS position measurement accuracy). Exact equipment location can be found in Appendix A.

4.2.2 Data Collection. The real-time head tracker algorithm recorded data to four different files. The first file is a record of the alignment parameters that were



Figure 4.2 Hardware Mounted in C-12C

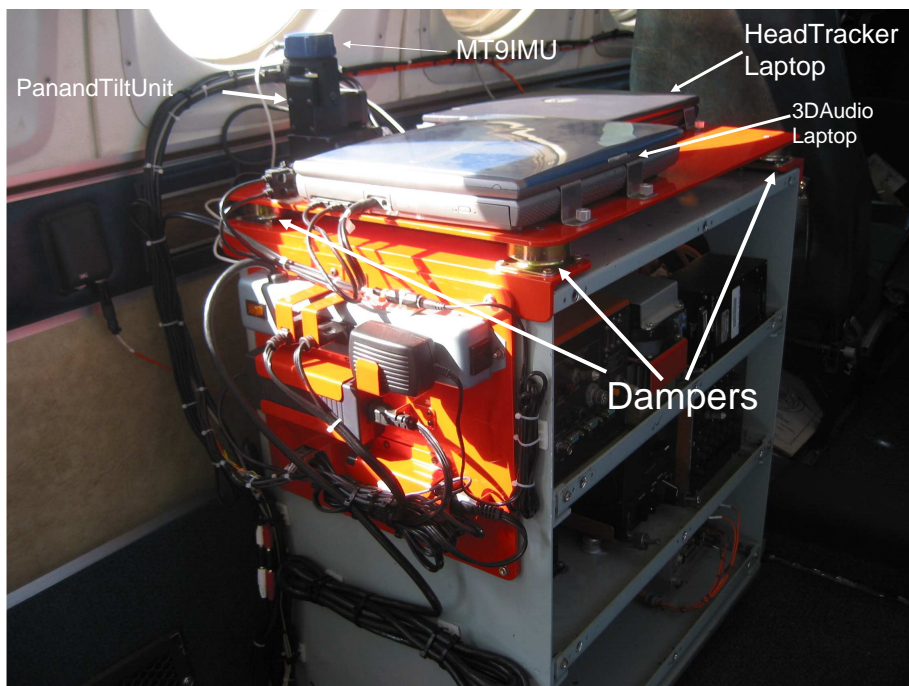


Figure 4.3 Top of Data Acquisition System Rack

used for INS initial conditions, to include initial position, velocity, attitude, and gyro drift. The next file contains position and velocity data from the Garmin GPS 35 at a 1-Hz rate. The third file is a binary file that contains the raw accelerations and angular rates from the MT9 IMU as well as head-tracker roll, pitch, and heading. This data was collected at 100-Hz. Finally, the last data file contains both INS and filter-estimated navigational data (i.e., position, velocity, and attitude), all Kalman filter states before and after measurement updates, and all filter-predicted covariance values before and after measurement updates. This data was collected at the Kalman filter update rate of 1-Hz. The first 3 data files are primarily used as an input for the post-processing version of the system. The last file is used to evaluate the performance of the real-time system. It should be mentioned that a 0.05 second delay was observed in the Garmin GPS 35 data when compared to the TSPI truth data. Since the head-tracker system time is based on the Garmin GPS 35 time, all head-tracker filter/INS time tagging includes the delay. This 0.05 second delay does not affect actual system performance (because timing was consistent between all the head tracker components), but the head-tracker operates on a slightly different system time than desired. In order to compare filter results with truth data, the TSPI data was shifted by the amount of the delay.

4.2.3 Overall Test Methodology. One of the test objectives was to determine inertial head tracker accuracy with the inertial measurement unit fixed to the aircraft body frame. As mentioned in Chapter 3, one flight was dedicated to collecting position, velocity, and attitude data from both the inertial head tracker and the GAINR system. This data was used to refine the parameters that make up the dynamics model and measurement model of the head tracker Kalman filter. The head tracker was then evaluated using the updated Kalman filter parameters.

The head tracker evaluation was accomplished by collecting head-tracker data as well as TSPI GAINR-system data during a second dedicated flight. The maneuver set listed in Table 4.1 was accomplished during the flight and was designed to expose

the system to a wide variety of accelerations and angular rates so that performance could be evaluated under these different conditions. Aircraft configuration for all test points was gear up and flaps up. The propeller speed was 1700 rpm, except for the climb in which it was set to 1900 rpm. The maneuvers were flown between 120 KIAS to 230 KIAS and 8,000 feet to 20,000 feet pressure altitude.

Table 4.1 C-12C Aircraft Maneuver Set for Inertial Head Tracker Evaluation

Maneuver	Nominal Conditions	Remarks
Climbs	150 KIAS	Δ Alt of at least 2000 ft
Straight and Level Unaccelerated Flight (SLUF)	170 KIAS, 12,000 ft	TOL: ± 4 kts, ± 100 ft
Constant G Turns	170 KIAS, 12,000 ft	Data band 20°- 60° of bank TOL: $\pm 5^\circ$ AOB, ± 200 ft, ± 4 kts
Steady Heading Side Slips	170 KIAS, 12,000 ft	TOL: ± 5 kts
Level Accelerations	12,000 ft	TOL: ± 100 ft
Level Decelerations	12,000 ft	TOL: ± 100 ft
Roller Coasters	170 KIAS	Load factors to 80% of the Flight Manual G limits
Yoke Raps	170 KIAS, 12,000 ft	
Pitch/Rudder Doublets	170 KIAS, 12,000 ft	No Yaw frequency sweeps
30° to 30° Bank-to-Bank Rolls	170 KIAS, 12,000 ft	TOL: ± 1000 ft
Descents	150 KIAS	Δ Alt of at least 2000 ft

4.2.4 Data Sets. The data collected during the evaluation flight are broken into 5 data sets. The entire set includes more than 2 hours of data and encompasses initial ground alignment prior to takeoff to clearing the runway after landing. Table 4.2 summarizes the details of each data set.

4.3 Flight Test Results

Overall, the best performance of the real-time system is found in data set 2. This is based on the evaluation criteria agreed upon by AFRL/HE. System performance was considered satisfactory if the angular accuracy (defined as error in roll, pitch, and heading) for 90% of the samples was within ± 3 degrees, and marginal

if the angular accuracy for 90% of the samples was within ± 7 degrees. Otherwise, the performance was deemed unsatisfactory.

Table 4.2 Data Set Summary

Data Set	Length Mins + Secs	Contents
1	24+59	Ground alignment, taxi, takeoff, climb
2	26+21	Straight and Level Unaccelerated Flight (SLUF), constant G turns, steady heading side slips
3	22+46	Level accel, level decel roller coaster, yoke raps, pitch/rudder doublets, bank-to-bank rolls
4	25+12	Multiple level turns during 3D Audio equip evaluation
5	27+04	Descent, landing, taxi clear of runway

Data set 2 results from real-time processing are depicted in several figures below. The overall ground track with respect to the Edwards AFB special-use air space is depicted in Figure 4.4. TSPI position, velocity, and attitude can be seen in Figures 4.5 through 4.8.

The trajectory starts with the aircraft on a easterly heading and then a right hand turn to west. The aircraft remains on the westerly heading for approximately 5 minutes before accomplishing a 180 degree right-hand turn back to the east immediately followed by a left hand turn to the north. The aircraft then flies through a series of full-circle constant-G turns. The first constant-G turn is a 30° angle of bank turn to the left. The second constant-G turn is a 45° angle of bank turn to the right, and finally, the last constant G-turn is a 60° angle of bank turn to the right. The aircraft then turns right to a south-easterly heading. On this heading, a steady

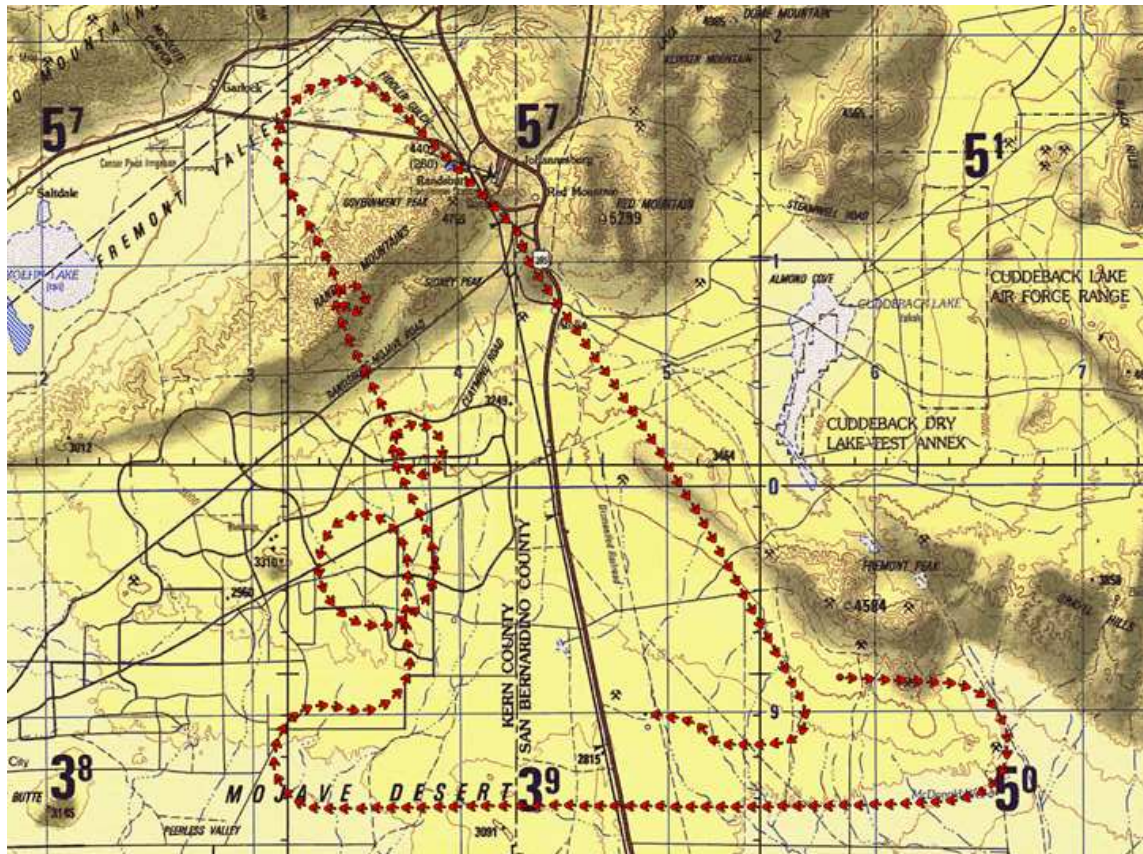


Figure 4.4 Data Set 2 Ground Track

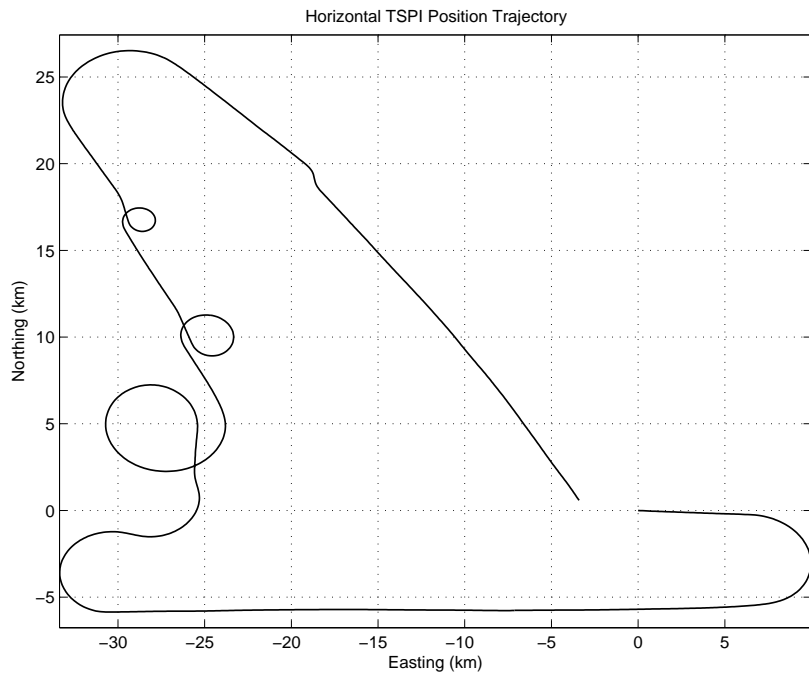


Figure 4.5 Data Set 2 Horizontal TSPI Position Trajectory

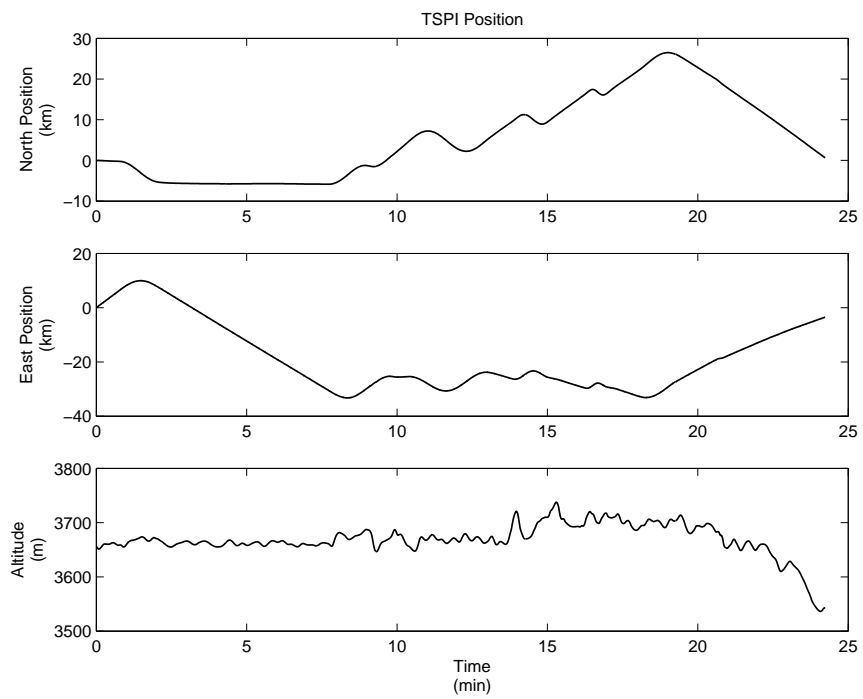


Figure 4.6 Data Set 2 TSPI Position

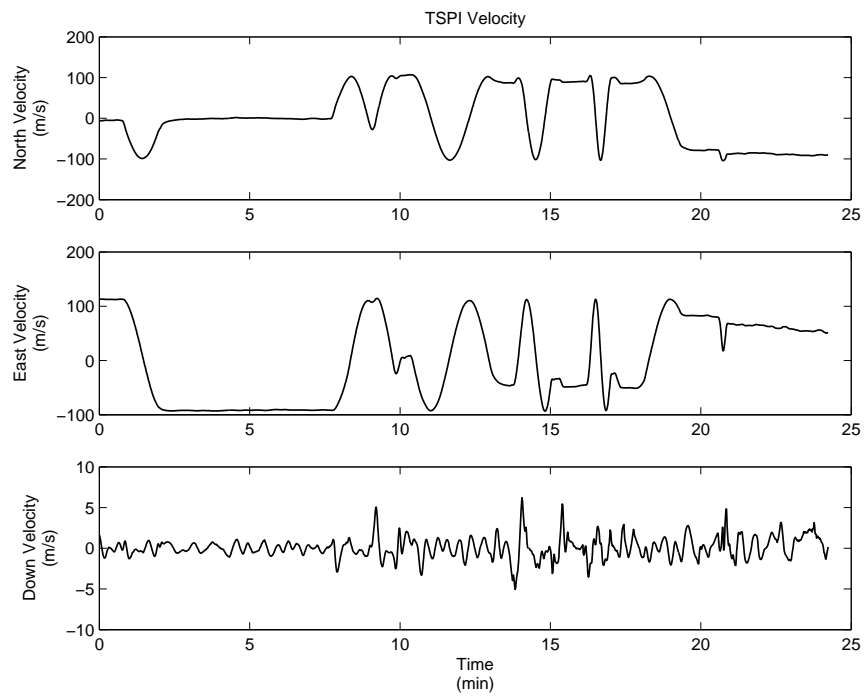


Figure 4.7 Data Set 2 TSPI Velocity

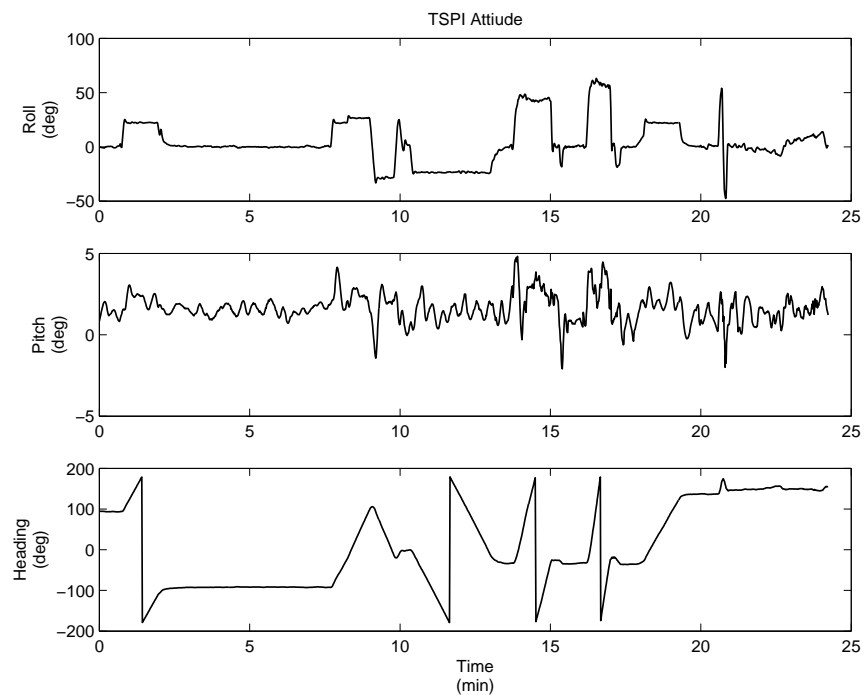


Figure 4.8 Data Set 2 TSPI Attitude

heading side slip is accomplished (to be discussed in a later section) followed by more straight-and-level flight to the south-east. This entire segment of flight occurs at approximately 12,000 ft MSL (3658 m).

Figures 4.9 and 4.10 depict accelerometer bias estimates and gyro drift estimates respectively. The filter-estimated x axis accelerometer bias has a mean value of approximately 0.35 m/s^2 with some fluctuations ($1\sigma = 0.093 \text{ m/s}^2$), and the y axis accelerometer bias has a mean value of 0.7 m/s^2 with smaller fluctuations ($1\sigma = 0.045 \text{ m/s}^2$) The filter learns the z axis accelerometer bias very quickly, since the gravity vector essentially coincides with the z axis most of the time. The mean value for the z axis accelerometer bias is 0.056 m/s^2 with a 1σ value of only 0.021 m/s^2 .

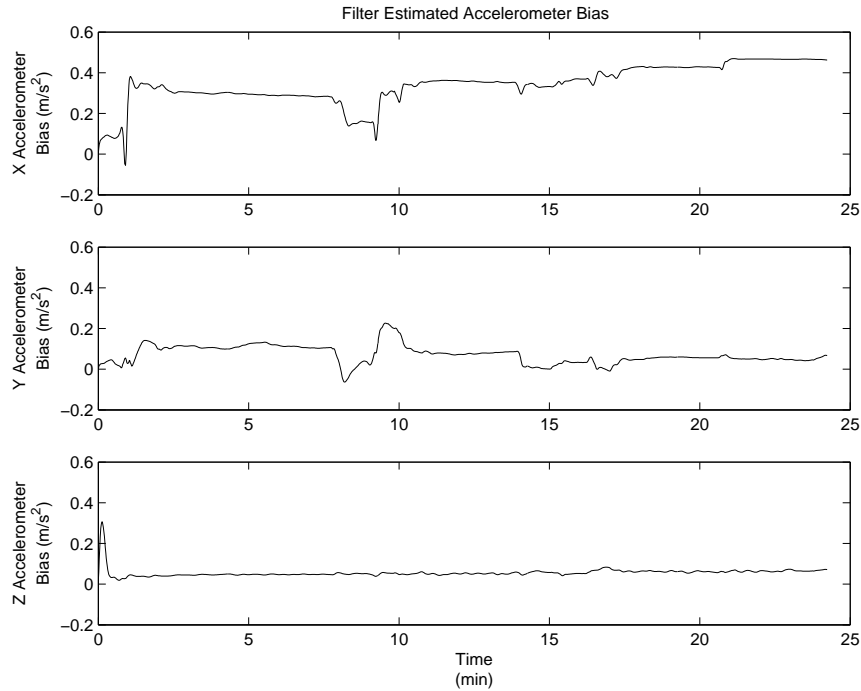


Figure 4.9 Data Set 2 Filter Estimated Accelerometer Bias

The x and z axis gyro drift estimates stay fairly constant throughout the data set with mean values of -0.10 deg/s and -0.12 deg/s , respectively. The x and z axis gyro drift estimates have similar 1σ values of approximately 0.05 deg/s . The y axis

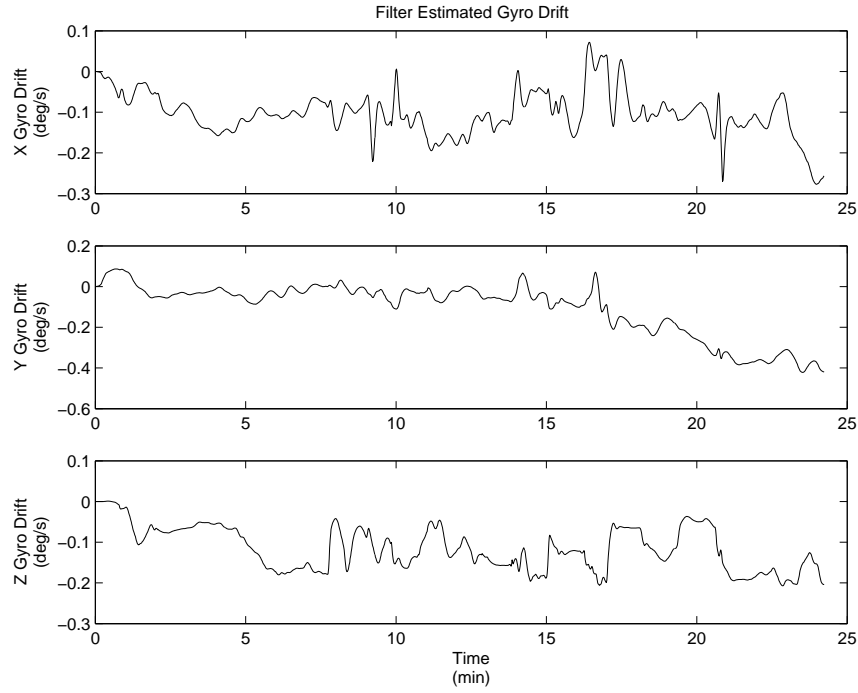


Figure 4.10 Data Set 2 Filter Estimated Gyro Drift

gyro drift estimate has a mean value of -0.11 deg/s and a 1σ value of 0.13. The estimate starts at zero and gradually grows in magnitude until reaching -0.42 deg/s.

Measurement residuals are shown in Figures 4.11 and 4.12. These figures show that the position and velocity measurements are not white. This is an expected outcome, since a loosely-coupled INS/GPS integration is being used. In addition, this may indicate that further tuning of the Kalman filter is possible.

Actual filter error and filter-computed standard deviations for position, velocity, and attitude error are depicted in Figures 4.13 through 4.15. These figures show that the system estimates position and velocity well. This is not surprising, since the system relies on GPS position and velocity measurements. The system also estimates attitude relatively well. Roll accuracy was within ± 3 degrees for 100% of the samples, and pitch accuracy was within the ± 3 degree specification for 99% of the samples. The filter did not perform as well at estimating heading,

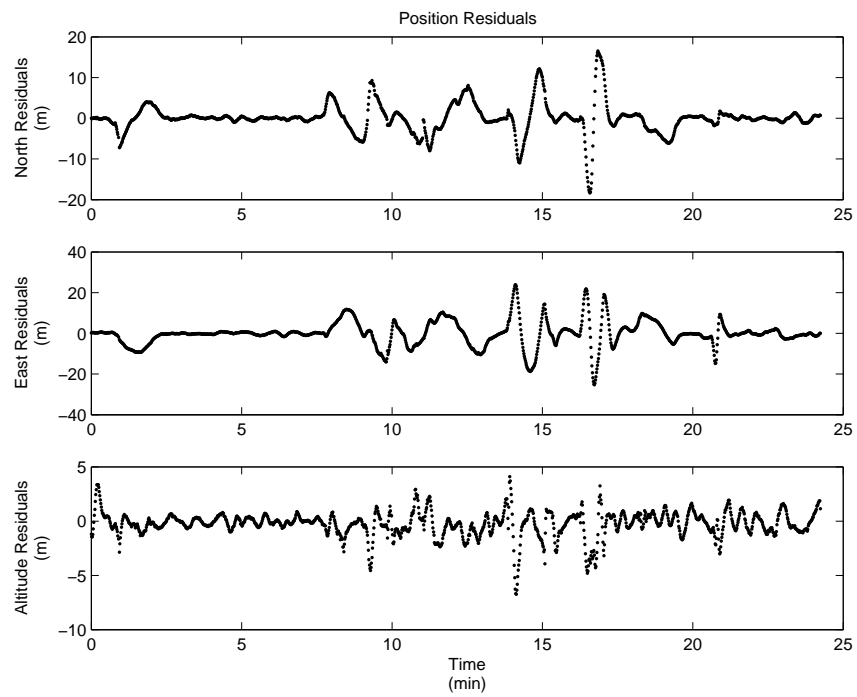


Figure 4.11 Data Set 2 Position Residuals

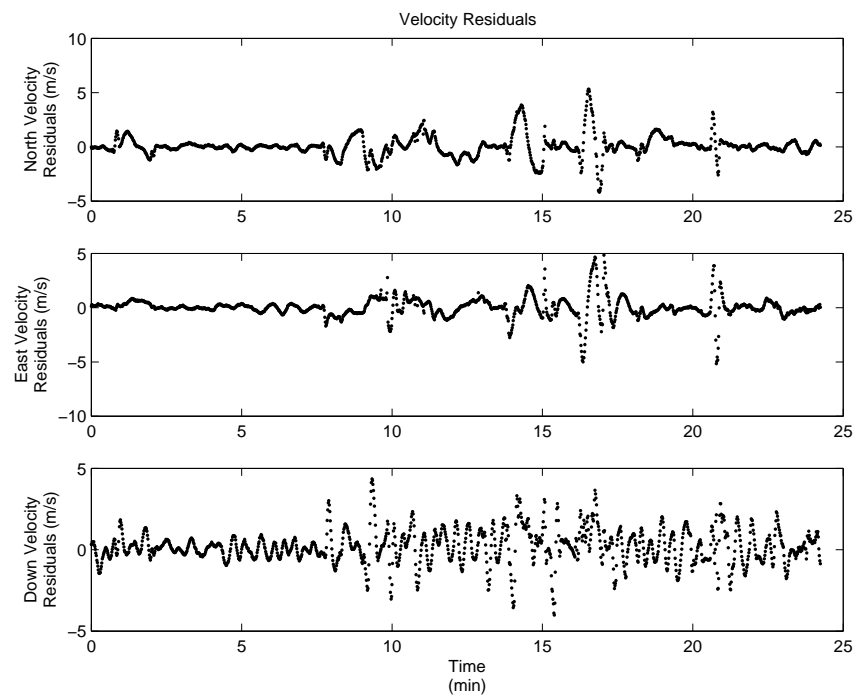


Figure 4.12 Data Set 2 Velocity Residuals

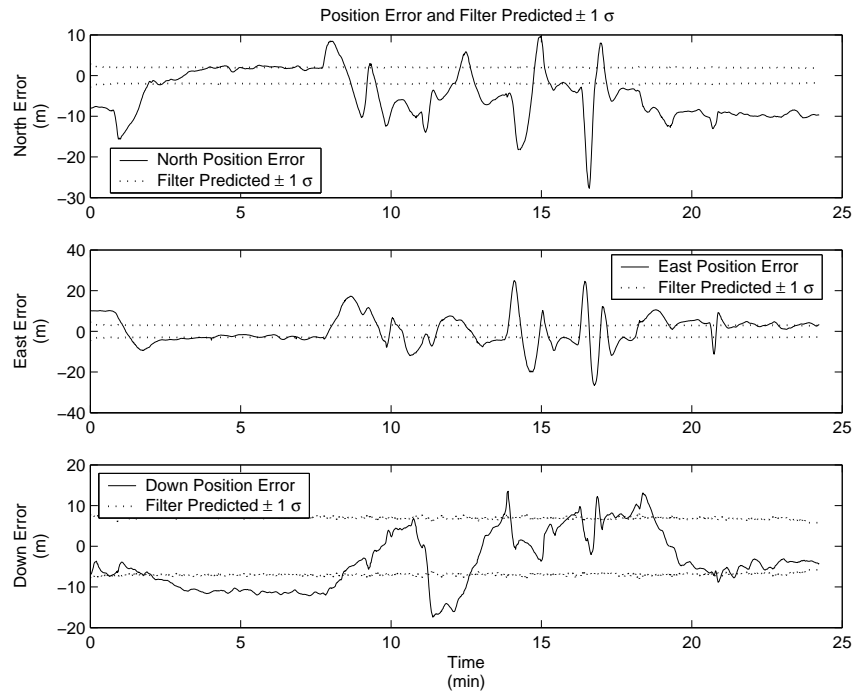


Figure 4.13 Data Set 2 Position Error and Filter Predicted $\pm 1\sigma$

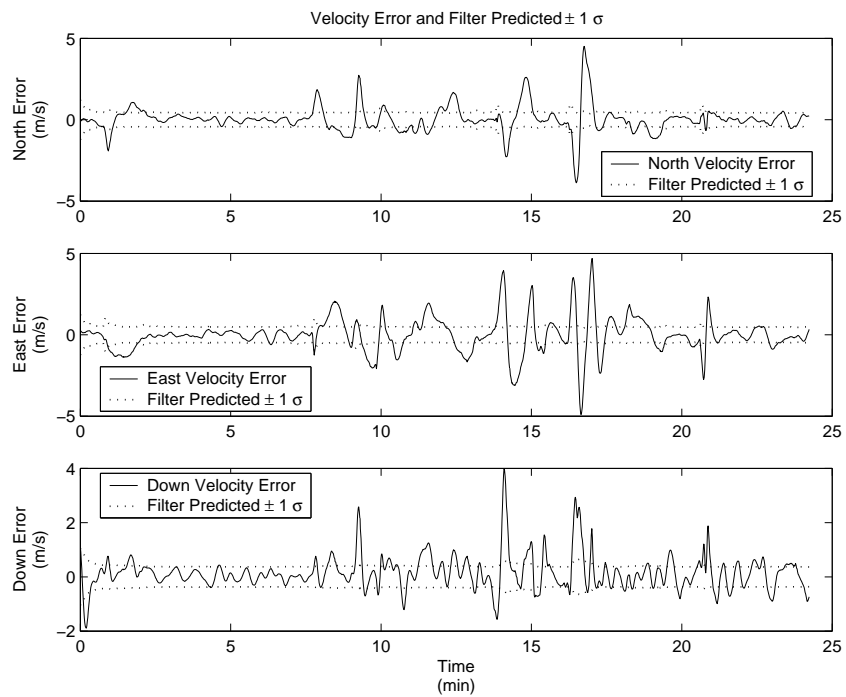


Figure 4.14 Data Set 2 Velocity Error and Filter Predicted $\pm 1\sigma$

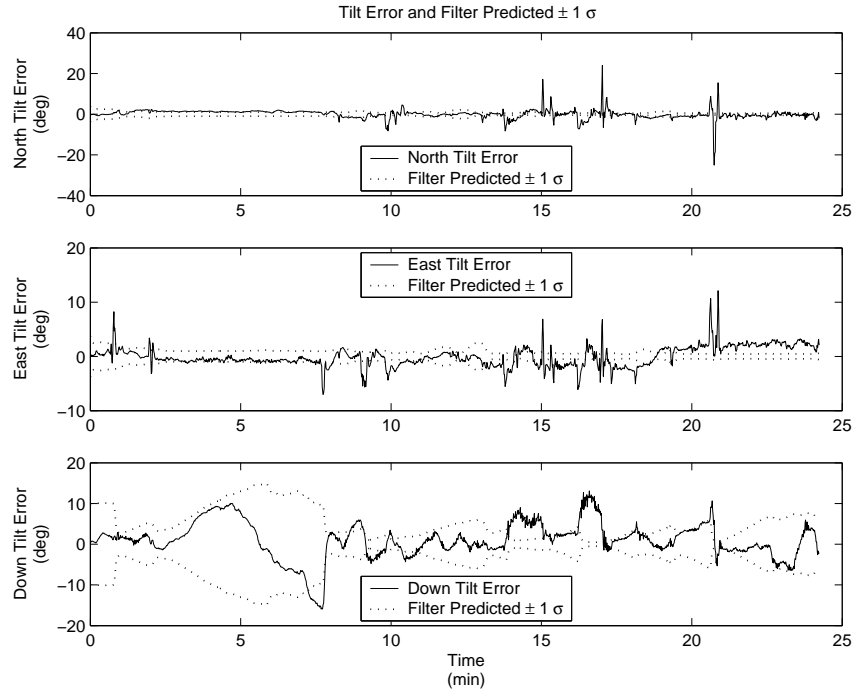


Figure 4.15 Data Set 2 Tilt Error and Filter Predicted $\pm 1\sigma$

with only 70% of the samples being within the ± 3 degree specification and 91% being within the ± 7 degree specification. Reasons for inferior heading performance will be addressed in the next section. Figure 4.16 shows filter-estimated and TSPI attitude. Despite the attitude accuracy just mentioned, the system outperforms expectations, and one can see that the filter tracks the motion of the aircraft very well for a MEMS-based system implemented in real-time using MATLAB[®] operating in a Windows[®] environment.

It is also apparent from the $\pm 1\sigma$ plots that additional filter tuning is warranted. The same measurement noise, process noise, and initial covariance values that were verified in the covariance analysis discussed in Chapter 3 were used in the real-time algorithm. This confirms the notion that complete filter tuning cannot be accomplished from one data set.

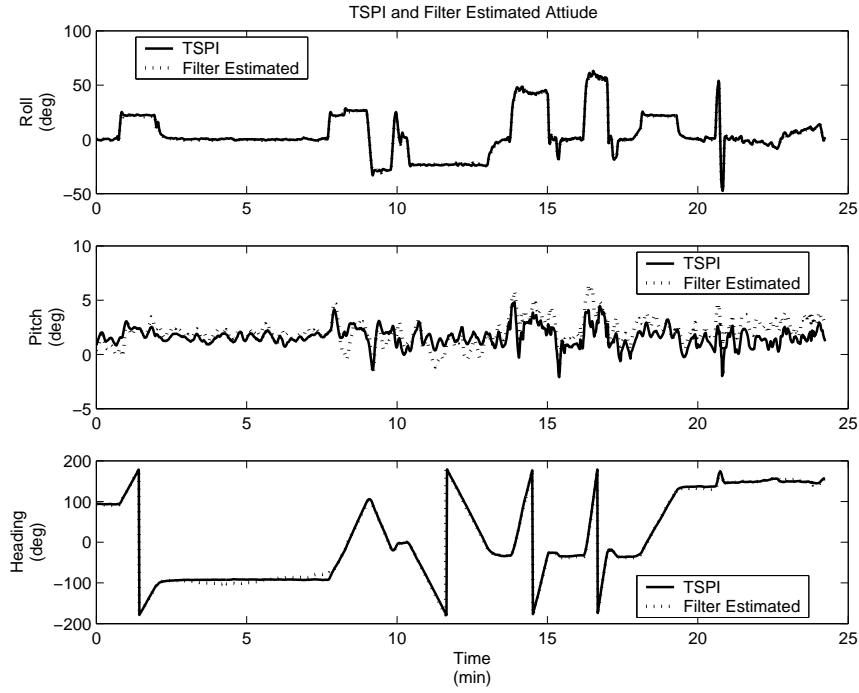


Figure 4.16 Data Set 2 TSPI and Filter Estimated Attitude

4.3.1 Straight-and-Level Unaccelerated Flight. One reason the filter did not perform as well at estimating heading is that some of data set 2 includes unaccelerated flight. Figure 4.17 and Figure 4.18 focus in on the Straight-and-Level Unaccelerated Flight (SLUF) section that occurs between 2.5 and 7.5 minutes of data set 2. The pitch and roll errors stay relatively small, but the heading error begins to grow almost immediately after the straight and level flight begins. As soon as a turn is made after the SLUF segment, the heading error decreases. This can be seen in Figure 4.18, in which the magnitude of the heading error decreases to less than 2 degrees. One can also see in Figure 4.15 that the filter predicted $\pm 1\sigma$ values for the SLUF segment between 2.5 minutes and 7.5 minutes also increase and then decrease in the presence of turns. Thus, the models incorporated in the filter allow it to properly reflect that it has this difficulty in SLUF. The filter cannot predict heading error as well as pitch and roll error, because the filter relies in part on specific force to determine attitude errors. This is apparent when examining how the

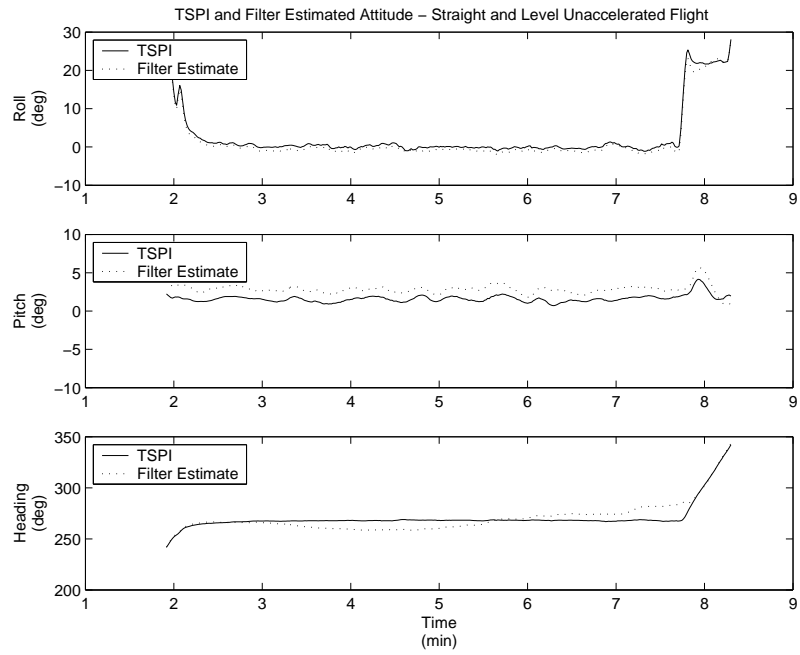


Figure 4.17 TSPI and Filter Estimated Attitude during SLUF - Data Set 2

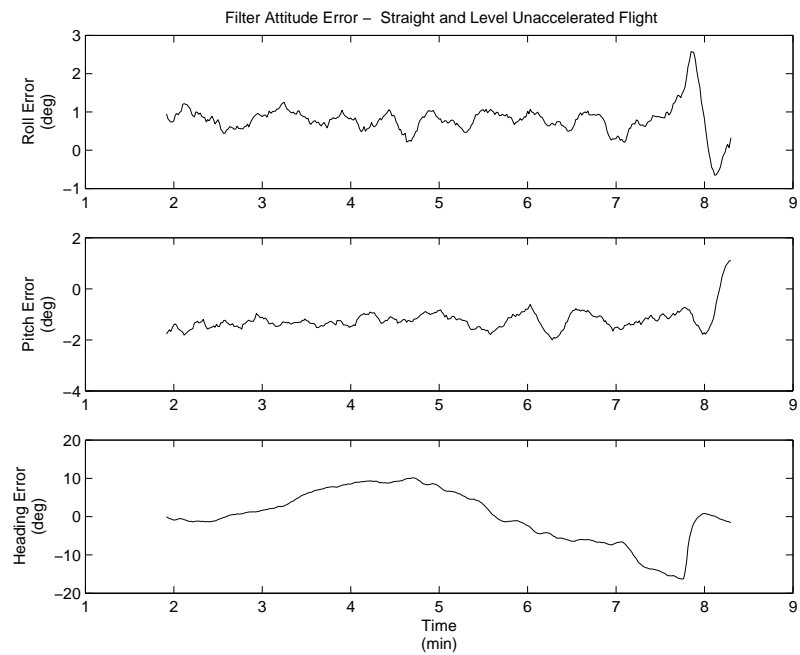


Figure 4.18 Filter Angular Accuracy in Straight-and-Level Unaccelerated Flight - Data Set 2

the velocity states are related to the attitude states in the dynamics model. Again, the \mathbf{VA} partition from the \mathbf{F} matrix discussed in Section 3.3.1 is

$$\mathbf{VA} = \begin{bmatrix} 0 & -f_D & f_E \\ f_D & 0 & -f_N \\ -f_E & f_N & 0 \end{bmatrix}$$

Local gravity always provides specific force in the down direction, so the north and east tilt errors are always strongly coupled to the velocity states. A tilt error in the north and/or east direction will result in a component of gravity being misapplied in the computed horizontal plane. Since velocity error is directly observable from GPS position and velocity measurements, any unexpected velocity error can be attributed to attitude error. In contrast, down tilt error is only strongly coupled to the velocity states through horizontal acceleration (i.e., f_E and f_N) as seen in the last column of the \mathbf{VA} partition. Therefore, heading error is only observable when the IMU is subjected to horizontal accelerations. This is somewhat of a simplification, since the attitude errors are related to other states as described in Equation (3.21), but it does explain why the filter has a more difficult time estimating heading error under straight-and-level unaccelerated flight. Figure 4.19, taken from data set 5, shows the filter again having problems during straight and level flight. Clearly, the filter heading estimates are better during turning flight and degraded during level, unaccelerated flight.

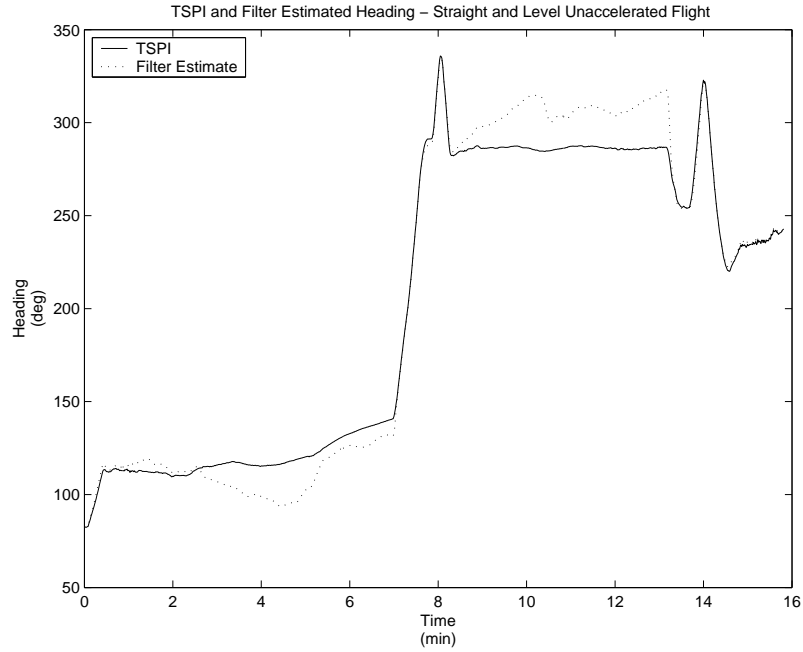


Figure 4.19 TSPI and Filter Estimated Heading - Data Set 5 (Straight-and-Level Unaccelerated Flight Occurred Between 1 and 5 Minutes and Between 9 and 13 Minutes)

4.3.2 Steady Heading Side Slip. The steady heading side slip is used to change the heading of the aircraft without exposing it to radial acceleration. The heading of the aircraft is changed a few degrees using the rudder, and a turn is prevented by applying a coordinated amount of aileron deflection. In this way, the side force generated by the rudder is balanced by a component of the lift vector in the opposite direction, and the aircraft is held on a constant “heading” (really a constant course). In lieu of the pan-and-tilt actuator, this was one method to simulate head rotation by a few degrees in the absence of acceleration. Examining the steady heading side slip shows that angular motion accompanied by essentially unaccelerated flight (e.g., a very typical case for the head tracking application) does not provide the filter with enough information to allow accurate estimate heading using the MEMS IMU. Figure 4.20 shows a steady heading side slip between the 78

second point and the 88 second point. Actual aircraft heading transitions from 156° to 148° during the maneuver. Although this is a small heading change, the filter does not track it well, and heading error increases to 6 degrees.

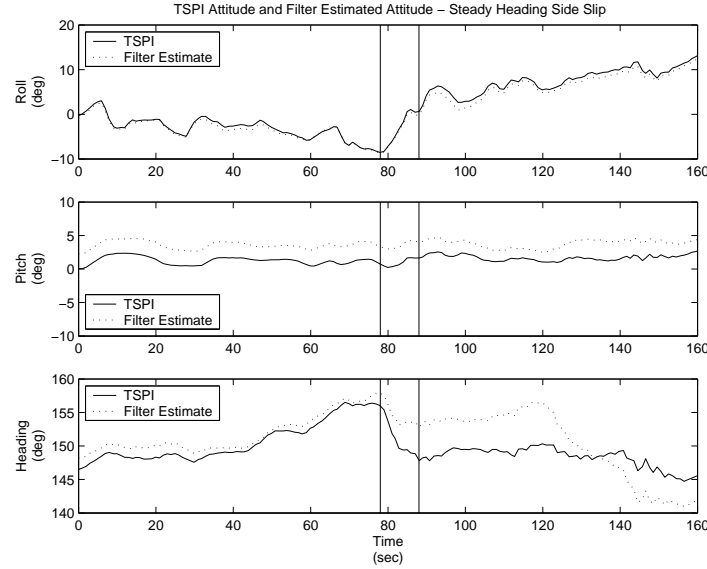


Figure 4.20 TSPI and Filter Estimated Attitude - Steady Heading Side Slip (From 78 Seconds to 88 Seconds)
- Data set 2

4.3.3 Ground Alignment Through Climbout. In previous sections, it has been shown that the head tracker has difficulty estimating heading during unaccelerated conditions. To form a comparison, the short period of relatively high linear acceleration ($\approx 3m/s^2$) during the takeoff roll is examined. Figure 4.21 depicts the ground track of the aircraft from parking to the end of the runway, takeoff roll, and the first turn on departure, all taken from data set 1. Prior to taxi, a ground alignment was performed. This alignment was accomplished using the MT9 magnetometers, and the initial heading was in error by 30 degrees. Initial roll and pitch error were both less than 1 degree. During the acceleration of takeoff, heading error does decrease, as shown in Figure 4.22. With a consistent horizontal specific force available, the filter is able to estimate heading error more correctly during this time.

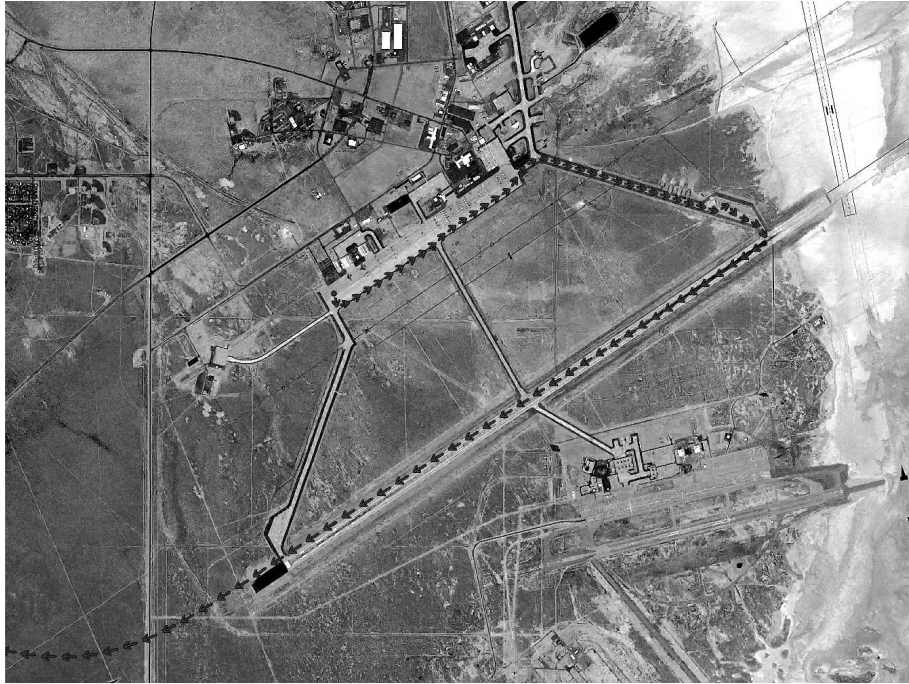


Figure 4.21 Ground Ops through Takeoff Ground Track - Data Set 1

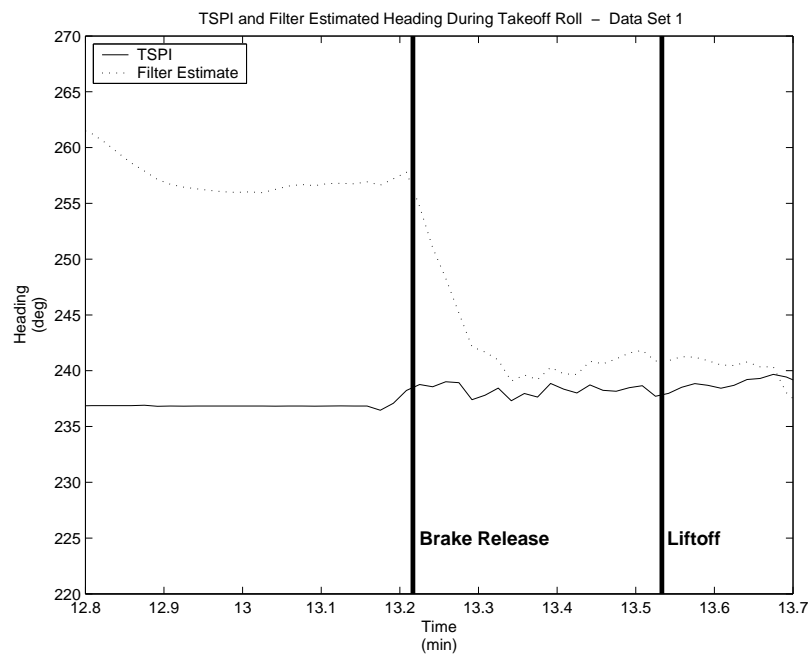


Figure 4.22 TSPI Heading and Filter Estimated Heading During Takeoff Roll - Data set 1

With such a poor initial alignment, it is reasonable to consider how the filter would have performed with a more accurate alignment. GAINR roll, pitch, and heading at the time of the alignment were used to form an initial DCM. Data set 1 was post-processed using the GAINR-based DCM as the initial alignment DCM. Attitude error for both alignment types is depicted in Figure 4.23. The filter using the initial GAINR alignment outperforms the filter using the magnetometer alignment as expected. Table 4.3 lists the number of samples that fell within the $\pm 3^\circ$ and $\pm 7^\circ$ specifications for both alignment types. It is possible that the GAINR alignment would have provided more benefits under different initial covariance values. If smaller initial covariance values are used for the tilt error states, the filter will be expecting the more accurate alignment, and it will “trust” the initial tilt errors for a longer period of time.

Even though the filter has reasonable attitude estimates during the takeoff roll with the magnetometer alignment, attitude estimates for the rest of data set 1 are not as accurate when compared to the overall results using the GAINR alignment. When the filter starts with a precise alignment, the filter has a better chance to form accurate estimates of accelerometer bias and gyro drift. The benefits of knowing these states more accurately from the beginning result in better performance throughout the data set. Figures 4.24 and 4.25 depict the accelerometer and gyro drift states after both alignment types. One can see that the filter appears to “learn” the accelerometer bias states more quickly when proceeded by a GAINR alignment. This is especially true for the x accelerometer bias. In the case of the gyro-drift

Table 4.3 Alignment Comparison Attitude Results

Alignment Type	Roll	Pitch	Heading
Magnetometer Alignment	96% within $\pm 3^\circ$	91% within $\pm 3^\circ$	27% within $\pm 3^\circ$
	100% within $\pm 7^\circ$	97% within $\pm 7^\circ$	51% within $\pm 7^\circ$
GAINR Alignment	100% within $\pm 3^\circ$	100% within $\pm 3^\circ$	53% within $\pm 3^\circ$
	100% within $\pm 7^\circ$	100% within $\pm 7^\circ$	83% within $\pm 7^\circ$

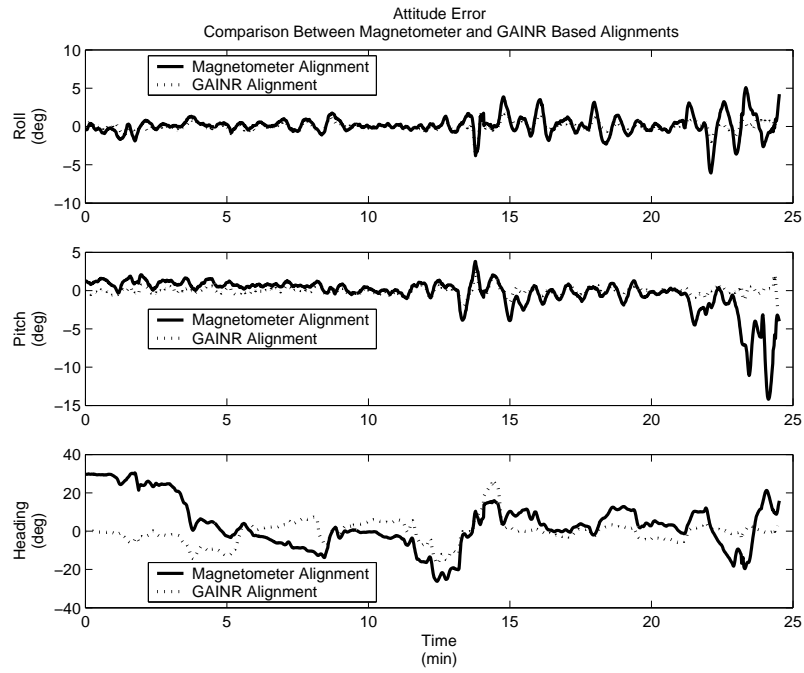


Figure 4.23 Attitude Error - Comparison Between Magnetometer-Based and GAINR-Based Alignments - Data Set 1

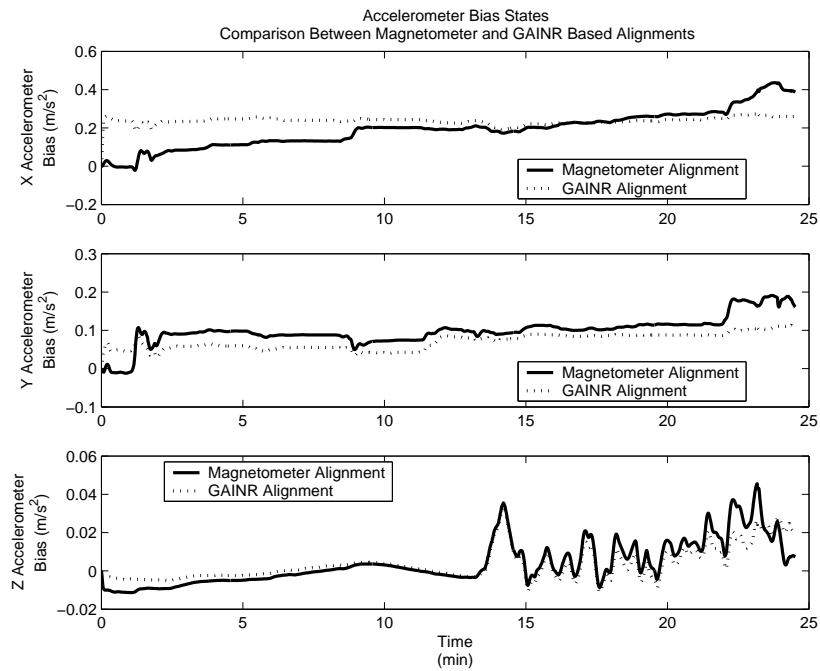


Figure 4.24 Accelerometer Bias States - Comparison Between Magnetometer-Based and GAINR-Based Alignments - Data Set 1

states, the mean values for the estimates are similar under either condition, but the estimates fluctuate less when proceeded by the GAINR alignment. It is clear that a better stationary alignment technique is required.

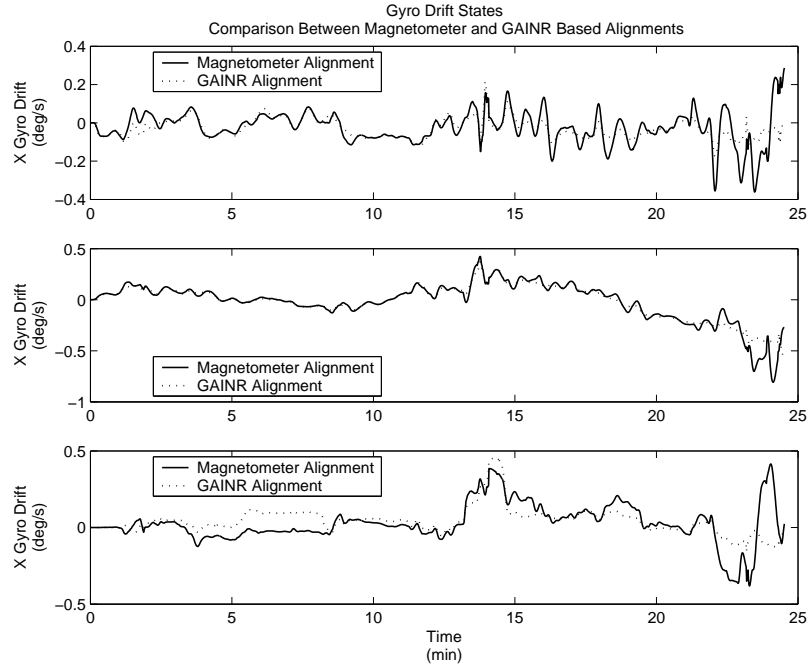


Figure 4.25 Gyro Drift States - Comparison Between Magnetometer-Based and GAINR-Based Alignments - Data Set 1

4.3.4 Deficiencies in Real-Time Data Capture of Sensor Outputs. As discussed in Section 3.4, data from the IMU and GPS receiver are transmitted to the processing laptop via an RS-232 serial bus. As each byte is received at the the laptop communications port, it is placed in a hardware buffer. Once in the hardware buffer, it should be available for use by MATLAB®. The computer's operating system has control over this process. Analysis shows that sometimes Microsoft Windows® is negligent in its duty to make data in the hardware buffer accessible to applications like MATLAB®. It is difficult to ascertain if data was actually sent from the sensor, but since data gaps from both the GPS receiver and the IMU frequently occur at the same time, these gaps are most likely attributed to Windows-induced delays, as

it is unlikely that both sensors are simultaneously reluctant to output data. In an attempt to keep the filter from diverging after data outages, the real-time algorithm resets all state covariances to their initial values if any IMU gaps greater than or equal to 40 milliseconds are detected. Gaps in data from the IMU are present in all data sets except data set 1, and the covariance-reset mechanization appears to handle gaps up to 120 milliseconds without any significant degradation in performance. The next largest gap, 2.2 seconds, is found in data set 5. A definite degradation in attitude performance is seen as a result of the 2.2-second IMU gap, which is also accompanied by a 5-second GPS outage. Figure 4.26 shows acceptable performance before the event (highlighted in the figure by the solid vertical line) followed by an immediate increase in roll, pitch, and heading error after the data gap. This increase is not surprising, since even a modest angular rate in the roll, pitch, or yaw axis can result in a very different DCM after 2.2 seconds. In addition, any noise in the data will be amplified greatly when integrated over the 2.2 second period.

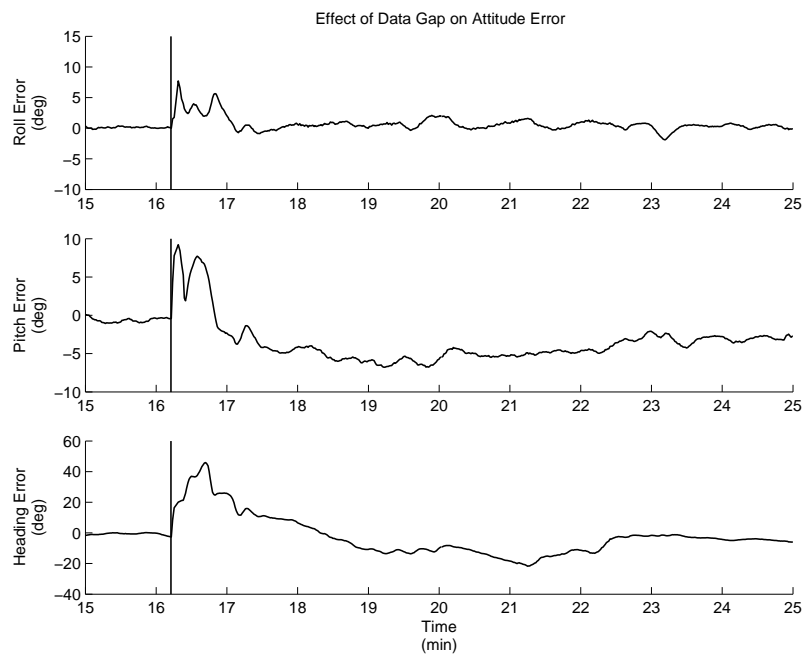


Figure 4.26 Effect of Data Gap on Attitude Error - Data Set 5 (2.2 Second Data Gap Shown By Vertical Lines)

4.4 Benefits of Head Tracker Seen in 3D Audio Analysis

Although the head tracker in its current configuration does not provide highly accurate (better than the $\pm 3^\circ$ specification) heading data to the 3D audio system on a consistent basis, using the head tracker provides a definite improvement in directional sound localization capability over not using the head tracker. Directional sound localization is the ability to generate audio cues from a specific azimuth and elevation combination. The audio cue is processed to sound as though it is coming from a certain location (i.e., spatially located).

For the localization test, data was gathered in a non-flying environment (i.e., closed door briefing room), in the aircraft on the ground with engines running, and in flight. During the in-flight test, the evaluation pilot flew the aircraft to maintain straight and level flight. The test conductor initiated a set of azimuth/elevation angle sound cues, which were presented to the pilot in a uniformly distributed random order. Twelve discrete azimuths (i.e., 1 to 12 o'clock) and 3 discrete elevations (i.e., low, medium, and high) were possible. The azimuth of the sound cue was generated with reference to the current aircraft heading. At the completion of each aural presentation, the pilot responded with the perceived direction of the sound (e.g., 3 o'clock low). The test conductor recorded the pilot's response and the commanded sound position. These tests were performed in two modes: (1) the 3D audio system coupled to aircraft attitude using GAINR data and (2) the 3D audio system coupled to head attitude using head-tracker data. When the 3D audio system is coupled to the GAINR system, the direction of sound is dependent on aircraft orientation. When the 3D audio system is coupled to the head tracker, the direction of sound is dependent on head orientation. In mode 1, the head tracker is not used, and 3D audio cues remain "fixed" to the user's orientation. For example, if a cue is presented directly in front of the user, and he turns his heads 90 degrees to the right, the cue will still be presented directly in front of him (i.e. in the direction he is looking). In mode 2, the 3D audio system is coupled to the head tracker, and sounds remain

spatially fixed. Imagine the same user facing north, and a cue is presented directly in front of him. When the user turns his head 90 degrees to the right, the cue still sounds like it is coming from the north. The MT9 IMU mounted to a headset is depicted in Figure 4.27.



Figure 4.27 MT9 IMU Mounted on Headset

It is difficult for the 3D audio system to generate discernable elevation cues, and correct elevation responses were infrequent using both configurations. Only 40 percent of the GAINR-coupled elevation angle responses were correct, both on the ground and in the air. Head tracker-coupled correct elevation responses were 42 percent on the ground and 46 percent in the air. Neither of these results are significant, since low, medium, and high are the only possibilities to choose from, and a user is likely to guess the correct response 33% of the time with no additional information from the 3D audio system. Elevation localization results are depicted in Figures 4.28 and 4.29.

On the other hand, results show a clear improvement in azimuth localization performance when using the head tracker. Without using the head tracker, only 40 percent of the azimuth angle responses were correct both on the ground and in the

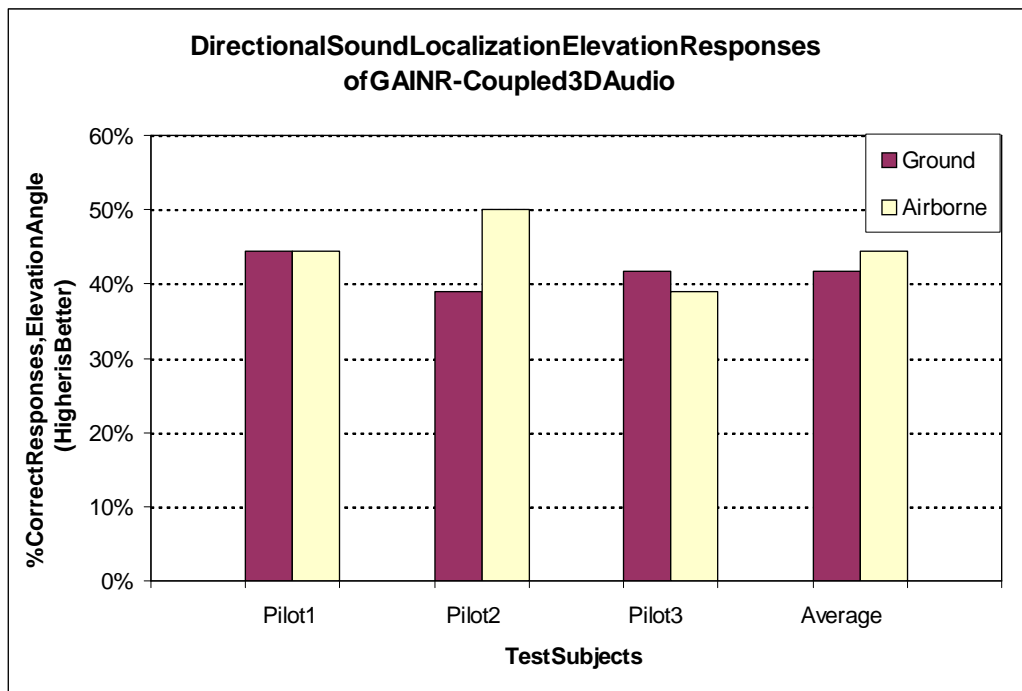


Figure 4.28 GAINR-Coupled Localization Elevation Response Performance

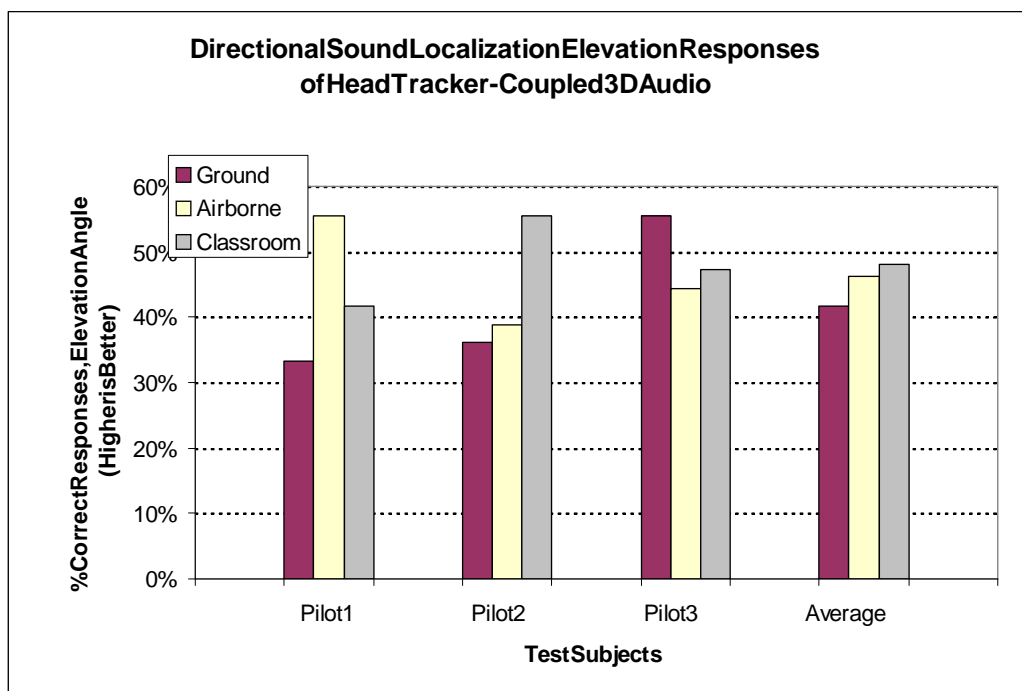


Figure 4.29 Head Tracker-Coupled Localization Elevation Response Performance

air as shown in Figure 4.30. The GAINR-coupled system was ambiguous between forward and aft azimuths. Cues from a forward azimuth (e.g., 11 o'clock) were difficult to distinguish from cues from an aft azimuth (e.g., 7 o'clock). Left and right azimuths were easily discerned.

With the system coupled to the head tracker, reported azimuth accuracy was significantly better. 56 percent of the azimuth angle responses were correct on the ground and 72 percent in the air, as shown in Figure 4.31. The head tracker-coupled system eliminated azimuth ambiguities, greatly improving the azimuth performance of the 3D Audio system.

Even though the head tracker did not meet the $\pm 3^\circ$ specification for heading accuracy, it still provided a means to determine the direction of generated sounds quickly. The heading estimates of the head tracker are not accurate enough for most realistic navigation applications, but they are accurate enough to provide real benefits to the 3D audio system. Even if head-tracker heading error is 10 degrees, this error is small when compared to the 180 degree azimuth ambiguity the user could experience with no head tracker.

As previously mentioned, some azimuths can be easily confused with other azimuths. A cue from 12 o'clock may sound very similar to a cue from 6 o'clock. A cue from 11 o'clock, however, will sound very different than a cue from 5 o'clock. If the cue is initially at 12 o'clock, it will move to the left as the user turns his head to the right. If the cue is initially at 6 o'clock, it will move to the right as the user turns his head to the right. Allowing the user to "reposition" the sound through use of the head tracker greatly improves the capability to resolve any azimuth ambiguities.

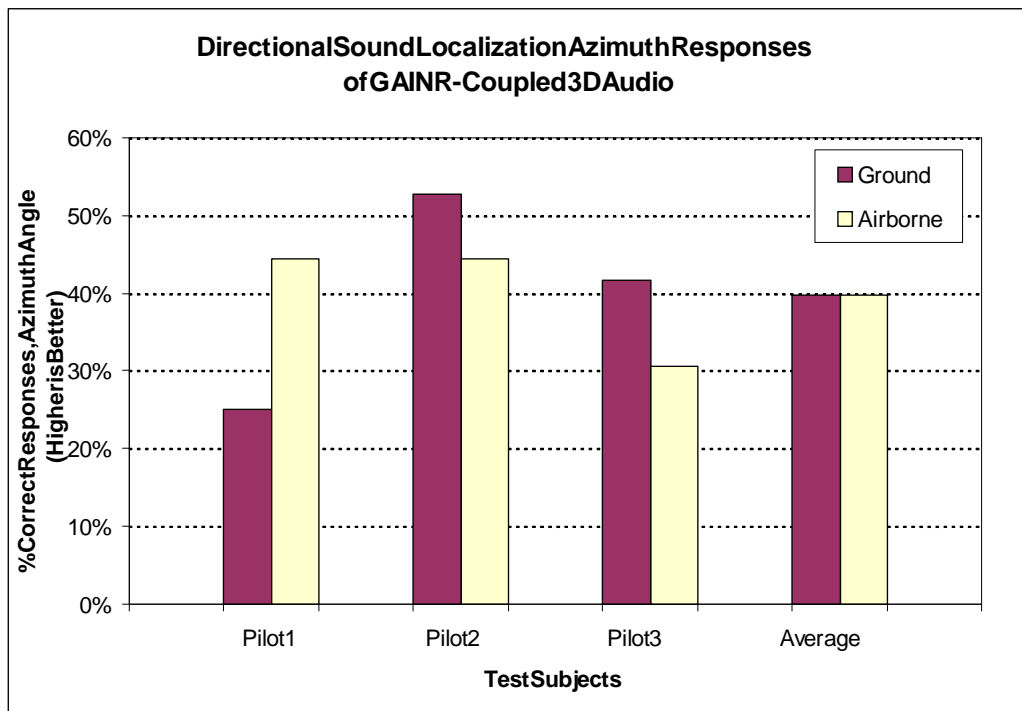


Figure 4.30 GAINR-Coupled Localization Azimuth Response Performance

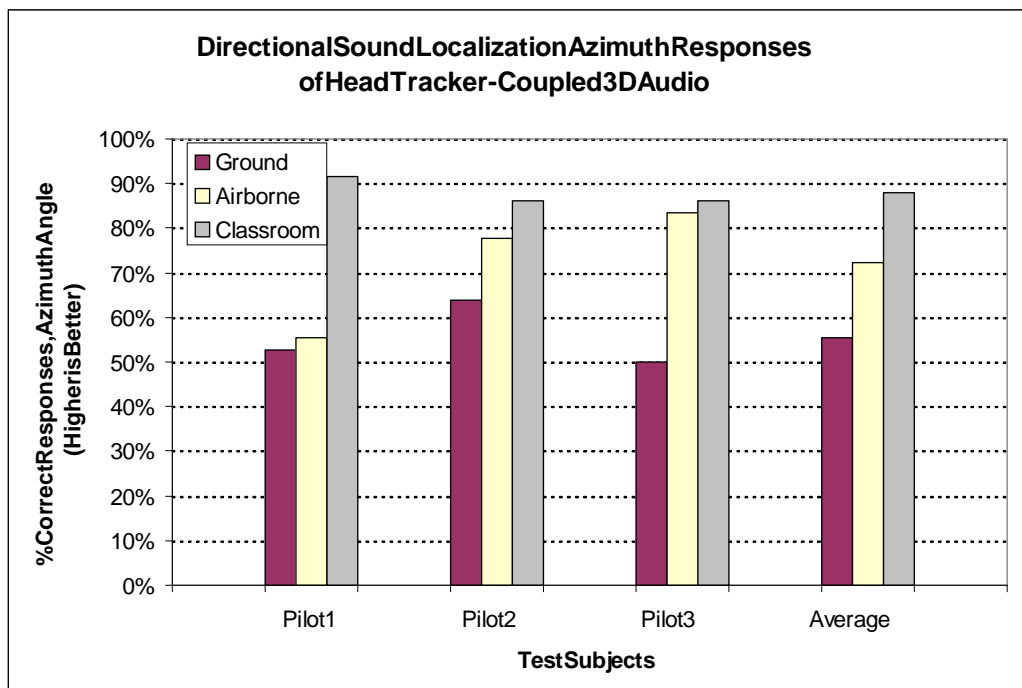


Figure 4.31 Head Tracker-Coupled Localization Azimuth Response Performance

4.5 Further Analyses

Due to time and budget constraints, only one iteration of the real-time algorithm could be evaluated in flight. The collected raw data, however, represents a valuable resource for improving the existing algorithm and expanding on the knowledge of MEMS based inertial navigation. Multiple “*what if*” questions can be addressed by post-processing the data and expanding upon what has already been learned from the real-time algorithm. The next section uses data set 2 to address a few of these questions.

Before beginning any such investigations, a comparison of real-time results to post-processed results is made using identical raw IMU data and GPS measurements from data set 2. If the results closely match, any insight gained from modifying the post-processing algorithm will likely apply to the real-time algorithm as well. This is a good assumption as long as any new computations can be performed within the time cycle limitations of the real-time algorithm. To form the comparison, outputs of the real-time algorithm and the post-processing algorithm are differenced. The outputs used in the comparison include position, velocity, and attitude error. Figures 4.32 through 4.37 show the results of this comparison. Maximum differences in position, velocity, and attitude error are 3.5 meters, 0.33 meters/second, and 1.6 degrees respectively. This comparison show that results from post-processing follow results from real-time processing, but the results do not match as closely as desired. Differences may be due to the extra propagation step in the real-time algorithm or possible due to additional Windows® related issues not fully understood. Although the results do not match as closely as desired, any improvements made to the post-processing version of the algorithm should yield similar results when applied to the real-time algorithm.

4.5.1 GPS Outage. Constant GPS availability is desired for head tracker operation, but GPS outages may be inevitable under some circumstances. Figures

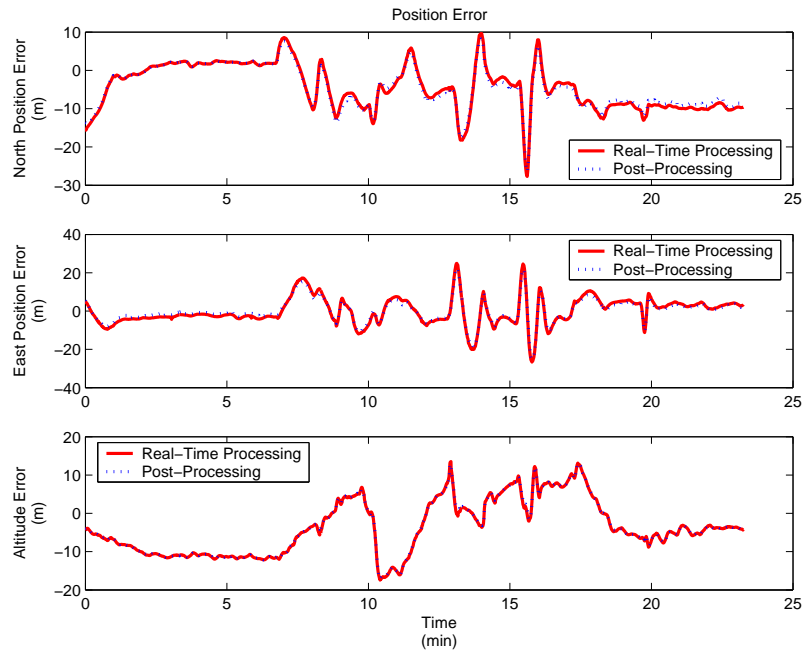


Figure 4.32 Real-Time Processing and Post-Processing - Position Error

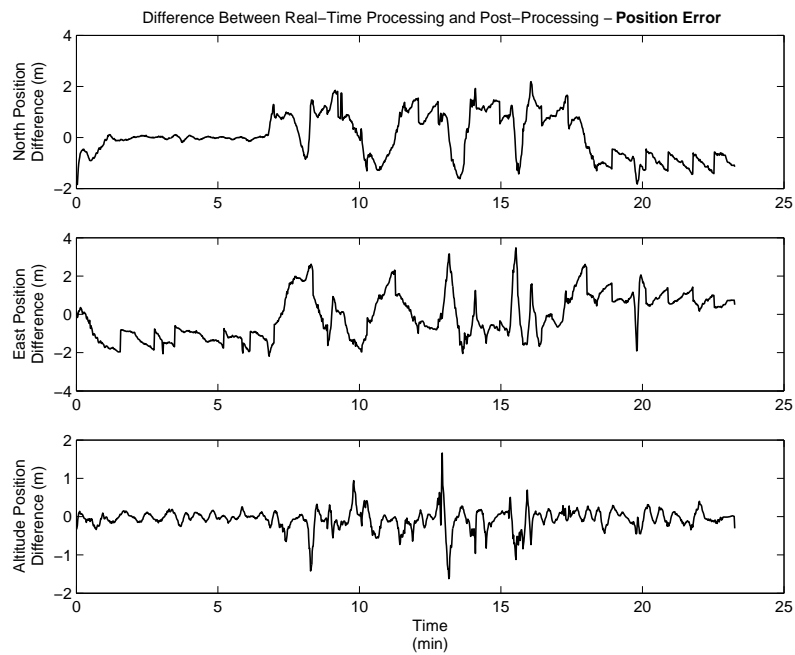


Figure 4.33 Difference Between Real-Time Processing and Post-Processing - Position Error

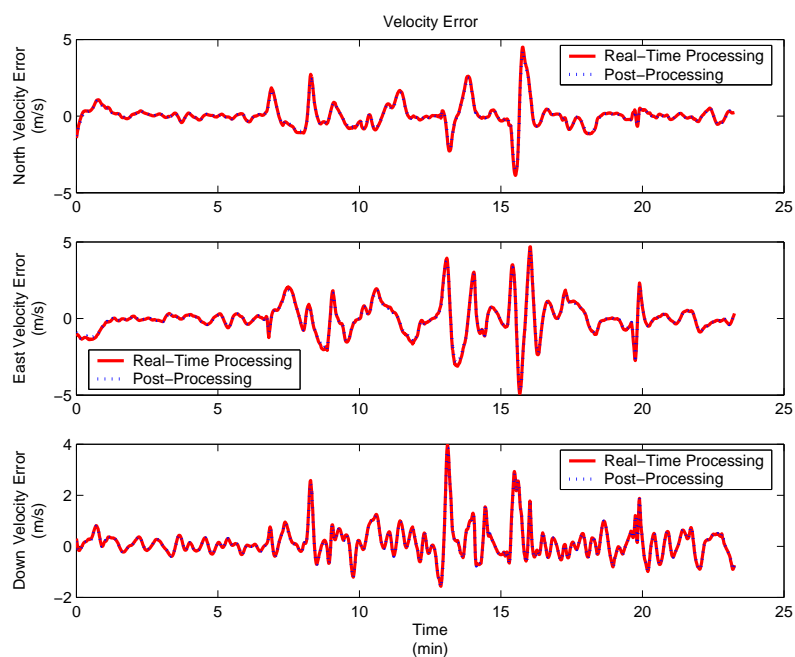


Figure 4.34 Real-Time Processing and Post-Processing - Velocity Error

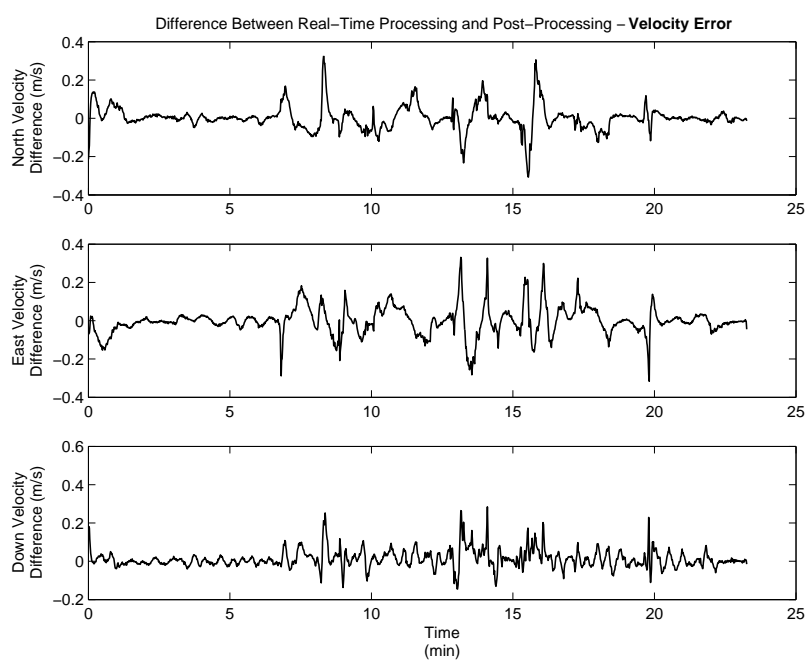


Figure 4.35 Difference Between Real-Time Processing and Post-Processing - Velocity Error

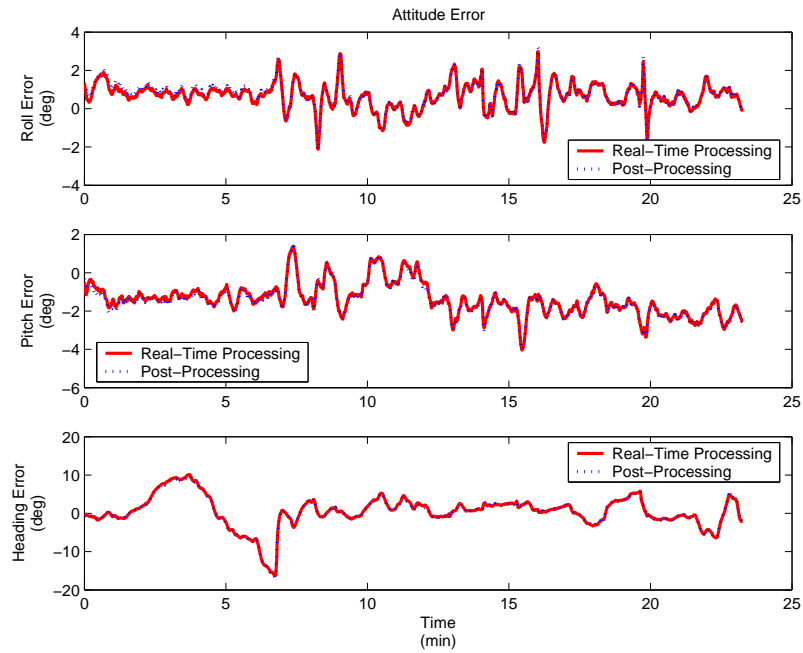


Figure 4.36 Real-Time Processing and Post-Processing - Attitude Error

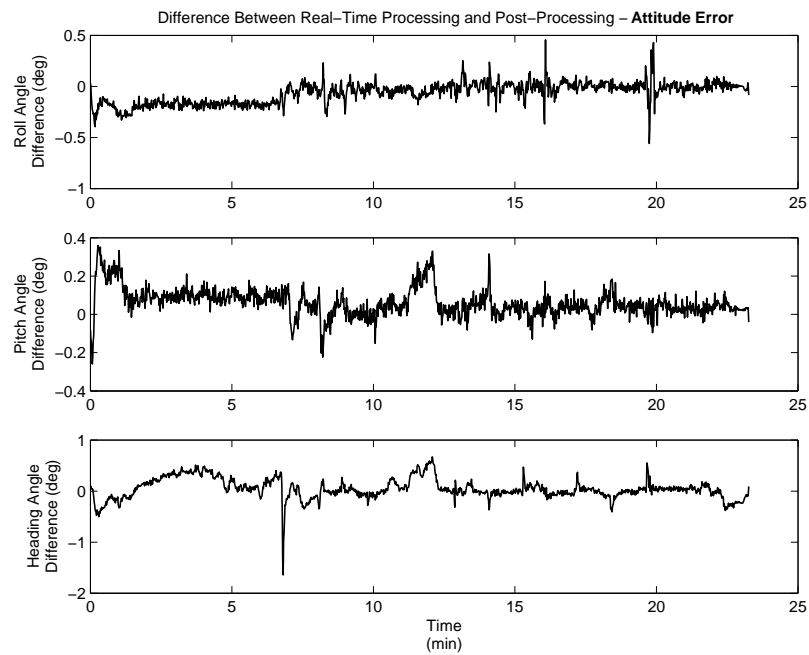


Figure 4.37 Difference Between Real-Time Processing and Post-Processing - Attitude Error

4.38 through 4.45 depict the affects of a 60 second GPS outage during SLUF and also during a 2 G turn at 60 degrees angle of bank.

The GPS outage during SLUF is more noticeable in pitch and roll than it is in heading, as seen in Figures 4.38 and 4.39. Pitch and roll errors start to grow during the GPS outage and then recover when the measurements return. The filter is already having problems with heading due to the SLUF, and the loss/return of GPS measurements does not significantly affect the heading drift. This observation agrees with the earlier discussion of heading and unaccelerated conditions. During the SLUF segment, position and velocity measurements provide benefits to pitch and roll only, since a horizontal specific force is not available to “connect” the measurements to heading. This is seen in the filter-predicted $\pm 1\sigma$ values in Figure 4.39, in which the GPS event is seen predominately in the north and east tilt states.

During the 2G turn, the GPS outage affects all three attitude states, as seen in Figures 4.40 and 4.41. The benefits of horizontal specific force cannot be fully applied in the absence of accurate measurements, and the filter-predicted $\pm 1\sigma$ values increase for all attitude states. As soon as the measurements return, horizontal specific force is still available, and heading error decreases. It is also interesting to note that pitch and roll seem to be more affected by the GPS outage during SLUF than by the outage during the turn. This is possibly due to better knowledge of the bias and drift states, as the 2G turn was proceeded by 3 other turns and the SLUF segment. Additionally, these results are from only a single instance of a stochastic process. To know more, multiple Monte Carlo runs would have to be conducted. For completeness, position and velocity error during the GPS outages are included in Figures 4.42 and 4.43 for SLUF and in Figures 4.44 and 4.45 for the 2G turn.

Both outages demonstrate that the filter is capable of coasting and recovering from GPS outages of up to 60 seconds without significant adverse effects on attitude estimation. Coasting during longer outages may be possible as well.

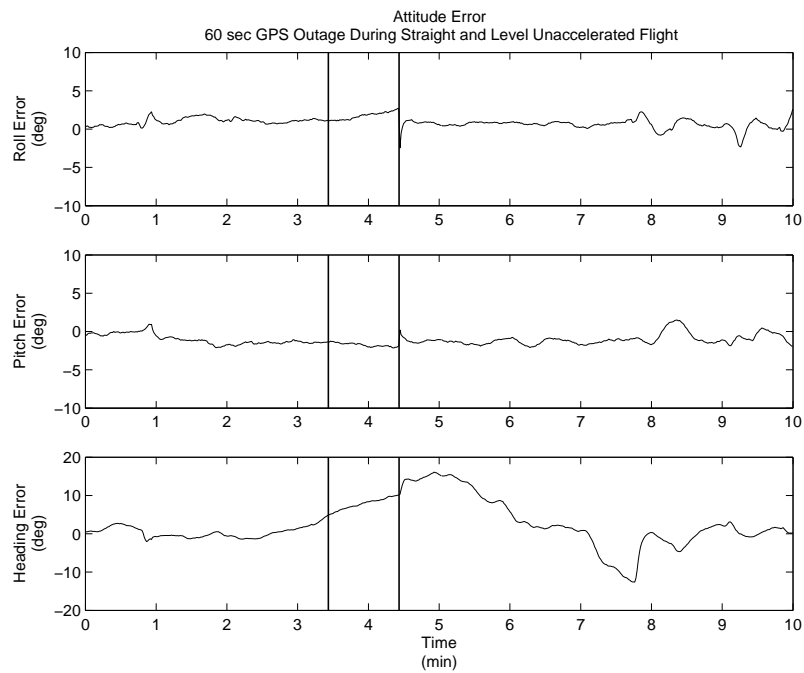


Figure 4.38 Attitude Error with 60 Second GPS Outage During SLUF

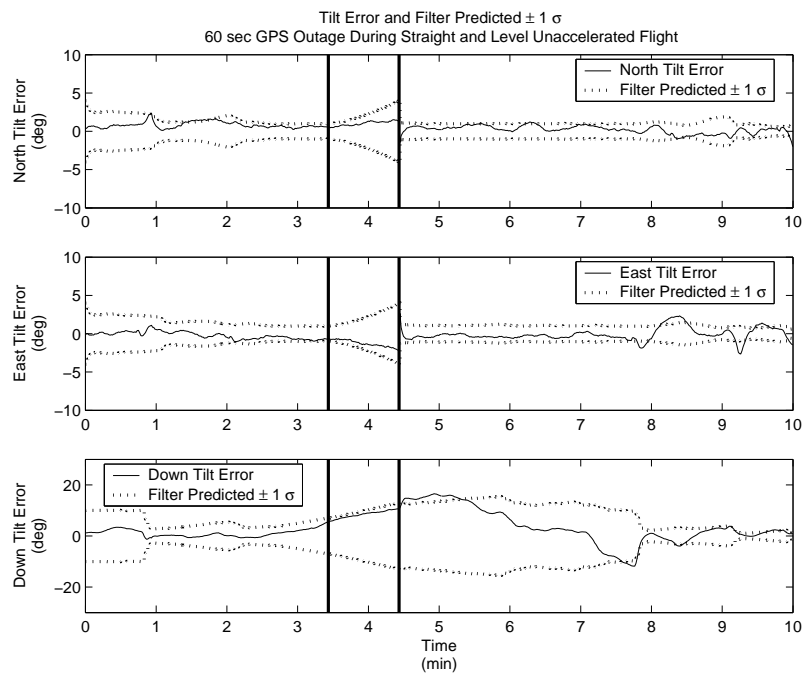


Figure 4.39 Tilt Error and Filter Predicted $\pm 1 \sigma$ with 60 Second GPS Outage During SLUF

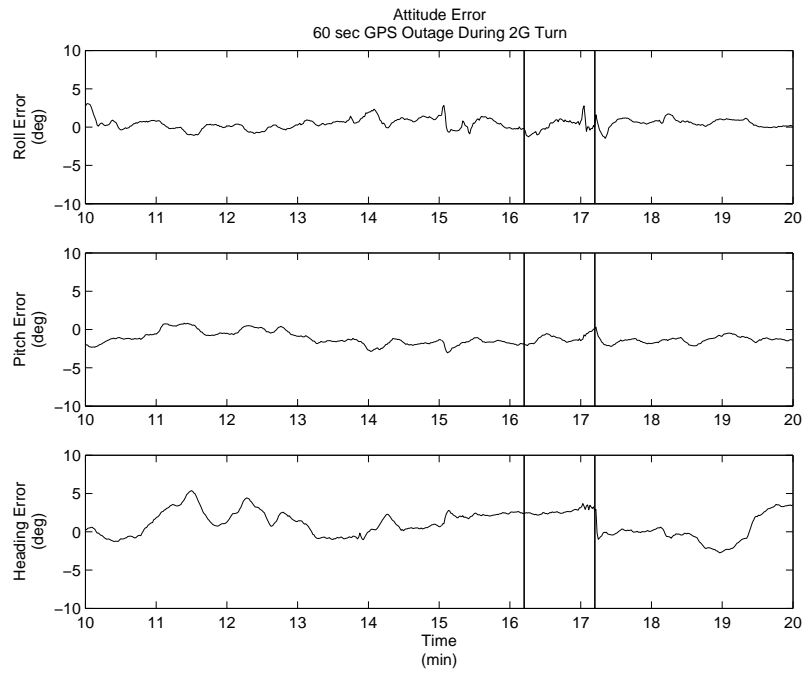


Figure 4.40 Attitude Error with 60 Second GPS Outage During 2G Turn

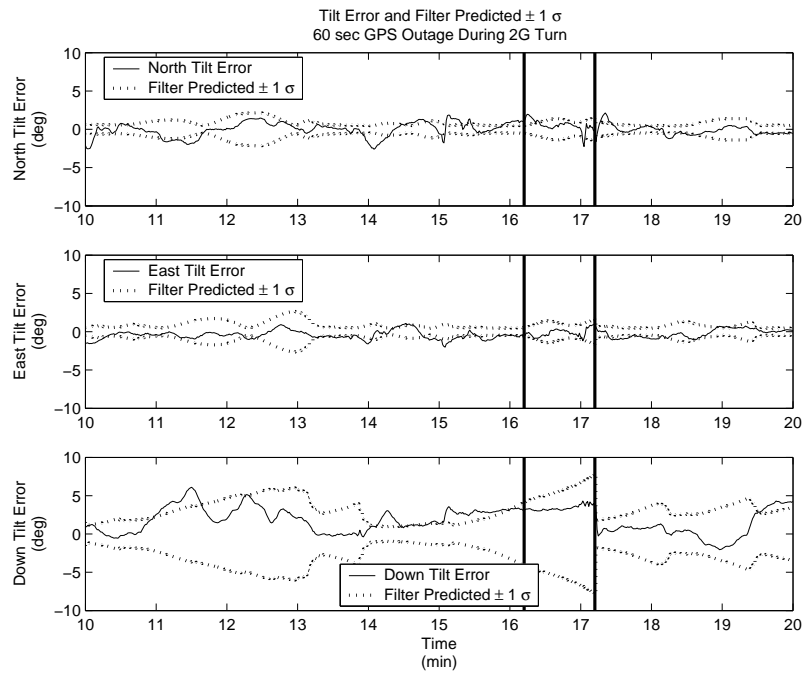


Figure 4.41 Tilt Error and Filter Predicted $\pm 1 \sigma$ with 60 Second GPS Outage During 2G Turn

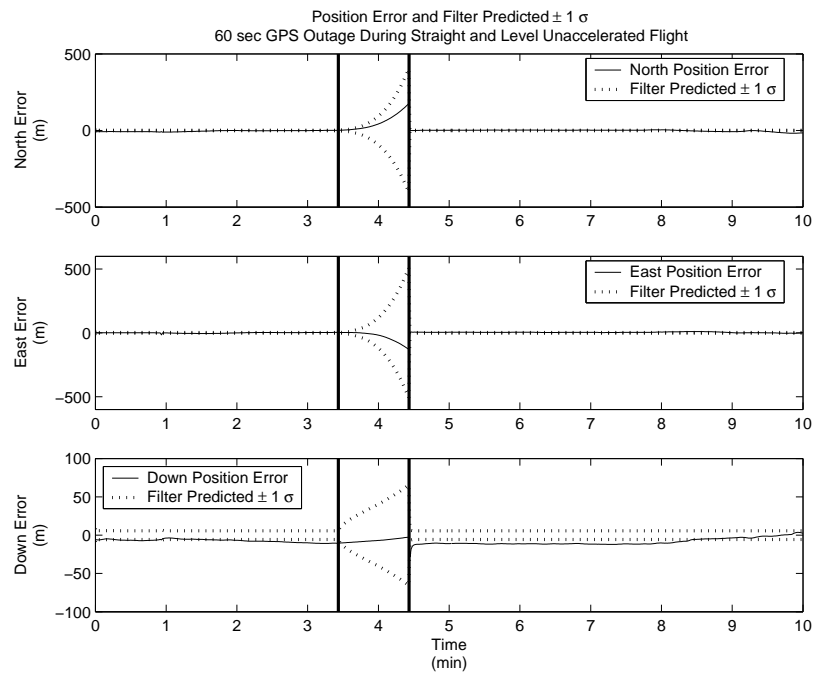


Figure 4.42 Position Error and Filter Predicted $\pm 1 \sigma$ with 60 Second GPS Outage During SLUF

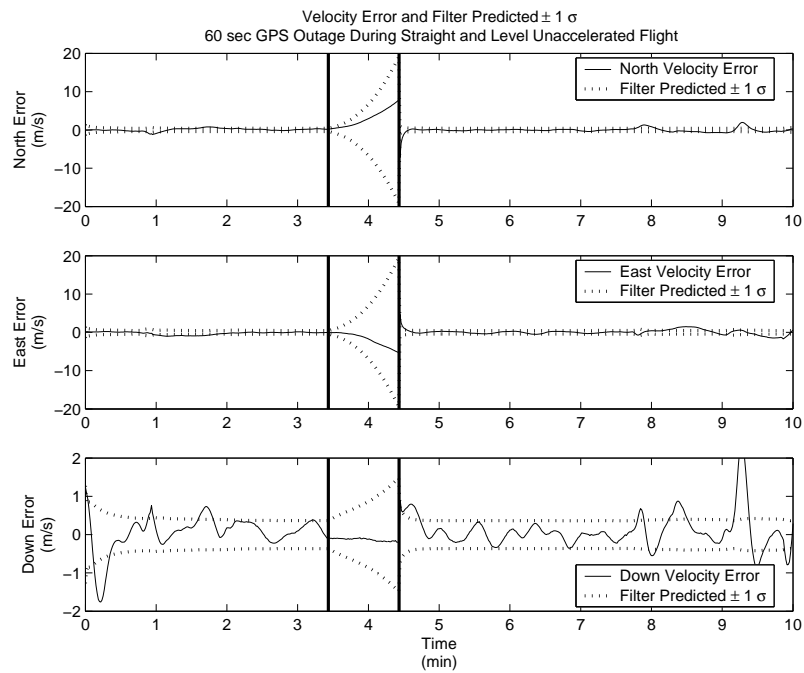


Figure 4.43 Velocity Error and Filter Predicted $\pm 1 \sigma$ with 60 Second GPS Outage During SLUF

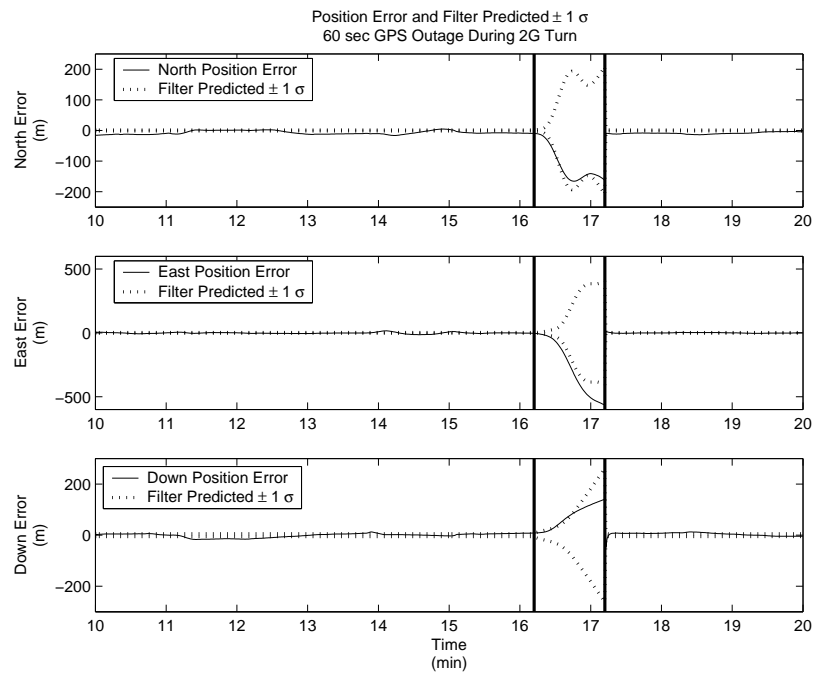


Figure 4.44 Position Error and Filter Predicted $\pm 1 \sigma$ with 60 Second GPS Outage During 2G Turn

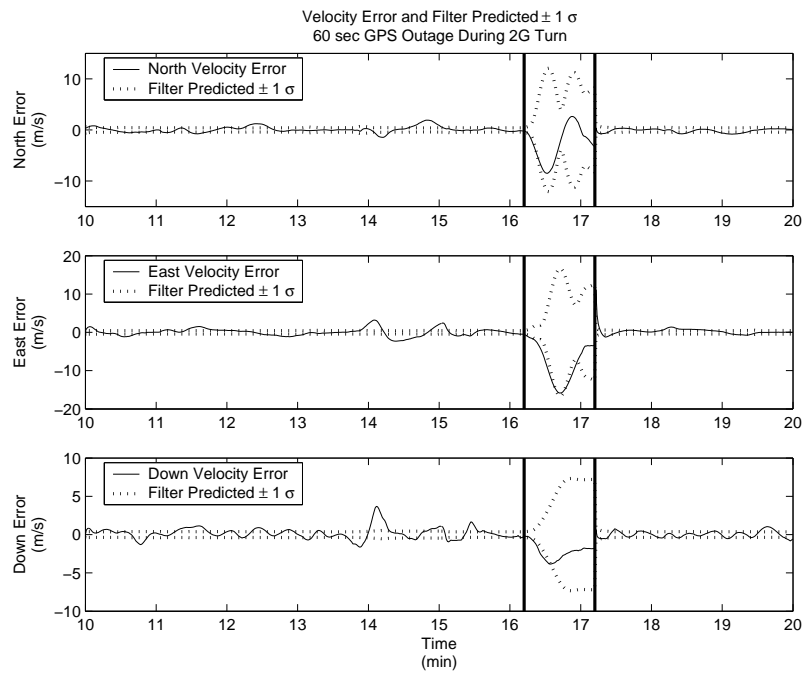


Figure 4.45 Velocity Error and Filter Predicted $\pm 1 \sigma$ with 60 Second GPS Outage During 2G Turn

4.5.2 GPS Course Measurement. Since the MEMS-based system has the most difficulty estimating heading, one method to improve performance is the addition of a GPS-based course measurement (course refers to the direction of the velocity vector, while heading refers to the direction the aircraft body is pointing). This technique would not help the head-tracker application, since aircraft course and head orientation may be very different. It might, however, prove to be a valid source of information for a low-cost Attitude and Heading Reference System (AHRS). If the direction of the GPS velocity vector is calculated, it will provide an estimate of aircraft course. Aircraft course and heading are related by wind direction and magnitude. The difference between course and heading depends on the velocity of the aircraft and the velocity of the air mass in which the aircraft is flying. The effects of the wind can be seen in Figure 4.46, which shows actual TSPI heading and TSPI course derived from velocity data.

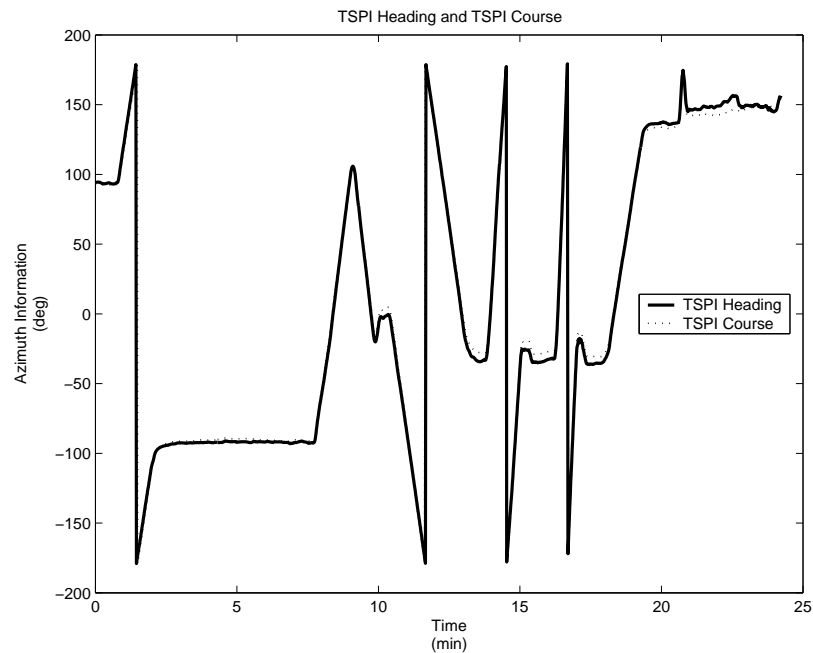


Figure 4.46 TSPI Course and TSPI Heading

Winds aloft in the Edwards local area are predominantly from the west, and deviations from course and heading appear to be greater when the aircraft is on a northerly or southerly heading. Figure 4.47 shows the difference in TSPI course and TSPI heading. Clearly course is not an ideal heading measurement, but it is safe to say that some information about aircraft heading can be extracted from GPS-based course which very closely matches TSPI course, as depicted in Figure 4.48. Aircraft heading will be approximated as GPS course, and an appropriate amount of measurement noise will be applied. Using the same measurement scheme as before, the heading (γ) difference measurement can be defined as

$$z_\gamma = \gamma_{GPS} - \gamma_{INS} = \delta\gamma + v \quad (4.1)$$

and using a 4-quadrant arctan function,

$$\gamma_{GPS} = \arctan \left[\frac{v_{E_{GPS}}}{v_{N_{GPS}}} \right] \quad (4.2)$$

The new measurement vector \mathbf{z} is then

$$\mathbf{z} = \begin{bmatrix} z_{lat} \\ z_{lon} \\ z_{alt} \\ z_{v_n} \\ z_{v_e} \\ z_{v_d} \\ z_\gamma \end{bmatrix} \quad (4.3)$$

and the new 7 x 15 measurement matrix \mathbf{H} is

$$\mathbf{H} = \begin{bmatrix} 1 & 0 & 0 & 0 & 0 & 0 & 0 & 0 & 0 & 0 & 0 & 0 \\ 0 & 1 & 0 & 0 & 0 & 0 & 0 & 0 & 0 & 0 & 0 & 0 \\ 0 & 0 & 1 & 0 & 0 & 0 & 0 & 0 & 0 & 0 & 0 & 0 \\ 0 & 0 & 0 & 1 & 0 & 0 & 0 & 0 & 0 & 0 & 0 & \dots \\ 0 & 0 & 0 & 0 & 1 & 0 & 0 & 0 & 0 & 0 & 0 & 0 \\ 0 & 0 & 0 & 0 & 0 & 1 & 0 & 0 & 0 & 0 & 0 & 0 \\ 0 & 0 & 0 & 0 & 0 & 0 & 0 & 0 & -1 & 0 & 0 & 0 \end{bmatrix}$$

The -1 is used because tilt error is positive in the down direction (due to north, east, down mechanization), and the measurement is in the up direction.

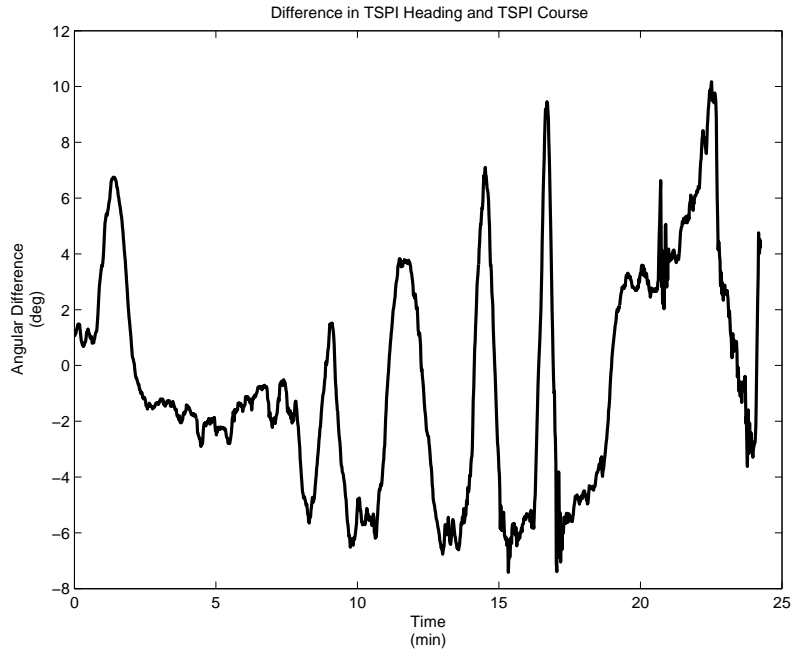


Figure 4.47 Difference between TSPI Heading and TSPI Course

Results using the new measurement and a measurement noise standard deviation of 35 degrees are depicted in Figure 4.49. The 35 degree measurement noise standard deviation provided the best performance (for data set 2) when compared

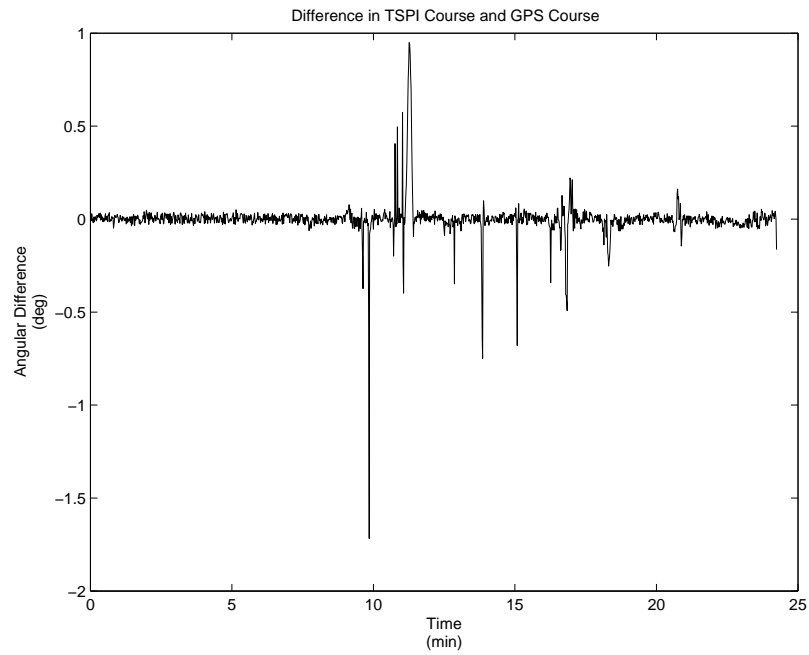


Figure 4.48 Difference between TSPI Course and GPS Course

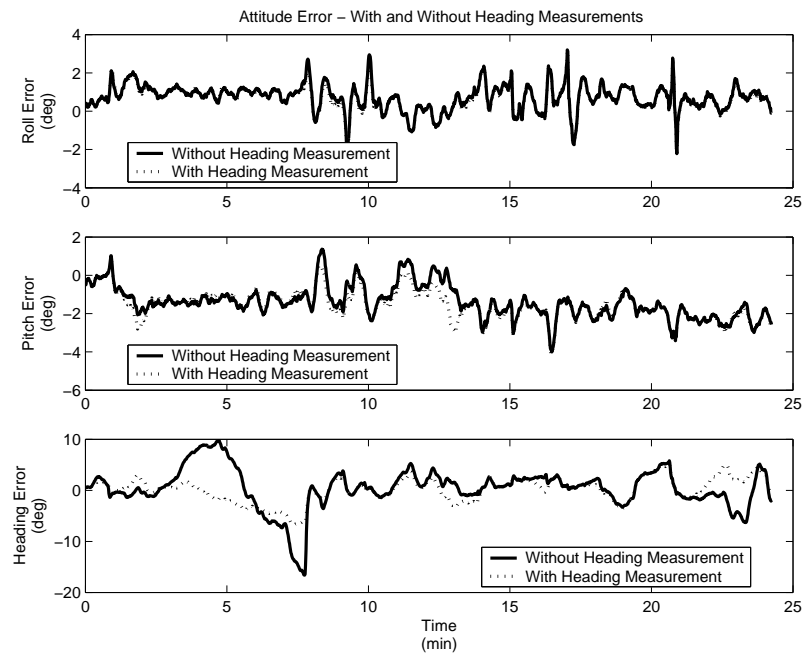


Figure 4.49 Attitude Error with and without GPS Heading Measurement

to measurement noise standard deviations of 20, 25, 30, 40, 45 and 50 degrees. The greatest benefits are seen in the SLUF segment when the filter is the least sure of heading error. Filter-predicted standard deviation for down tilt error is somewhat bounded as a result of the heading measurement, as seen in Figure 4.50. Improved performance of the system is verified using the established evaluation criteria. The percentage of heading error samples within the $\pm 3^\circ$ bounds increases from 70% without the heading measurement to 79%, with the measurement. The percentage within $\pm 7^\circ$ also improves from 91% to 100%. As expected, no performance improvements are seen in roll and pitch.

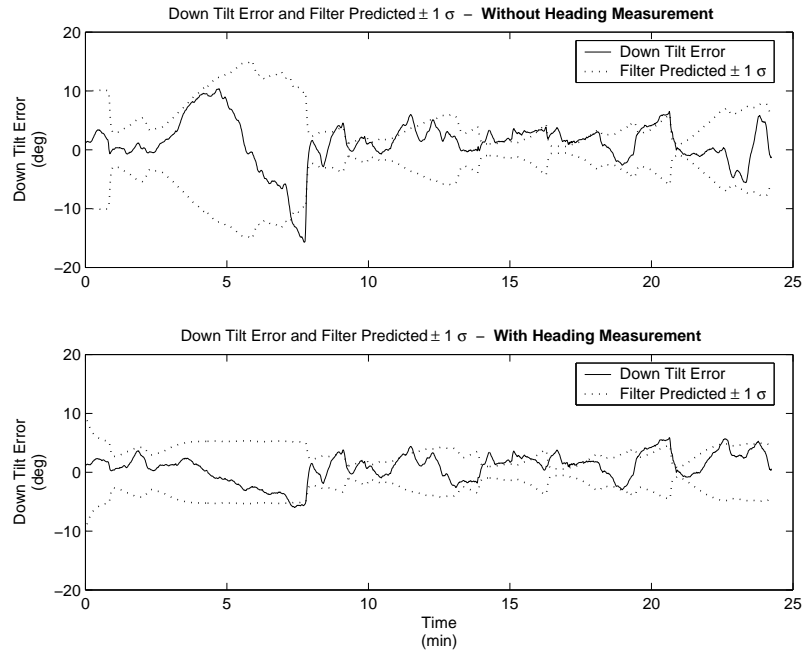


Figure 4.50 Tilt Error and Filter Predicted $\pm 1 \sigma$ with and without GPS Heading Measurement

4.5.3 Simplified Dynamics Model. Many of the terms in the dynamics model are smaller than the noise levels from the MEMS IMU. For example, the typical noise standard deviation from the MT9 gyros and accelerometers are 8.3×10^{-3} rad/sec and 2.0×10^{-2} m/sec² respectively. In contrast, the angular velocity

of the earth is 7.3×10^{-5} rad/sec and falls below the noise floor of the MT9 gyro outputs. This flight test was conducted predominately at an altitude of 12,000 feet with maximum velocities around 200 knots true airspeed. This equates to a maximum transport rate of 1.6×10^{-5} rad/sec and a centripetal acceleration of 1.5×10^{-3} m/sec². All of these fall well below the noise levels of their respective sensors. The Coriolis acceleration of 1.2×10^{-2} m/sec², although not sensed by the accelerometers, would eventually lead to a position error if not taken into account in a free inertial type system. Since the head tracker receives GPS measurements on a regular basis, ignoring Coriolis acceleration should not be a problem. Based on the noise characteristics of the IMU, it is likely that errors in the system are dominated by other factors—namely accelerometer bias and gyro drift.

Since the benefits of a full dynamics model are not realized, a simplified model may provide equal performance and require less computational resources. Equation (3.16) from Section 3.2.5 is repeated as

$$\dot{\mathbf{v}}^n = \mathbf{C}_b^n \mathbf{f}^b - (2\boldsymbol{\omega}_{ie}^n + \boldsymbol{\omega}_{en}^n) \times \mathbf{v}^n + \mathbf{g}^n$$

Removing the Coriolis term and the centripetal acceleration term leaves

$$\dot{\mathbf{v}}^n = \mathbf{C}_b^n \mathbf{f}^b + \mathbf{g}^n \quad (4.4)$$

Forming the error equation and ignoring errors in the knowledge of gravity gives

$$\delta \dot{\mathbf{v}}^n = \mathbf{f}^n \times \boldsymbol{\Psi} + \mathbf{C}_b^n \delta \mathbf{f}^b \quad (4.5)$$

where $\boldsymbol{\Psi} = [\delta\alpha \ \delta\beta \ \delta\gamma]^T$ is the misalignment angle vector and $\delta \mathbf{f}^b$ is the accelerometer bias vector.

The attitude error dynamics, included in the Pinson error model presented in Section 3.3.1, can be approximated as

$$\dot{\Psi} \approx -\omega_{\text{in}}^{\text{n}} \times \Psi + \delta\omega_{\text{in}}^{\text{n}} - \mathbf{C}_{\text{b}}^{\text{n}} \delta\omega_{\text{ib}}^{\text{b}} \quad (4.6)$$

Ignoring the earth rate and transport rate terms leaves

$$\dot{\Psi} \approx -\mathbf{C}_{\text{b}}^{\text{n}} \delta\omega_{\text{ib}}^{\text{b}} \quad (4.7)$$

where $\delta\omega_{\text{ib}}^{\text{b}}$ is the gyro drift vector. Finally the position error dynamics can be expressed as

$$\delta\dot{\mathbf{p}} = \delta\mathbf{v} \quad (4.8)$$

Applying the simplifications to the dynamics matrix \mathbf{F} , Equation (3.21) reduces to

$$\mathbf{F} = \begin{bmatrix} \mathbf{0} & \mathbf{PV} & \mathbf{0} & \mathbf{0} & \mathbf{0} \\ \mathbf{0} & \mathbf{0} & \mathbf{VA} & \mathbf{VB} & \mathbf{0} \\ \mathbf{0} & \mathbf{0} & \mathbf{0} & \mathbf{0} & \mathbf{AD} \\ \mathbf{0} & \mathbf{0} & \mathbf{0} & \mathbf{0} & \mathbf{0} \\ \mathbf{0} & \mathbf{0} & \mathbf{0} & \mathbf{0} & \mathbf{0} \end{bmatrix} \quad (4.9)$$

These partitions, introduced in Section 3.3.1, are repeated below.

$$\mathbf{PV} = \begin{bmatrix} \frac{1}{R} & 0 & 0 \\ 0 & \frac{1}{R \cos L} & 0 \\ 0 & 0 & -1 \end{bmatrix}$$

$$\mathbf{VA} = \begin{bmatrix} 0 & -f_D & f_E \\ f_D & 0 & -f_N \\ -f_E & f_N & 0 \end{bmatrix}$$

$$\mathbf{VB} = \mathbf{C}_b^n$$

$$\mathbf{AD} = -\mathbf{C}_b^n$$

A performance comparison between the current system (using the full dynamics model) and a reduced system (using the simplified dynamics model) is needed in order to validate the simplification. Figures 4.51 through 4.53 show the differences between the two models with respect to position, velocity, and attitude errors using post-processed data from data set 2. The plots show that using either model produces essentially the same results. Under closer scrutiny, the maximum differences between the two models for position, velocity, and attitude are 0.7 centimeters, 0.36 centimeters/second, and 0.069 degrees, respectively. For all practical purposes, the models are equivalent, and the simplified model can be used safely under similar conditions.

4.6 Chapter Summary

This chapter provided background information on equipment set up as well as test methodology. Flight test results were presented primarily for the head tracker system, but also for the 3D audio system coupled to the head tracker. Finally, further analysis of the system was discussed to include GPS outages, the incorporation of GPS course information, and the use of a simplified dynamics model.

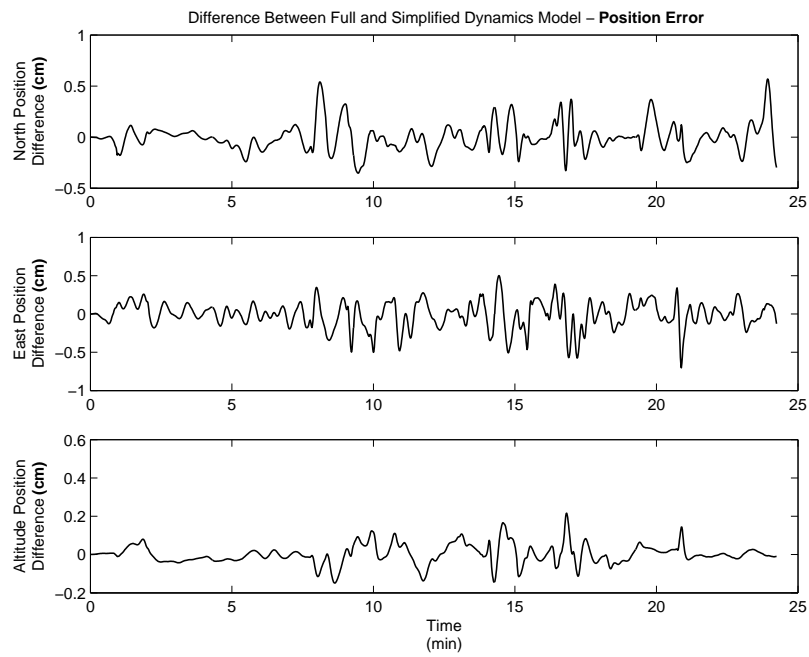


Figure 4.51 Difference Between Full and Simplified Dynamics Model - Position Error

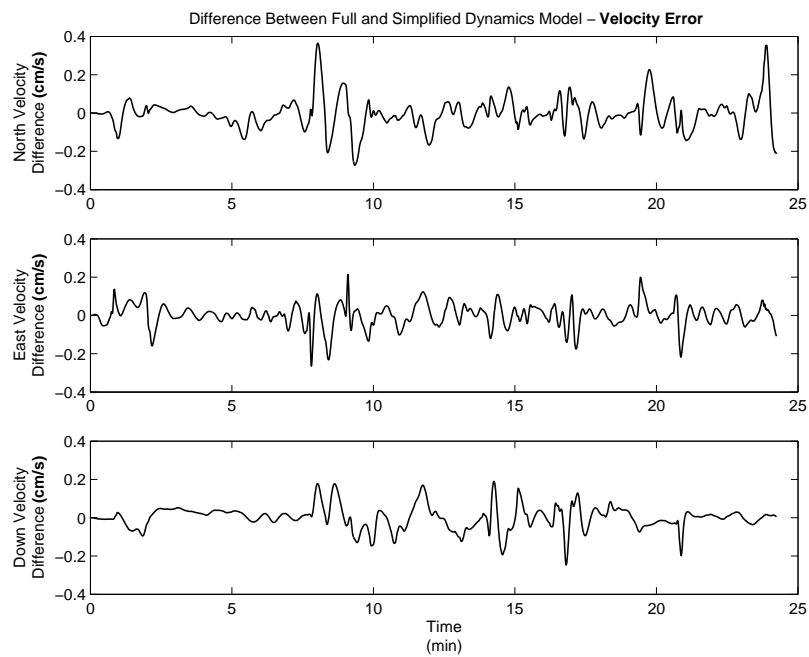


Figure 4.52 Difference Between Full and Simplified Dynamics Model - Velocity Error

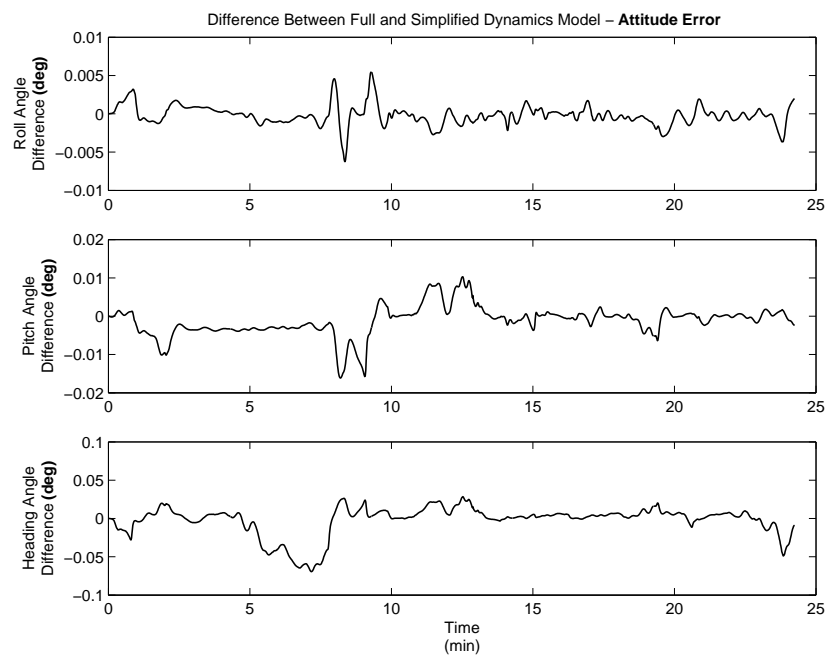


Figure 4.53 Difference Between Full and Simplified Dynamics Model - Attitude Error

V. Conclusions and Recommendations

5.1 Overview

The goal of this research was to expand the knowledge of low-cost MEMS IMU technology in aviation. The system was designed around the specific application of inertial head tracking for 3D audio in aviation, but the lessons learned should provide benefits to other applications as well.

This research on head tracking for 3D audio using a GPS-aided MEMS IMU began with background information on 3D audio and a summary of previous work. Relevant information on inertial navigation, Kalman filtering, and INS/GPS integration was included to provide theory behind the design of the system. The details of the algorithm were explained to include the local-level INS mechanization, design of the system Kalman filter, and overall implementation of the INS/GPS integration. Finally, the results of real-time operation during flight were examined, and further analysis was conducted through post-processing. A summary of the key conclusions as well as recommendations for further research follows below.

5.2 Conclusions

- **Degraded performance in heading can be traced to the quality of the sensors and to the conditions of flight.** Errors in the outputs of the MEMS gyros and accelerometers will produce large errors in the INS navigation solution, since their outputs are integrated from an initial condition. If the errors in the sensors are accurately estimated, a reasonable navigation solution can be provided. In order to provide accurate estimates of the sensor errors, independent information (which can be directly or indirectly related to the sensor errors) must be available. The head tracker receives independent information from GPS measurements that can be used to infer information indirectly about

the sensor errors through the dynamics and measurement models. When the only independent information available comes in the form of GPS position and velocity measurements, examination of the system model shows that information about heading error can only be inferred in the presence of horizontal acceleration. Strictly speaking, heading error is only observable if specific force is present in the horizontal plane. This lack of observability was demonstrated in the flight test. Specifically, the segments of straight-and-level unaccelerated flight, steady heading side slips, constant G turns, and the takeoff roll provide the needed comparison to make this conclusion.

- **A precise alignment will pay dividends in the long run.** This conclusion seems blatantly obvious, but the importance of an accurate alignment should not be forgotten. One might be led to believe that any benefits from a precise alignment will be quickly lost due to the large sensor errors indicative of a MEMS IMU. This is true to a certain extent, but estimates of the sensor errors will improve if the system starts from an accurate initial condition. With better estimates of sensor errors, overall system performance will improve. The comparison of the magnetometer alignment to the GAINR alignment confirms this. Heading accuracy using the GAINR alignment improves almost two-fold. The number of heading samples that fell within $\pm 3^\circ$ of the actual heading increased from 27% to 53%. The number of samples within $\pm 7^\circ$ increased from 51% to 83%. Modest improvements were seen in pitch and roll accuracy as well.
- **Windows[®] is not a suitable operating environment to conduct real-time processing at a 100-Hz rate.** The large gaps in IMU data (up to 2.5 seconds) are unacceptable. If this system is expected to provide a reasonable navigation solution, the raw data must arrive to the algorithm in a consistent and reliable manner. The integration of the DCM and navigation frame

accelerations assumes a small time step. Any unexpected violation of this assumption will lead to decreased performance and possibly filter divergence.

- **3D audio azimuth sound localization capability is improved with the addition of a head tracker.** Even with its current heading accuracy, the head tracker provides the capability to solve azimuth ambiguities common to the 3D audio cues. The user can quickly reposition the cue and refine its perceived direction. Correct azimuth localization responses improved from 40% without use of the head tracker to 72% with use of the head tracker. Certainly, even larger improvements in azimuth localization are possible if the heading accuracy of the head tracker is improved.
- **GPS outages of up to 60 seconds do not significantly affect head-tracker attitude performance.** The head tracker system is capable of coasting during, and recovering after, short GPS outages with no significant change to attitude performance, as seen in the GPS outages during SLUF and during turning flight.
- **The addition of GPS azimuth information improves heading accuracy.** Modest improvements in heading accuracy (from 70% to 79% within the $\pm 3^\circ$ bounds) can be expected with the addition of GPS course information. Although heading and course may differ by several degrees based on the effects of the wind, some information about true aircraft heading may be extracted from the course measurement. This measurement can be used to help bound heading drift during periods of unaccelerated flight. The usefulness of a course measurement depends on the application. Very little benefit, if any, would be seen in the head-tracker application. However, the measurement would be very useful in a ground vehicle in which heading and course are usually the same (unless the vehicle is skidding). Benefits to air vehicles would vary, depending on the average velocity of the vehicle and the average velocity of the air mass in which it operates (e.g., blimp vs. ballistic missile).

- **A simplified dynamics model can be used without a noticeable degradation in performance.** Some of the terms in the full dynamics model are smaller than the noise values of the sensors in the IMU. For operations under similar conditions as the flight test, the reduced dynamics model can be used with almost exactly the same results. Using the simplified model will reduce computational requirements and free up computational resources that can be used to improve the algorithm in other ways.

5.3 Recommendations

Use of a low-cost MEMS IMU showed promising results in this evaluation. Potential for further improvements in the current system exist, and continued research is warranted for the head-tracker application and other applications as well. The following recommendations for future research will hopefully expedite the continued development of this and similar systems.

- **Port the real-time algorithm to an embedded processor.** The use of MATLAB[®] in a Windows[®] environment works fine for post-processing, but the varying latencies and loss of data inherent in real-time processing under the Windows[®] operating system limits the current capability and potential future capability of the system. The real-time algorithm should be executed under an operating system that is solely dedicated to the task. In addition, the real-time algorithm should be implemented in a low-level language instead of MATLAB[®]. This would require more intimate knowledge of the internal operation of the microprocessor, but more control could be exerted over the delicate timing scheme required for real-time operation.
- **Use a tightly-coupled INS/GPS integration.** The measurement noise will be much less correlated in time than in the loosely-coupled configuration where the measurements are products of the GPS receiver's own algorithm. This will improve the Kalman Filter estimates.

- **Use the simplified dynamics model.** Results show that there is no benefit to using the full dynamics model in this application or similar applications. Using the reduced model will free up computational resources—namely in the formulation of the state transition matrix.
- **Determine head orientation in two steps.** If orientation of the user's head with respect to the local-level reference frame is desired, it may be more realistic to form the DCM in two steps. INS/GPS integration could be used to provide orientation of the aircraft with respect to the local-level reference frame, and a separate technology could be used to determine head orientation with respect to the aircraft. The final desired orientation could be derived from the two transformations. Probably the two strongest candidates for head tracking inside an aircraft are the spatial scan optical technique [26] or the time of flight pulsed infrared diode technique [26], both mentioned in Chapter 1. Restricting the INS/GPS system to aircraft orientation may make it easier to improve heading accuracy, as already seen in the addition of GPS course information.
- **Experimentation should be accomplished with a higher quality IMU.** A wide variety of MEMS IMUs are available. A higher quality IMU should be used to see if the benefits of the higher quality sensors outweigh the additional cost. Furthermore, using a different IMU may bring additional insight to the existing algorithm.
- **A better stationary alignment technique needs to be developed.** The magnetometer alignment is too inaccurate and inconsistent to be of much use. Even a user-entered heading would be more accurate. It may be necessary to postpone any alignments until course information is readily available. One option is to perform the alignment while taxiing from the parking apron to the runway. While still on the ground, course and heading will be equal. The drawback is that there must be an opportunity to taxi unaccelerated long

enough to accomplish the alignment. In addition, any bumps in the taxiway may corrupt the alignment.

- **Use a different GPS receiver.** Three main deficiencies exist in the Garmin GPS 35 receiver. First of all, there is no provision to use an external antenna. The initial plan was to place the receiver on the glare shield in front of the pilot. Wire mesh inside the windshield used for deicing made reception of GPS signals problematic. As a result, the receiver had to be taped to a side window. This was not optimal because the antenna inside the receiver had a clear view of only a portion of the sky. In addition, this placement of the receiver made it much more susceptible to multipath error from the adjacent aircraft wing and other sections of the aircraft. A GPS antenna was available for use on top of the aircraft tail, but it could not be utilized since the Garmin GPS 35 had no provision for an external antenna. Secondly, the apparent 0.05 second delay in the receiver solution is undesirable, since it must be taken into account in any comparison to truth data. Lastly, the output rate of the receiver was limited to 1-Hz. Measurements provided at a faster rate may improve overall system performance. Whatever receiver is used in the future, it should address these deficiencies as well as provide raw measurements for a tightly-coupled integration.
- **Collect raw data early enough to allow sufficient time for algorithm development prior to evaluating the real-time system for its primary application.** As previously mentioned, minimal time was available between initial collection of raw data and evaluation of the system for its primary application. Truth data was available from the initial raw data collection flight three days before the evaluation of the real-time algorithm with the IMU fixed to the aircraft body frame. Evaluation of the head tracker mounted to a headset had to be accomplished on the very next day! This was due to unavoidable time constraints. Performance of the system as a head tracker would have been bet-

ter, without a doubt, if more time had been available to refine the algorithm. If at all possible, collect raw data and truth data months in advance to the evaluation of any real-time system. The benefits will be well worth it. As a minimum, collect raw data and truth data in a dynamic ground evaluation prior to flight test.

- **Incorporate better azimuth measurements.** As a preliminary measure, GPS course was approximated as aircraft heading to form a measurement of heading error as described in Section 4.5.2. A better method to incorporate this information would be to estimate the crab angle ξ (i.e., the difference between heading and course). As a start, this angle could be modeled as a first order Gauss-Markov process. The crab angle (ξ) measurement could be defined as

$$z_{\xi} = \text{CRS}_{GPS} - (\gamma_{INS} + \delta\gamma) = \xi - \delta\gamma + v \quad (5.1)$$

and using the same 4-quadrant arctan function

$$\text{CRS}_{GPS} = \arctan \left[\frac{v_{E_{GPS}}}{v_{N_{GPS}}} \right] \quad (5.2)$$

The new corresponding row in the \mathbf{H} matrix would be

$$\mathbf{H}_{(7,1...16)} = \begin{bmatrix} 0 & 0 & 0 & 0 & 0 & 0 & 0 & 0 & 0 & -1 & 0 & 0 & 0 & 0 & 0 & 0 & 1 \end{bmatrix} \quad (5.3)$$

If true air speed is available, a better method would be to estimate north and east wind velocity using true air speed measurements and INS velocity. Then the relationship between wind, heading, and course could be applied.

- **Improve the post-processing algorithm to match more closely the real-time algorithm.** In theory, the exact same results should be produced by both algorithms, if each algorithm is given the same raw IMU data and measurements data. With a better post-processing algorithm in hand, better

predictions can be made of real-time operation. Investigations can be limited to worthwhile improvements, reducing the amount of expensive flight time required to evaluate the system.

- **Investigate using a closed-form DCM propagation.** If we assume that the angular rate ω is constant over a small time step (an assumption already being applied in the current DCM propagation), then a closed-form solution to the DCM matrix differential equation can be formed. The closed-form solution is developed in [21] and is repeated below:

$$\begin{aligned}
\mathbf{C}(t + \tau) &= \mathbf{C}(t)e^{\mathbf{\Omega}\tau} \\
&= \mathbf{C}(t) \left[\mathbf{I} + \frac{1}{\omega} \sin \omega\tau \mathbf{\Omega} + \frac{1}{\omega^2} (1 - \cos \omega\tau) \mathbf{\Omega}^2 \right] \\
&= \mathbf{C}(t) + \frac{1}{\omega} \sin \omega\tau \mathbf{C}(t) \mathbf{\Omega} + \frac{1}{\omega^2} (1 - \cos \omega\tau) \mathbf{C}(t) \mathbf{\Omega}^2 \quad (5.4)
\end{aligned}$$

where

$$0 \leq \tau \leq \Delta T$$

$$\mathbf{\Omega} = \begin{bmatrix} 0 & -\omega_z & \omega_y \\ \omega_z & 0 & -\omega_x \\ -\omega_y & \omega_x & 0 \end{bmatrix}$$

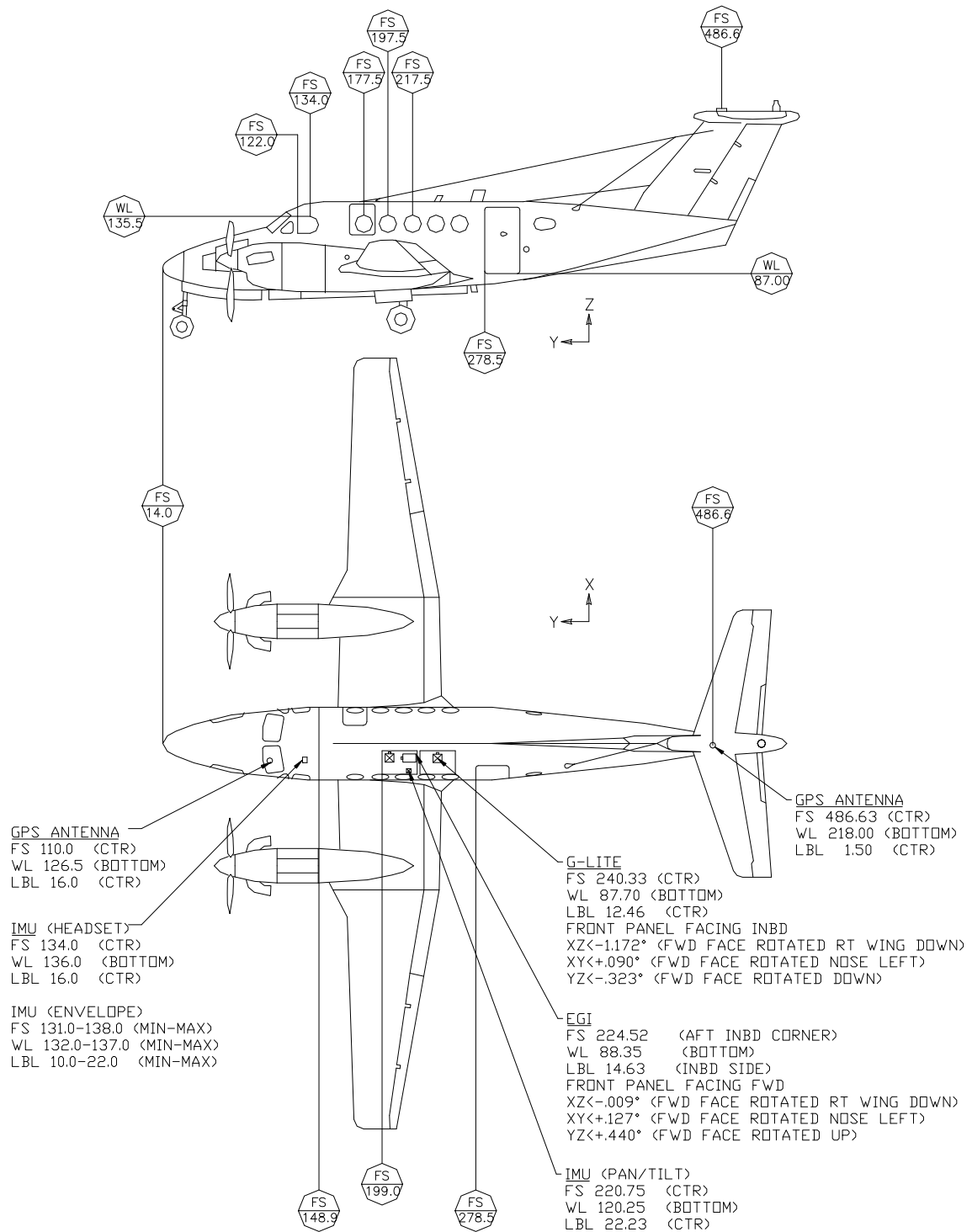
$$\mathbf{\Omega}^2 = \begin{bmatrix} -(\omega_y^2 + \omega_z^2) & \omega_x \omega_y & \omega_x \omega_z \\ \omega_x \omega_y & -(\omega_x^2 + \omega_z^2) & \omega_y \omega_z \\ \omega_x \omega_z & \omega_y \omega_z & -(\omega_x^2 + \omega_y^2) \end{bmatrix}$$

$$\omega^2 \equiv \omega_x^2 + \omega_y^2 + \omega_z^2$$

This DCM propagation may provide more accurate results than the first order propagation used in the current algorithm.

- **Develop better sensor errors models.** Currently, both accelerometer bias and gyro drift are modeled as a random walk. It might be beneficial to model other components of accelerometer error such as scale factor errors, cross-coupling errors, and vibro-pendulous error. For the gyros, investigate modelling g-dependent bias, anisoelastic bias, scale factor error, and cross-coupling errors. All of these error components are described in [31] and additional information can be found in [14].
- **Watch out for MT9 timer tick problems.** If using the Xsens MT9 IMU, occasionally data will be transmitted that passes the checksum but contains erroneous timer tick values. If the timer ticks are being used to time tag the IMU data, a test should be accomplished to check for erroneous timer ticks.
- **Accomplish further tuning of the Kalman filter.** Due to the time constraints already mentioned, extensive Kalman Filter tuning could not be accomplished. The current noise and initial covariance values are reasonable, but further refinement may provide improved performance.

Appendix A. C-12C Tail Number 73-1215 Equipment Coordinates



Bibliography

1. Austin, Kurt. "Air Force Tactics, Techniques, and Procedures, 3-3, Volume 20, Combat Aircraft Fundamentals, B-1." Air Warfare Center Weapons and Tactics Documentation Divison, May 2000.
2. Azuma, Ronald T. "A Survey of Augmented Reality." *Presence: Teleoperators and Virtual Enviroments*. 355–385. 1997.
3. Britting, Kenneth R. *Inertial Navigation Systems Analysis*. New York: Wiley-Interscience, 1971.
4. Brungart, Douglas. "Human Effectiveness Directorate Research and Development Area Plan." 3-D Audio Displays Technology, October 2002.
5. Chai, Lin, William A. Hoff, and Tyrone Vincent. "3-D Motion and Structure Estimation Using Inertial Sensors and Computer Vision for Augmented Reality." Submitted to *Presence: Teleoperators and Virtual Environments*.
6. Computer Sciences Corporation, Edwards, California. *Multi-Sensor Optimal Smoother Estimation Software Users Guide*, 2001.
7. Dell, William, "The Use of 3D Audio to Improve Auditory Cues in Aircraft." Department of Computing Science, University of Glasgow, 2000.
8. Draper, Charles S., Walter Wrigley, and John Hovorka. *Inertial Guidance*. Pergamon Press, 1960.
9. Ellum, Cameron and Nasser El-Sheimy. "Inexpensive Kinematic Attitude Determination from MEMS-Based Accelerometers and GPS-Derived Accelerations," *Journal of The Institute of Navigation*, 49(3):117–126 (Fall 2002).
10. Foxlin, Eric. "Inertial Head-Tracker Sensor Fusion by a Complementary Separate-Bias Kalman Filter." *Proc. of IEEE Virtual Reality Annual International Symposium*. 184–194. 1996.
11. GARMIN Corporation, Olathe, Kansas. *GPS 35 Technical Specifications*, 1998.
12. HEBSCO, Inc. *Technical Order 1C-12A-1*. Flight Manual, USAF Series Aircraft, C-12C, 1 November 2003.
13. Joffrion, Jacque M. *Inertial Head Tracking for 3D Audio (Project Sound Advice) Test Plan*. USAF TPS-TP-04A-04, USAF Test Pilot School, Edwards AFB, CA, October 2004.
14. Lawrence, Anthony. *Modern Inertial Technology - Navigation, Guidance, and Control*. Springer-Verlag, 1993.

15. Mathur, Navin and Frank van Grass. "Feasibility of Using a Low-Cost Inertial Measurement Unit with Centimeter-Level GPS." *International Association of Institutes of Navigation World Congress in Association with the U.S. Institute of Navigation Annual Meeting*. 712–720. June 2000.
16. Maybeck, Peter S. *Stochastic Models, Estimation, and Control, Volume 1*. New York: Academic Press Inc., 1979. Republished, Arlington, VA: Navtech, 1994.
17. Maybeck, Peter S. Class handout distributed in EENG 765, EENG765: Stochastic Estimation and Control I, Wright-Patterson AFB OH, 2003.
18. Miller, Mikel M. Class handout distributed in EENG 735, EENG735: Inertial Navigation System Analysis and Integration, Wright-Patterson AFB OH, July 2003.
19. Misra, Pratap and Per Enge. *Global Positioning System: Signals, Measurements, and Performance*. Lincoln MA: Ganga-Jamuna Press, 2001.
20. Neu, Jonathan M. *A Tightly-Coupled INS/GPS Integration Using a MEMS IMU*. MS Thesis, Air Force Institute of Technology, Wright-Patterson Air Force Base, Ohio, 2004.
21. Pachter, L.S. and M. Pachter, "Strapdown Inertial Navigation and Numerical Analysis," April 2003.
22. Pachter, Meir. Class handout distributed in EENG 534, EENG534: Fundamentals of Aerospace Instruments and Navigation Systems, Wright-Patterson AFB OH, 2003.
23. Pachter, Meir. Class handout distributed in EENG 635, EENG635: Inertial Navigation Systems, Wright-Patterson AFB OH, 2003.
24. Raquet, John F. Class handout distributed in EENG 533, EENG533: Navigation Using the Global Positioning System, Wright-Patterson AFB OH, April 2003.
25. Rogers, Robert M. *Applied Mathematics in Integrated Navigation Systems*. American Institute of Aeronautics and Astronautics, 2000.
26. Rolland, Jannick, Yohan Baillot, and Alexei A. Goon, "A Survey of Tracking Technology for Virtual Environments." University of Central Florida, Center for Research and Education in Optics and Lasers. no date.
27. Schwarz, K. P. and M. Wei. "Efficient Numerical Formulas for the Computation of Normal Gravity in a Cartesian Frame," *Manuscripta Geodaetica* (1990).
28. Seidman, David. *The Essential Wilderness Navigator*. Camden, Maine: Ragged Mountain Press, 1995.
29. Soloviev, Andrey and Frank van Grass. "Review of Potential Applications of Low-Cost GPS/INS for General Aviation." *Institute of Navigation NTM*. January 2003.

30. Taschner, Michael J. *Modification Manual: C-12C, Serial Number 73-1215*. Air Force Flight Test Center, Edwards AFB, 2002.
31. Titterton, D. H. and J. L. Weston. *Strapdown Inertial Navigation Technology*. London, UK: Peter Peregrinus, Ltd., 1997.
32. van Graas, Frank and James Farrell, "GPS/INS - A Very Different Way." 57th Annual Meeting and the 20th Biennial Guidance Test Symposium, Albuquerque, NM, June 2001.
33. Vincent, Roger M., David J. Hoey, Peter W. Matisoo, and Michael T. Panarisi. *A Limited Evaluation of Three-Dimensional Audio's Potential to Enhance Situation Awareness and Improve Survivability in a Tactical Fighter Aircraft (HAVE EAR)*. Technical Report AFFTC-TLR-96-38, Edwards AFB, California: Air Force Flight Test Center, Air Force Materiel Command, United States Air Force, January 1997.
34. Wei, M. and K. P. Schwarz. "A Strapdown Inertial Algorithm Using an Earth-Fixed Cartesian Frame," *Journal of the Institute of Navigation*, 37(2):153-167 (Summer 1990).
35. XSens Technologies, Enschede, The Netherlands. *MT-9B Data Sheet*, 2003.
36. Yang, Yunchun and Jay Farrell. "Two-Antenna GPS and Low Cost INS Tight Integration for Attitude Determination." *Institute of Navigation GPS*. September 2001.

Vita

Captain Jacque M. Joffrion grew up in Clovis, New Mexico and graduated from Clovis High School in 1992. He entered the United States Air Force Academy after high school and graduated with a Bachelor of Science Degree in Electrical Engineering in 1996. Captain Joffrion attended USAF pilot training at Laughlin Air Force Base from October 1996 until October 1997. After pilot training, he was trained to fly the B-1B at Dyess Air Force Base where he served operationally for three years. His next assignment was to Ellsworth Air Force Base where he served as a B-1B instructor pilot for one year before being accepted into the joint AFIT/Test Pilot School Program. He began the program in August of 2002 and completed the required AFIT coursework in November 2003. He was then re-assigned to the USAF Test Pilot School in January 2004. After graduating from Test Pilot School, Captain Joffrion completed his research and defended his thesis at AFIT in March of 2005.

Permanent address: ON FILE

REPORT DOCUMENTATION PAGE				Form Approved OMB No. 0704-0188	
Public reporting burden for this collection of information is estimated to average 1 hour per response, including the time for reviewing instructions, searching existing data sources, gathering and maintaining the data needed, and completing and reviewing this collection of information. Send comments regarding this burden estimate or any other aspect of this collection of information, including suggestions for reducing this burden to Department of Defense, Washington Headquarters Services, Directorate for Information Operations and Reports (0704-0188), 1215 Jefferson Davis Highway, Suite 1204, Arlington, VA 22202-4302. Respondents should be aware that notwithstanding any other provision of law, no person shall be subject to any penalty for failing to comply with a collection of information if it does not display a currently valid OMB control number. PLEASE DO NOT RETURN YOUR FORM TO THE ABOVE ADDRESS.					
1. REPORT DATE (DD-MM-YYYY) 21-03-2005		2. REPORT TYPE Master's Thesis		3. DATES COVERED (From - To) Aug 2002 - Mar 2005	
4. TITLE AND SUBTITLE Head Tracking for 3D Audio Using a GPS-Aided MEMS IMU					
				5b. GRANT NUMBER	
				5c. PROGRAM ELEMENT NUMBER	
6. AUTHOR(S) Joffrion, Jacque M., Captain, USAF				5d. PROJECT NUMBER	
				5e. TASK NUMBER	
				5f. WORK UNIT NUMBER	
7. PERFORMING ORGANIZATION NAME(S) AND ADDRESS(ES) Air Force Institute of Technology Graduate School of Engineering and Management (AFIT/EN) 2950 Hobson Way, Building 640 WPAFB OH 45433-7765				8. PERFORMING ORGANIZATION REPORT NUMBER AFIT/GE/ENG/05-09	
9. SPONSORING / MONITORING AGENCY NAME(S) AND ADDRESS(ES) Dr. Douglas S. Brungart AFRL/HECB 2610 Seventh Street WPAFB OH 45433-7901 785-6127 x4274				10. SPONSOR/MONITOR'S ACRONYM(S) AFRL/HECB	
				11. SPONSOR/MONITOR'S REPORT NUMBER(S)	
12. DISTRIBUTION / AVAILABILITY STATEMENT APPROVED FOR PUBLIC RELEASE, DISTRIBUTION UNLIMITED					
13. SUPPLEMENTARY NOTES					
14. ABSTRACT Audio systems have been developed which use stereo headphones to project sound in three dimensions. When using these 3D audio systems, audio cues sound like they are originating from a particular direction. There is a desire to apply 3D audio to general aviation applications, such as projecting control tower transmissions in the direction of the tower or providing an audio orientation cue for VFR pilots who find themselves in emergency zero-visibility conditions. 3D audio systems, however, require real-time knowledge of the pilot's head orientation in order to be effective. This research describes the development and testing of a low-cost head tracking system for 3D audio rendering applied in general aviation. The system uses a low-cost MEMS IMU combined with a low-cost, single frequency GPS receiver. Real-time data from both of these systems was sent to a laptop computer where a real-time Kalman filter was implemented in MATLAB to solve for position velocity, and attitude. The attitude information was then sent to a 3D audio system for sound direction rendering. The system was flight tested on board a Raytheon C-12C aircraft. The accuracy of the system was measured by comparing its output to truth data from a high-accuracy post-processed navigation-grade INS/DGPS solution. Results showed that roll and pitch error were accurate to within 1-2 degrees, but that heading error was dependent upon the flight trajectory. During straight-and-level flight, the heading error would drift up to 10-15 degrees because of heading unobservability. However, even with heading error, the ability of a pilot to determine the correct direction of a 3D audio cue was significantly improved when using the developed head tracking system over using the navigation-grade INS/GPS system fixed to the aircraft.					
15. SUBJECT TERMS Cueing, Cues (Stimuli), Directional, Flight Testing, Inertial Guidance, Inertial Navigation, Kalman Filtering, Navigation Reference, 3-D Audio, 3-D Auditory Displays, C-12 Aircraft, Directional Signals, GPS/INS Fusion, GPS/INS Integration, Head Tracking Systems, IMU (Inertial Measurement Unit), Inertial Sensors, MEMS (Microelectromechanical Systems), Navigation Reference Systems, Pilot Cueing					
16. SECURITY CLASSIFICATION OF:			17. LIMITATION OF ABSTRACT	18. NUMBER OF PAGES	19a. NAME OF RESPONSIBLE PERSON
a. REPORT	b. ABSTRACT	c. THIS PAGE			Dr. John Raquet , AFIT/ENG
U	U	U	UU	129	19b. TELEPHONE NUMBER (include area code) (937) 785-6565 x4580